Direct numerical simulation of wall turbulence subjected to an adverse pressure gradient

Hussein Rkein

Laboratoire de Mécanique des Fluides de Lille
Kampé de Fériet

Université de Lille

University of Lille
Doctoral School ENGSYS-632

Ph.D. Thesis
to obtain the doctorate

Specialty: Fluid Mechanics

Direct Numerical Simulation of Wall Turbulence subjected to an Adverse Pressure Gradient

---

Publicly presented and defended by

Hussein RKEIN

on December,15th 2021

Composition of the jury:

Reviewer	**Sylvain LAIZET**	Reader, Imperial College, London
Reviewer	**Bérengère PODVIN**	Research Director, CNRS, EM2C, Gif/Yvette
President	**Jean-Marc FOUCAUT**	Professor, LMFL, École Centrale de Lille
Examiner	**Nicolas RENARD**	Research Engineer, ONERA, Meudon
Supervisor	**Jean-Philippe LAVAL**	Research Director, CNRS, LMFL, Lille

Ph.D. thesis prepared at Lille Laboratory of Fluid Mechanics - Kampé de Fériet

Laboratoire de Mécanique des Fluides de Lille
Kampé de Fériet

Université de Lille

Université de Lille
Ecole Doctorale ENGSYS-632

Thèse de Doctorat
en vue de l'obtention du grade de
Docteur

Spécialité : Mécanique des milieux fluides

Simulation numérique directe de la turbulence de paroi soumise à un gradient de pression défavorable

---

Présentée et soutenue publiquement par

Hussein RKEIN

le 15 décembre 2021

Composition de jury:

Rapporteur	**Sylvain LAIZET**	Reader, Imperial College London
Rapporteur	**Bérengère PODVIN**	Directrice de Recherche, CNRS, EM2C, Gif/Yvette
Président	**Jean-Marc FOUCAUT**	Professeur, LMFL, École Centrale de Lille
Examinateur	**Nicolas RENARD**	Ingénieur de Recherche, ONERA, Meudon
Directeur de thèse	**Jean-Philippe LAVAL**	Directeur de Recherche, CNRS, LMFL, Lille

Thèse de doctorat préparée à Laboratoire de Mécanique des Fluides de Lille - Kampé de Fériet

Abstract

The main objective of this work is to analyze the effects of a moderate adverse pressure gradient on the dynamics of turbulent boundary layer flows. For that purpose, a direct numerical simulation (DNS) of the turbulent boundary layer (TBL) subjected to a moderate adverse pressure gradient (APG) out of equilibrium has been performed using the open-source code Incompact3d up to a Reynolds number of 8000 based on momentum thickness. A large database resolved in time and space was collected and used to analyze the turbulence statistics. Special attention has been paid to the existence and evolution of the outer peak of Reynolds stresses observed in APG wall-bounded flows. Different velocity scalings have been investigated and tested against the numerical results. The velocity scale based on the shear stress is shown to scale all the Reynolds stresses profiles for different Reynolds numbers, indicating that all Reynolds stresses are associated with a single dynamics of turbulent structures.

The large-scale coherent structures of the streamwise velocity fluctuations have been investigated using two-point spatial correlation. A comparison with a zero pressure gradient case at an equivalent Reynolds number allows us to further investigate the effect of the pressure gradient on the size and inclination of attached coherent structures. A deeper investigation of the coherent structures was also performed, where each structure was detected separately based on a thresholding method to distinguish between the effects of large and small scales and to better understand the mechanisms controlling the dynamics of these structures. The contribution of large-scale motions (LSM) on the Reynolds stresses comparing with ZPG case was also analyzed.

Keywords: turbulence, direct numerical simulation, turbulent boundary layers

Résumé

L'objectif principal de ce travail est d'analyser les effets d'un gradient de pression défavorable modéré sur la dynamique d'écoulement d'une couche limite turbulente. Dans ce contexte, une simulation numérique directe (DNS) de la couche limite turbulente (TBL) soumise à un gradient de pression défavorable modéré (APG) hors équilibre a été réalisée jusqu'à un Reynolds de 8000 en utilisant le code open-source Incompact3d. Une large base de données résolues en temps et en espace a été collectée et utilisée pour analyser les statistiques de la turbulence. Une attention particulière a été consacrée à l'existence et à l'évolution du pic de contraintes de Reynolds observé dans la zone externe de la couche limite. Différentes échelles de vitesse ont été étudiées, testées et confrontées aux résultats numériques. L'échelle de vitesse basée sur la contrainte de cisaillement permet de mettre à l'échelle tous les profils de contraintes de Reynolds pour plusieurs nombres de Reynolds, ce qui indique que toutes les contraintes de Reynolds sont associées à une dynamique unique des structures turbulentes.

Les structures cohérentes à grande échelle des fluctuations de vitesse longitudinales ont été étudiées en utilisant la corrélation spatiale en deux points. Une comparaison avec un cas sans gradient de pression à un nombre de Reynolds équivalent nous permet d'étudier l'effet du gradient de pression sur la taille et l'inclinaison des structures cohérentes attachées. Une étude approfondie sur les structures cohérentes a également été réalisée, où chaque structure a été détectée séparément en utilisant une méthode de seuillage afin de distinguer les effets des grandes et petites échelles et de mieux comprendre les mécanismes qui contrôlent la dynamique de ces structures. La contribution des mouvements de grande échelle (LSM) sur les contraintes de Reynolds en comparaison avec le cas ZPG a également été analysée.

Mots clés : turbulence, simulation numérique directe, couches limites turbulentes

Acknowledgments

This achievement could not have been possible without the valuable help and support of many people. I would like to offer my genuine gratitude to all of those who had faith and trust that this work will be achieved successfully when it had seemed impossible.

At the beginning, I express my deepest sense of gratitude to Dr. Jean-Philippe Laval, my esteemed supervisor, who inspired me and offered me a support while conducting this PhD. I would like to thank him for his vivid insight, constant support, thoughtful guidance, and authentic feedback. Saying "thank you" may seem simple; my unfeigned thanks go to him when acknowledging his encouragement, patience, suggestions and corrections. I will always be indebted to him for sharing me his knowledge of fluid mechanics, turbulence and numerical simulation as well as his mentorship about life.

In addition, I would like to express my sincere thanks to Dr. Sylvain Laizet and Dr. Bérengère Podvin for their effort and time exerted in reading and reviewing this thesis. I also thank Dr. Nicolas Renard and Dr. Jean-Marc Foucaut for accepting to be part of the jury.

Thanks to all my colleagues at building M6 during these four years for providing amazing activities inside and outside the Lab. I am also grateful to the secretariat team for their unfailing support and assistance.

This study could not have been possible without financial support and computational resources. In this context, I would like to thank the Islamic Center association for Guidance and Higher Education in Lebanon for the financial support. Special thanks to GENCI for the computational resources on the Occigen and Jean-Zay supercomputers. I would also like to express my gratitude to Dr. Sylvain Laizet for providing the open-source code Incompact3d.

In addition, words fail to express my deepest appreciation to all my friends, your company has really made my time enjoyable and memorable.

Finally, I must express my gratitude to my family for providing me unfailing

support, and continuous encouragement throughout my years of study, and through the process of researching and writing this thesis.

Nomenclature

Abbreviations

2D	Two-dimensional
3D	Three-dimensional
APG	Adverse pressure gradient
CFL	Courant-Fiedrichs-Lewy number
DNS	Direct numerical simulation
FFT	Fast Fourier Transform
FPG	Favorable pressure gradient
HW	Hot-wire
LES	Large-Eddy Simulation
LSM	Large-scale motions
PIV	Particle image velocimetry
PTV	Particle tracking velocimetry
TBL	Turbulent boundary layer
TKE	Turbulent kinetic energy
VLSM	Very large-scale motions
ZPG	Zero pressure gradient

Greek Symbols

β	Clauser's non-dimensional pressure gradient parameter
δ	Boundary layer thickness, δ_{99}
δ_1	Displacement thickness

δ_ν	Viscous length scale, ν/u_τ
ϵ	Dissipation rate of turbulent kinetic energy
η	Kolmogorov length scale
κ	Von Kármán constant
μ	Dynamic viscosity of the fluid
ν	Kinematic viscosity of the fluid, μ/ρ
ρ	Density of the fluid
τ_w	Wall shear stress
θ	Momentum thickness

Roman Symbols

C_f	Skin friction coefficient
H	Shape factor
h	Channel half-width
k_x, k_z	Streamwise and spanwise wavenumber
L_x, L_y, L_z	Computational domain size in the spatial directions
N_x, N_y, N_z	Number of computational mesh nodes in the spatial directions
P	Pressure
Re_τ	Reynolds number based δ and u_τ
Re_θ	Reynolds number based θ and U_e
t	Time
U	Instantaneous streamwise velocity
u	Streamwise fluctuating velocity
U_e	Free stream velocity
U_{ZS}	Zagarola-Smits outer velocity scale
u_τ	Friction velocity
V	Instantaneous wall-normal velocity
v	wall-normal fluctuating velocity
W	Instantaneous spanwise velocity
w	Spanwise fluctuating velocity
x	Streamwise coordinate

y	Wall-normal coordinate
z	Spanwise coordinate

Special symbols

$(.)^+$	Variable in wall-units, normalized using u_τ and ν
$(.)_{ref}$	Reference position such that $Re_\theta = 7240$
$\langle . \rangle$	Average in the homogeneous directions

Contents

List of Tables

List of Figures

Chapter 1

Introduction

1.1 Background

Turbulence is among the most difficult problems of physics. Turbulent flows are highly disordered as such they are unpredictable. Most flows in nature are turbulent, starting from smoke of a cigarette, breaking of ocean wave as well as atmospheric flows. High energy consumption of vehicles (e.g. airplanes, cars, ships and submarines) results from the turbulent state. The theory of turbulence phenomenon is yet incomplete. As Navier-Stokes equations (equations describing fluid motion) are non-linear, non-stationary and non-local, analytical solutions corresponding to a turbulent state are still unknown and will probably remain for most of the turbulent flows. As the hope to find analytical solutions of the governing equations is very low, the main challenge is to understand the mechanism of turbulence in order to derive efficient models which could be used to reduce the very large degree of freedom associated with turbulent flows. One can distinguish between free turbulence and wall turbulence, the latter being generated and affected by the presence of one or more solid surfaces (wings of an airplane, turbine blade, ...). Therefore, wall turbulence is present in most if not all industrial flows.

Boundary Layer is the thin layer that appears near the wall due to skin friction. Improvement of the safety and performance of vehicles depends on detailed knowledge of the turbulence within the boundary layer. The book of Schlichting and Gestern [127] presents a complete review about wall-bounded flow theory.

A big challenge in investigating turbulence is to transfer complex turbulent motions into simpler motions called coherent structures. Over the past decades, a large effort has been devoted to study the coherent structures in turbulent flows. Efforts were exerted on the understanding of the nature and origin of the coherent structures, as well as the lifespan and the way of their development besides other statistics. Most of the studies focus on the case of boundary layer on a flat

plate without pressure gradient as it is the simplest academic case of wall-bounded flows. However, in industrial applications, the flows are usually bounded by curved geometries and therefore exposed to an adverse pressure gradient leading to flow deceleration and change in behavior compared to the zero pressure gradient boundary layer.

The constant increase of computing resources enables numerical simulations with more and more degrees of freedom. In parallel the progress in experimental techniques allows us to investigate a wide range of length and time scales of turbulent flows. These new capabilities associated with advanced post-processing of the large databases facilitate a detailed description of turbulent flows which is the first and necessary step to build efficient models. Academic ideal turbulent flows such as turbulence in a periodic box were the first to be simulated. However, high fidelity numerical simulations of wall-bounded turbulent flows are now commonly performed but for a restricted number of academic cases.

This study is dedicated to fill a gap in the numerical studies of turbulent boundary layers subjected to moderate adverse pressure gradient for a case of Reynolds number higher than that taken in previous studies.

1.2 Objectives

The overarching objective of the present work is to further understand the effect of adverse pressure gradient on the turbulent boundary layer. For that purpose, a large database well-resolved in time and space was performed. The database will allow several future studies in our research team. This database can be compared with available numerical and experimental databases (with or without pressure gradient) in order to check the validity and the universality of turbulence theories and scalings. Furthermore, the current non-equilibrium boundary layer contributes to testing models proposed for equilibrium wall-bounded flows.

The first part of the work focuses on the outer region of the turbulent boundary layer since it is strongly affected by the presence of an adverse pressure gradient. The goal is to find the link between the Reynolds stresses and the turbulent production rate. To do so, it is essential to clarify the causes of the strong turbulent activity in the outer region, whether it is the Reynolds number, adverse pressure gradient or both of them.

The second part of the work is dedicated to understand the large-scale motions of the streamwise velocity fluctuations and their sensitivity to a moderate adverse pressure gradient. The objective is to examine the geometric characteristics of the structures in terms of shape, dimension and arrangement. Besides, efforts were made

to investigate the dominance between low- and high-momentum structures along the boundary layer.

1.3 Organization of the thesis

This thesis is composed of six chapters organized as follows:

The background of the current work and objective of the study are introduced in Chapter 1. In Chapter 2, a review of the literature focused on the turbulent boundary layer flows and the organization of coherent structures populating these flows, is presented. Investigations of the effect of an adverse pressure gradient on TBL and coherent structures are also reviewed.

Chapter 3 reveals some specifications of the numerical solver and the parameters used for the simulation. Some statistics that represent the characteristics of the current DNS are also outlined. The statistical results of the TBL are presented in Chapter 4. Statistics of Reynolds stresses are presented with a special emphasis on the peak appearing in the outer region. Different types of velocity scaling are discussed and tested using the current database.

Chapter 5 is devoted to the analysis of coherent structures. The average statistics and the detection technique of the three-dimensional structure based on the strong negative and positive streamwise velocity fluctuations are shown.

Finally, the main conclusions and future work of this investigation are summarized in Chapter 6.

Chapter 2

Turbulent Boundary Layers

This chapter provides an overview of the theories of wall-bounded flows and focuses on the zero pressure gradient turbulent boundary layer and how it is organized. Various types of coherent structures along the boundary layer are reported. The effect of the pressure gradient on the boundary layer is then discussed.

2.1 Governing equations

The equations governing a fluid flow are functions of the properties of the flow. A significant change of pressure and temperature may change the density ρ and the flow becomes compressible. In this case, the variation of density in time or space can not be neglected. When the Mach number (dimensionless number that expresses the ratio between the characteristic velocity of the fluid and the local speed of sound) is less than 0.3, the flow is usually considered to be incompressible. In this case, the density is considered to be constant as the pressure and the temperature doesn't have important variation.

The viscosity of fluid noted μ characterizes the resistance against any force that tends to move the fluid layers over each other. The ideal fluids are considered as non-viscous fluids. When the fluid density ρ and the dynamic viscosity μ are supposed to be constant and not affected by the temperature, the flow will be considered as isothermal. In most applications including aeronautics applications, the fluids are considered as Newtonian fluid which means that at every point the viscous stresses arising from the flow are linearly related to the local strain rate.

The fundamental conservation laws of the fluid flow are expressed by partial differential equations based on the continuum hypothesis. The conservation laws are expressed for a closed control volume V of the fluid domain. The boundary of V is considered as a closed control surface S with a normal unit vector $\mathbf{n}$ directed towards the outside of V.

2.1.1 Conservation laws

The conservation of mass law includes the rate of accumulation of mass in a volume V that ensures the balance between mass entering and leaving V across its boundary S; it is expressed in the following equation:

$$\frac{\partial}{\partial t}\int_V \rho dV + \int_S \rho \mathbf{n}.\mathbf{U} dS = 0, \tag{2.1}$$

where t is the time and $\mathbf{U}$ is the instantaneous fluid velocity vector. By applying the Gauss' divergence theorem[1]. Then, by integrating over an arbitrary volume, we obtain the continuity equation:

$$\frac{\partial \rho}{\partial t} + \nabla.(\rho \mathbf{U}) = 0 \tag{2.2}$$

In an incompressible fluid, the density ρ is considered as constant in both space and time. After neglecting all density-dependent terms, the conservation of mass equation gives us the flow incompressibility condition which is noted as the following:

$$\nabla.\mathbf{U} = 0 \tag{2.3}$$

The conservation of momentum involves the rate of accumulation of momentum in V, and the momentum flux passing through S must be equivalent to the momentum gain due to body forces and surface stresses. It is represented mathematically as

$$\frac{\partial}{\partial t}\int_V \rho \mathbf{U} dV + \int_S \rho (\mathbf{n}.\mathbf{U})\mathbf{U} dS = \int_V \rho \mathbf{f} dV + \int_S \mathbf{n}.\sigma dS \tag{2.4}$$

where $\mathbf{f}$ is the body forces and σ is the stress tensor. By applying the same procedures of (2.2) and using the continuity equation, the previous equation leads to

$$\rho\left(\frac{\partial \mathbf{U}}{\partial t} + \mathbf{U}.\nabla\mathbf{U}\right) = \rho\mathbf{f} + \nabla.\sigma \tag{2.5}$$

For an incompressible fluid with constant viscosity, the stress term has been reduced and replaced in the conservation of momentum equation. We finally obtain the most frequently used governing equation in fluid dynamics which is known as the incompressible Navier-Stokes equation

$$\frac{\partial \mathbf{U}}{\partial t} + \mathbf{U}.\nabla\mathbf{U} = -\frac{1}{\rho}\nabla P + \nu\Delta\mathbf{U} + \mathbf{f} \tag{2.6}$$

[1]Let $\mathbf{F}$ be a continuously differentiable vector field defined in the volume V and S is a closed boundary of V, we have $\int_S \mathbf{F}.\mathbf{n}dS = \int_V \nabla.\mathbf{F}dV$

where P represents the static pressure and $\nu = \mu/\rho$ is the kinematic viscosity.

2.1.2 Boundary layer assumptions

In the current work, isothermal flows of a Newtonian fluid are investigated. Like many other sufficiently low-speed flows, the flow can be described by the incompressible Navier-Stokes equations. They are represented by the aforementioned continuity (2.3) and conservation of momentum (2.6) equations.

By considering density, viscosity and temperature as constants, the physical properties that are computed are pressure and the three components of velocity. We denoted hereafter x, y, and z as the positions in the streamwise, wall-normal, and spanwise directions respectively. U, V and W are considered as the relevant instantaneous velocity components.

The three-dimensional continuity equation (2.7) is presented with the momentum equation of the three components of velocity (2.8) where i and $j = 1, 2, 3$.

$$\frac{\partial U_i}{\partial x_i} = 0 \tag{2.7}$$

$$\frac{\partial U_i}{\partial t} + U_j \frac{\partial U_i}{\partial x_j} = -\frac{1}{\rho}\frac{\partial P}{\partial x_i} + \nu \frac{\partial^2 U_i}{\partial x_j^2} \tag{2.8}$$

In order to simplify and understand the complex motion of the fluid flow, each component of the instantaneous velocity is decomposed into its mean and its fluctuating parts $U_i = \langle U_i \rangle + u_i$ [117], where $\langle . \rangle$ is the average of the relevant quantity in the homogeneous directions.

Taking the average of the NS equations (2.7) and (2.8) and considering that the spanwise direction is a homogeneous direction, one can simplify the equation for the mean velocity as the spanwise velocity and all derivatives with respect to the spanwise direction are suppressed. Furthermore, as the fluid properties are considered as constant over time and the boundary conditions are fixed, the flow over the boundary layer will be considered as steady and the time-dependent terms must be neglected. Moreover, it is known that in the boundary layer the flow grows slowly in the streamwise direction, but is subjected to strong velocity gradients in the wall-normal direction in order to reach the free-stream velocity outside the turbulent region. For that purpose, the x-derivatives are neglected in comparison to those in the y-direction in the momentum equations.

Based on the previous assumptions, equations (2.7) and (2.8) are reduced to the

boundary layer equations for the mean flow:

$$\frac{\partial \langle U \rangle}{\partial x} + \frac{\partial \langle V \rangle}{\partial y} = 0 \tag{2.9}$$

$$\langle U \rangle \frac{\partial \langle U \rangle}{\partial x} + \langle V \rangle \frac{\partial \langle U \rangle}{\partial y} = -\frac{1}{\rho}\frac{\partial P}{\partial x} + \nu \frac{\partial^2 \langle U \rangle}{\partial y^2} - \frac{\partial \langle uv \rangle}{\partial y} \tag{2.10}$$

$$0 = \frac{1}{\rho}\frac{\partial P}{\partial y} + \frac{\partial \langle vv \rangle}{\partial y} \tag{2.11}$$

Further details on the boundary layer assumptions are summarized in the books of Schlichting and Gestern [127] and Pope [113].

2.1.3 Turbulent flows parameters

Due to the no-slip condition, the 3 velocity components at the wall are zero. The mean streamwise velocity increases far from the wall to reach asymptotically a constant free-stream velocity (U_e) at the outer edge of the boundary layer.

The boundary layer thickness (δ) is generally defined as the wall-normal position at which the mean streamwise velocity is equal to 99% of the free-stream velocity. Other definitions have been proposed in the literature to estimate δ [159].

Another measure for the boundary layer thickness is the displacement thickness δ_1 (also denoted δ^*). It tells us how much the streamlines of the outer flow are displaced by the effect of the boundary layer [127]. For example, the mass flow is lost due to wall friction, and its deficit is equivalent to the mass flow rate for an inviscid boundary layer at the same free-stream velocity up to δ_1.

The integral form of the displacement thickness is given by

$$\delta_1 = \int_0^\delta \left(1 - \frac{\langle U \rangle}{U_e}\right) dy \tag{2.12}$$

The momentum thickness θ (also denoted δ_2) is another integral parameter that corresponds to the required thickness of an inviscid boundary layer to retain the same momentum. It is defined by:

$$\theta = \int_0^\delta \frac{\langle U \rangle}{U_e}\left(1 - \frac{\langle U \rangle}{U_e}\right) dy \tag{2.13}$$

The ratio between the last two thicknesses is called the shape factor

$$H = \frac{\delta_1}{\theta} \tag{2.14}$$

In a laminar boundary layer flow (Blasius boundary layer) $H \simeq 2.6$, whereas,

$H = 1.3 - 1.4$ in the ZPG turbulent boundary layer and it increases with the effects of the adverse pressure gradient. In the strong APG boundary layer of Gungor et al. [47], $H = 3.43$ was found at the edge of separation.

The skin-friction coefficient C_f defined as

$$C_f = \frac{\tau_w}{\frac{1}{2}\rho U_e^2} \tag{2.15}$$

is the non-dimensional measurement of the friction at the wall. It tends to zero when the flow is separated from the wall. Where τ_w is the wall shear stress which is defined as

$$\tau_w = \mu \frac{\partial \langle U \rangle}{\partial y}|_{y=0} \tag{2.16}$$

The friction velocity u_τ is the characteristic velocity scale near the wall, and it is related to τ_w by

$$u_\tau = \sqrt{\tau_w / \rho} \tag{2.17}$$

The non-dimensional Reynolds number [117] represents the relative importance of inertial forces in comparison to viscous ones. It is commonly used as a good indicator of fluid turbulence, where the increase in Reynolds number represents a transition from laminar to turbulent flows. Reynolds number can be defined based on different length scales (e.g. δ, δ_1 and θ) and various velocity scales such as, U_e and u_τ.

In turbulent boundary layers, several Reynolds numbers can be defined. The most commonly used are the Reynolds number based on the momentum thickness

$$Re_\theta = \frac{U_e \theta}{\nu} \tag{2.18}$$

and the Reynolds number based on the friction velocity

$$Re_\tau = \frac{u_\tau \delta}{\nu} \tag{2.19}$$

2.2 Zero pressure gradient wall-bounded flows

There are very old studies that were conducted to study the internal flows; for example, the channel and pipe flows. Common features were observed between internal flows and flows over a flat plate. The existence of a free-stream region far from the wall makes the study of boundary layers more complicated than that of internal flows. This is due to the growth of the boundary layer thickness in the streamwise direction.

Turbulent Boundary Layer is the simplest case of flows over a flat plate for which

zero pressure gradient cases implies that the pressure is constant in the streamwise direction and the term $\partial P/\partial x$ is neglected in (2.10).

The main characteristics of the ZPG turbulent boundary layer are summarized below.

2.2.1 TBL organization

In canonical wall-bounded flows, we can generally distinguish two regions, where different physical processes dominate, namely the inner and outer regions.

The inner region is a layer close to the wall (up to $y \simeq 0.1\delta$), and it is the region in which viscous forces are effective.

In the very near-wall region, the convective terms of the momentum equation can be neglected with respect to the diffusive terms and the equation (2.10) reduce to

$$\nu \frac{\partial^2 \langle U \rangle}{\partial y^2} - \frac{\partial \langle uv \rangle}{\partial y} = 0 \tag{2.20}$$

Integration of (2.20) in wall-normal direction leads to the total mean shear stress that is constant and must be equal to the wall shear stress. It is defined with its viscous and shear terms as follows:

$$\tau = \mu \frac{\partial \langle U \rangle}{\partial y} - \rho \langle uv \rangle = \tau_w = \rho u_\tau^2 \tag{2.21}$$

This region is classified into three layers based on the dominance between both terms of (2.21):

(i) **Viscous sublayer** is located in the very near-wall zone $y^+ < 5$, where viscosity is dominant due to the wall proximity, and the viscous term becomes dominant on the Reynolds stress one in (2.21) ($\mu \frac{\partial \langle U \rangle}{\partial y} \gg \rho \langle uv \rangle$). Here, the mean velocity profile is characterized by the linear law

$$U^+ = y^+ \tag{2.22}$$

where the superscript $(+)$ represents the scaling by unit-walls, i.e., u_τ as velocity-scale and $\delta_\nu = \frac{\nu}{u_\tau}$ as a length-scale. The wall-law is considered as being independent from Reynolds number.

(ii) **Buffer layer** ($5 < y^+ < 30$), in which both terms of τ become equivalents and the energy production has its maximum value and represented by a peak in the production rate profile at $y^+ \simeq 15$. Also, a peak in the streamwise velocity fluctuation profile at the same wall-normal position appeared.

(iii) **Overlap (logarithmic) region**, which is generally located at $\delta_\nu \ll y \ll \delta$. This extent shows that both wall-units and outer scaling (by U_e and δ) are valid in this region. Matching of both scalings leads to the famous Von Karman's logarithmic law of the mean velocity profile

$$U^+ = \frac{1}{\kappa_0} \log y^+ + C \tag{2.23}$$

with κ_0 and C are empirical constants. κ_0 is of the order of 0.41 but has been observed to vary slightly around this value for different flow types. The lowest value of κ_0 was found to be 0.38 using experimental ZPG boundary layers up to $Re_\theta = 70000$ [102, 101] and the highest was obtained in pipe flow experiment of Zagarola and Smits [171] as 0.45 for Reynolds numbers from 31×10^3 to 35×10^6.

The log layer is present only at sufficiently high Reynolds number and extends up to $0.1 - 0.2\delta$. There is no agreement on the lower bound of the log region as a meso-layer can be defined between the buffer and the log region ($30 \lesssim y^+ \lesssim 170$) [42].

The outer layer is composed of the upper part of the overlap layer and the wake region up to the edge of the boundary layer. In this region, the viscous forces are negligible as compared with the Reynolds stress terms that reach their maximum in this region. The large-scale structures, containing the highest level of energy, are also located in the outer layer. Maciel et al. [89] mentioned that the lower limit of the outer region is considered approximately $y = 0.15\delta$. The wake law that is proposed by Coles [24] is appropriate to give a description of this region.

As the viscous effect is almost negligible in this region, it is inappropriate to represent the mean velocity using the wall-unit which is based on viscous quantities. Outer characteristic length and velocity scales (U_e and δ) were used to define the velocity defect law (2.24), which is generally used to describe the streamwise velocity profile in the outer part up to the edge of the boundary layer.

$$\frac{U_e - U}{u_\tau} = f\left(\frac{y}{\delta}\right) \tag{2.24}$$

The different layers of the TBL are illustrated in Fig. 2.1 on a mean streamwise velocity profile obtained from the DNS of Sillero et al. [131] over a flat plate TBL corresponding to $Re_\tau = 1990$.

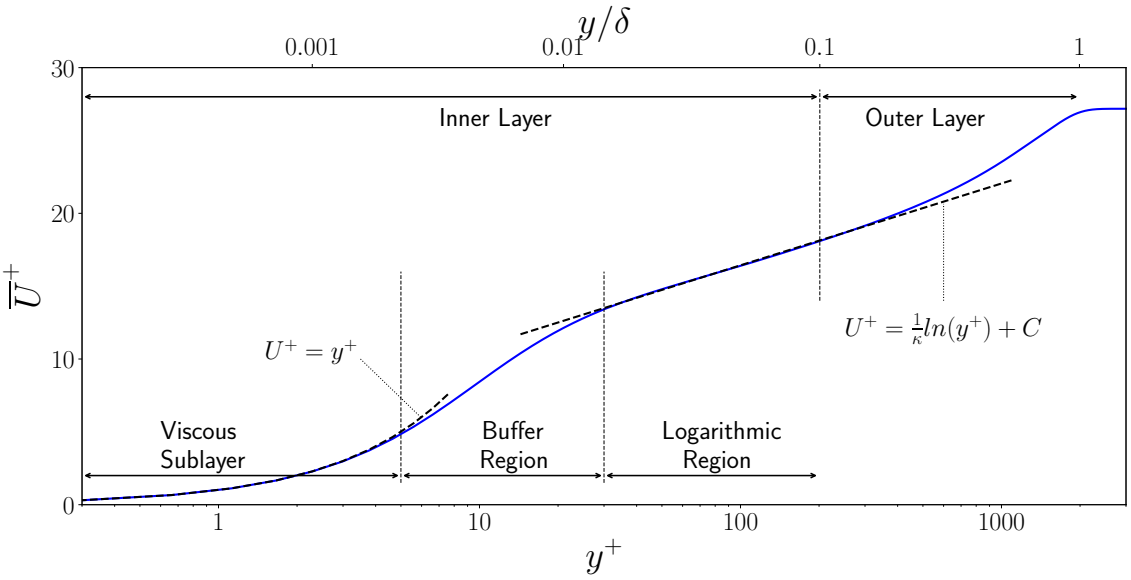

Fig. 2.1. The various regions of boundary layer are presented on a mean velocity profile of a flat plate TBL of Sillero et al. [131] at $Re_\theta = 6500$ ($Re_\tau = 1990$).

2.2.2 Experimental and numerical studies of canonical flows

Numerous numerical and experimental techniques are used to visualize and study the flow motion in a TBL. Traditional measurement techniques (dye, smoke) [116] were previously used to visualize the coherent structures in turbulent flows. But these techniques provide mainly qualitative observations.

In the past century, the hot-wire anemometer was invented as a new single-point technique to measure the flow velocity [25]. A lot of studies were conducted using the hot-wire method for various wall-bounded flows. In the late 20th century, the innovation of experimental techniques provided a multi-dimensional measurement method such as, particle image velocimetry (PIV) and Tomo-PIV which allows us to obtain multi-dimensional velocity fields in a 2D or 3D domain with a good spatial resolution.

Recently, Lagrangian particle tracking methods were developed, and it is known as Particle Tracking Velocimetry (PTV) that gives 3D trajectories up to several hundred of thousands of particles either in a small volume in order to access a very high spatial resolution down to the dissipative scales [30] or a large field of view using bigger Lagrangian tracers [36].

Through experiments, it is usually possible to obtain a realistic Reynolds number and flows around a complex shape similar to aeronautical applications. In spite of the great technical innovation, experiments are not able to reach sufficient spatial and time resolutions combines with a large field of view - particularly in the near-wall region - suitable for the identification of complex small-scale and large-scale

interactions.

Parallel to the experimental techniques and due to the technological innovation in computers, simulation of turbulent flows became possible in the last decades. Based on the accuracy and cost of simulation, three main approaches can be distinguished.

The first one is known as direct numerical simulation (DNS) where the turbulence is entirely resolved for all scales. The Navier-Stokes equations are accurately solved and high resolutions are used in all spatial directions. In addition, a small time step allows us to identify the 3D complex and/or small-scale motions and follow them along the flow through time. The fine spatial and temporal resolutions with the high order numerical schemes used in DNS lead us to catch the turbulence scales down to Kolmogorov dissipative scale. But these types of simulations need large computing resources accessible through supercomputers.

DNS of TBLs at high Reynolds number similar to the ones accessible experimentally in large facilities is not yet possible due to the limitation of available computational resources. Furthermore, very accurate simulations such as DNS of flows around complex shapes are extremely difficult to perform. DNS of flat channel flow up to $Re_\tau \approx 5200$ are now available [81] and DNS over a flat plate have been performed for a wide range of Reynolds number [131, 132, 125] but are limited to $Re_\tau \simeq 2000$ up to now.

Large Eddy Simulations (LES) were proposed to overcome the extremely high cost of DNS. The meshing and time resolutions required for LES are reduced, as only the most energetic large-scale turbulence motions are explicitly resolved and the smaller ones are modeled. LES gives accurate results suitable to different studies with a much lower cost compared to DNS. So, in theory a higher Reynolds number can be reached.

However, the main difficulty to perform LES of wall-bounded flows comes from the simulation of the near-wall region which requires a high spatial resolution to accurately resolve the scales responsible of the kinetic energy peak. To overcome this important cost, the near-wall region is usually modeled instead of fully resolved. However, the main difficulty comes from the fact that it is very difficult to derive universal dynamical models for this near-wall region where the flow dynamics is rather complex. This is particularly true for wall-bounded turbulence on curves or complex geometries. For more details about the LES implementation strategies and sub-grid scale models, the reader can refer to Sagaut [122].

The last approach is the Reynolds Averaged Navier-Stokes (RANS) method. This method significantly reduces the computational costs and gives approximate time-averaged solutions for the Navier-Stokes equations. In this approach turbulence at all relevant scales is fully modeled, and prevents to simulate the dynamics of turbulent structures. The RANS equations are obtained by applying a Reynolds

decomposition, which decomposes an instantaneous velocity and pressure into its time-averaged and fluctuating parts. These equations are similar to the original Navier-Stokes equations but include additional terms in the momentum equations, the Reynolds stress tensor, which is unknown and needs to be modeled.

Several families of models have been proposed depending on the strategy to model these Reynolds stress terms. The most popular models are the eddy viscosity models (EVM) based on Boussinesq's hypothesis. One can distinguish several categories of EVM models based on the number of additional equations to solve. The one-equation RANS models solve one turbulent transport equation, usually the turbulent kinetic energy however other choices are possible as for the model proposed by Spalart and Allmaras [142] which solves a transport equation for a viscosity-like variable (other models can be found in [8, 48, 114]). The most popular methods are within the family of the two-equation models which require solving two extra equations for two quantities (traditionally linked to the kinetic energy and the dissipation). In order to prevent the use of the turbulent viscosity hypothesis, the Reynolds stress models solve an equation of each component of the Reynolds stress tensor and usually an extra equation for the dissipation. In spite of the number of equations to solve the cost of a RANS simulation usually remains much less than for an LES as the equation are solved on a much coarser mesh. It is important to note that RANS modeling is enough for most engineering applications that need the prediction of the mean flow and the effects of turbulence. An overview of RANS models can be found in Wilcox et al. [164].

Hybrid methods combining LES and RANS have been developed to retain the accuracy and time dependence of LES in the regions away from the walls but with reduced computational cost. This approach can take into account the unsteadiness of turbulence in engineering applications, for example, the prediction of noise propagation and dynamic loads in the aeronautical industry. RANS models are used in regions where LES requires very fine grid resolutions, especially near the walls. Several possibilities exist to link the RANS and LES domain. An explicit coupling can be used to define a-priori the domain in which the RANS and LES are solved. An alternative is the DES methods [141] for which the model is able to switch from a RANS formulation to an LES one based on a local property of the grid and/or of the flow.

2.2.3 Townsend-Perry theory

Townsend [152] developed a theory to scale the Reynolds stress tensor components, in which it is the wall-attached eddies of size proportional to the wall-distance y that contribute to the turbulent flow motion. The author assumed that the majority of

energy-containing motion is provided by the contributions of these attached eddies with similar velocity distributions. This theory starts from the hypothesis that an inertial range must exist within the turbulent boundary layer; for $\delta_\nu \ll y \ll \delta$, which is independent of both ν and δ. This range is generally located in the overlap region.

A first approximation was proposed by the author, based on the momentum equation, in which the Reynolds shear stress is considered as a constant $\langle uv \rangle = -u_\tau^2$. In order to ensure the turbulence equilibrium hypothesis ($P = \epsilon$), the dissipation rate is taken to be inversely proportional to the distance from the wall. The previous approximation leads to impose a mixing length-scale proportional to the wall distance via wall-attached eddies. The attached eddies correspond to large energy-containing scales responsible for turbulent mixing (not for turbulent dissipation which occurs at scales close to the Kolmogorov scale slowly increasing with increasing wall distances).

The contribution of the wall-attached eddies to the Reynolds shear stresses is given in Townsend [152], as an integral formula based on the probability density of finding eddies with size y_a; where $\delta_\nu \ll y_a \ll \delta$. As $\langle vv \rangle$ and $\langle uv \rangle$ are constrained by the wall and the author proposed that the eddy probability density function is inversely proportional to the eddy size. Hence, the Reynolds stress terms are given by:

$$\begin{aligned} \langle uu \rangle &= u_\tau^2 \left(C_\infty + C_0 \ln \left(\delta / y \right) \right) & \langle vv \rangle &= E_0 \\ \langle ww \rangle &= u_\tau^2 \left(D_\infty + D_0 \ln \left(\delta / y \right) \right) & \langle uv \rangle &= -u_\tau^2 \end{aligned} \tag{2.25}$$

where C_∞, C_0, E_0, D_∞, and D_0 are constants which depend on the shape of the relevant eddy.

Perry and Chong [110] and Perry et al. [111] showed that the energy spectrum of streamwise velocity fluctuation at a wall-distance y, in agreement with Townsend's attached eddy hypothesis, scales as $E_{11}(k_1) \sim u_\tau^2 k_1^{-1}$ in the range $1/\delta < k_1 < 1/y$, where k_1 is the streamwise wavenumber. For higher wave numbers range, $1/y < k_1 < 1/\eta$, where η is the Kolmogorov microscale that refers to the small scales. The turbulent motion follow Kolmogorov's law which states that E_{11} is proportional to $\epsilon^{2/3} k_1^{-5/3}$ with ϵ is the turbulence dissipation rate. The largest scales of the flow are located in the low wave number range, where $k_1 < 1/\delta$, being independent of y and k_1.

Nickels et al. [107] stated that a -1 power law behavior in the energy spectra would occur when both inner scaling (based on the wall-normal distance y) and outer scaling (based on δ) are simultaneously valid over the same wavenumber range.

However, an extensive range of k^{-1} is not clearly visible in the very high Reynolds number experiments of Vallikivi et al. [154] in the Princeton superpipe data [93]. Moreover, the k^{-1} behavior was not observed in the fully developed pipe flow of Morrison et al. [97] ($5.5 \times 10^4 \leq Re_D \leq 5.7 \times 10^6$). These results were interpreted by Nickels et al. [108] as being because their measurements were not close enough to the wall; the authors stated that it is necessary to approach closer to the wall in order to observe the k^{-1} behavior.

Using the superpipe data at high Reynolds number of Princeton, Vassilicos et al. [156] proposed a new model that include a new k^{-m} range, $E_{11}(k_1) \sim u_\tau^2 \delta (k_1 \delta)^{-m}$ with $0 < m < 1$, at the lower bound (largest scales) of the traditional Townsend-Perry range, $1/\delta < k_1 < 1/\delta_1$. This new range would exist only for the very large Reynolds Number and in a limited near-wall region $y < y^*$ where y^* is function of the Reynolds number. This new range could be associated with the very large-scale structures of streamwise fluctuating velocity. This new predictive model was validated by several high-Reynolds-number turbulent boundary layer in Laval et al. [75].

The attached eddy structures proposed by Townsend and Perry have been the subject of many studies over the last few years. The main challenge is to identify a family of coherent structures associated with the concept of attached eddies. Perry and Chong [110] proposed a model based on a hierarchy of Λ-vortices which has been extended by Perry and Marušić [112] (see Fig. 2.2). However, Srinath et al. [145] have shown that the Townsend Perry k^{-1} range can be simply explained by a much simpler on-off model of streamwise fluctuating velocity structures as soon as their spacial distribution is space filling.

2.2.4 Coherent structures

Turbulent motions are characterized by a random interaction between a wide range of scales. Different models introduced the notion of turbulent eddies. Bradshaw [11], Kline et al. [68], and Townsend [152] were among the first to highlight the role of coherent structures. Nowadays, coherent structures are considered to play an important role and are the focus of many investigations in turbulence research.

Different types of coherent (or quasi-coherent) structures are summarized in the literature. They are located along the boundary layer covering a wide range of length scales. A brief overview of the commonly identified coherent structures is presented below.

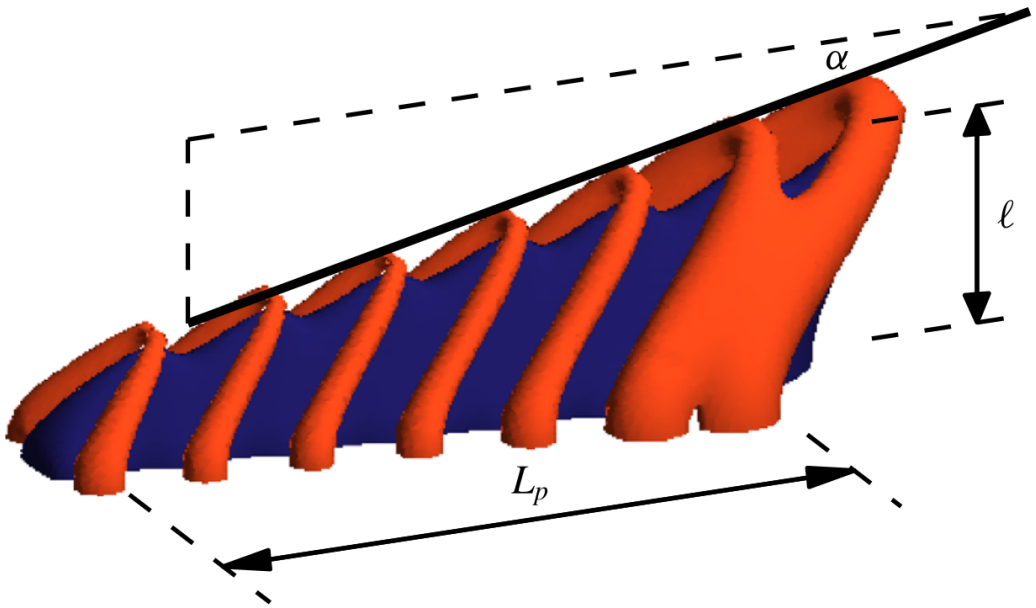

Fig. 2.2. Schematic of a typical hierarchies of eddies randomly distributed in groups or packets of hairpin vortices. (Reproduced from Silva et al. [133]).

Near-wall streaks

Streaks of high- and low-speed fluid, that are generally observed in the near-wall region of wall-bounded turbulent flows, are one of the earliest signs of the existence of coherent structures. Using a hydrogen bubble generating wire, Kline et al. [68] confirmed the existence of low-speed streaks in the buffer layer of turbulent boundary layers. They are also proposed mechanisms of the low-speed streaks formation and break-up as well as the interaction of the near-wall streaks with the outer part of the flow. The authors mentioned that "streaks interact with the outer portions of the flow through a process of gradual lift-up; then, sudden oscillation, bursting, and ejection". Here, bursting describes the interaction between near-wall streaks and the outer parts of the flow by a violent breakup of a low-speed streak after it is lifted from the wall.

Using experimental data, Kim et al. [63] showed the importance of low-speed streaks in generating turbulent kinetic energy. The production of turbulent energy in a region up to $y^+ = 100$ occurs during bursting times. The authors described the bursting process in three stages: lifting of the low-speed streaks, the growth of an oscillatory motion followed by breakup accompanied by a return to the wall. They are also associated with the essential energy transfer from the mean flow to the fluctuations during the oscillatory motion.

Using an instantaneous streamwise-spanwise plane, Robinson et al. [119] showed

that the low-speed streaks are more elongated (in the streamwise direction) and thinner (in the spanwise direction) than the high-speed ones.

In the literature, streaks are defined as being located in the near-wall region ($y^+ < 10$) and to have a height of the order of 50^+. In the streamwise direction, they are elongated from 500^+ to 2000^+ and have a spanwise width between 20^+ and 60^+ [15]. For more details about their statistics, one can refer to the experimental study of Lin et al. [84].

Using data from DNS of turbulent channel flow, Jiménez and Moin [61] investigated large-scale structures that are convected several thousand wall-units, during a very long timescale. The authors state that these observations imply that such structures are very stable and suggest that this may be related to the very long extent of the near-wall streaks in the streamwise direction observed in experiments.

A very detailed study of the characteristics of the near-wall streaks is made possible with the use of DNS. The near-wall streaks are known to play a significant role in the near-wall cycle of coherent structures generation and breakup in the buffer region. Schoppa and Hussain [128] conducted a very detailed stability analysis of a model of near-wall streaks to explain the streaks breakup.

Quadrants

Four distinct types of motions based on the decomposition of the Reynolds shear stress were introduced by Wallace et al. [161]. According to the signs of the streamwise and wall-normal velocity fluctuations, four quadrants are defined. The second quadrant motions ($u < 0$ and $v > 0$) and the fourth one (where $u > 0$ and $v < 0$) were associated with the ejection and sweeps motions.

A probability density function analysis of the components of velocity fluctuations shows that the probability of spending time in the second (Q_2) and fourth (Q_4) quadrants (where the product uv is negative) is much more than the others quadrants. In both quadrants, the negative product uv implies that these events produce turbulent energy, where the production of turbulent kinetic energy was defined as $P = -\langle uv \rangle \partial \langle U \rangle / \partial y$. Hence, Q_2 and Q_4 are considered as the significant turbulence producing motions.

Corino and Brodkey [26] realized that the main generation and dissipation of turbulence energy occur in the generation region of $5 \leq y^+ \leq 70$ and the origin of the fluid ejections was located in this region. They observed experimentally that these motions play an essential role in turbulence production and found that the size of the eddies increases with increasing distance from that region. The ejection motions always terminate with fluid entering from upstream towards the wall, which corresponds to the sweep event.

From hot-wire anemometry and conditional averaging, Wallace et al. [161] showed that sweeps contribute more to the production of turbulent kinetic energy in comparison to ejections in the region ($y^+ < 15$) and less as we move away from the wall $y^+ > 15$. Using a probability density function of the velocity, Jiménez and Hoyas [59] suggested that the increase in streamwise fluctuating velocity is caused by stronger ejections coming from the wall, rather than stronger sweep motions.

As defined in the previous section that ejection events are a process of lifting streaks from the wall. Kline et al. [68] declared that the fluid ejection from the wall is considered to be the main mechanism of energy transfer between the near-wall and outer regions. It was noticed by Robinson et al. [119] that strong ejections seem to originate from the central part of streaks more often than from either end. The authors also showed that spanwise extent of the outer-region ejections ranges up to 200^+.

Vortices

A vortex is defined by Robinson et al. [119] as a coherent structure that exhibits instantaneous spiral or circular streamlines in a plane normal to its core. Vortical structures are commonly observed in all regions of turbulent flow but in various forms. They play an important role in the dynamics of the turbulent boundary layers.

Back to 1950s, Theodorsen [149] presented horseshoe-shaped vortices (also called hairpins) as "molecules" of turbulence. He represented the shape of the horseshoe vortex by a sketch showing its two legs attached to the wall and its head tilted and pointing downstream (see Fig. 2.3 reproduced from his paper).

Townsend [151] later published observation of coherent structures by interpreting the spatial correlations of the streamwise velocity fluctuation and concluded that the dominant structures near the wall are tilted eddies. He also proposed wall-attached vortices in the streamwise direction which are considered to be the legs of Theodorsen's horseshoe vortices.

Küchemann [70] described vortical motions as "the sinews and muscles of fluid motions", where they play an important role in the turbulence generation as well as in the exchange between the boundary layer regions. Ejections and sweeps have been shown to be associated with quasi-streamwise vortices located in the near-wall region of turbulent flows. The near-wall low-speed streaks are also associated with quasi-streamwise vortices that pushed the low-speed fluid away from the wall and induced the ejection events [10, 137].

Counter-rotating vortices that are oriented and inclined downstream are shown by Robinson [118] enclosing the wall layer. He also suggested that these vortices

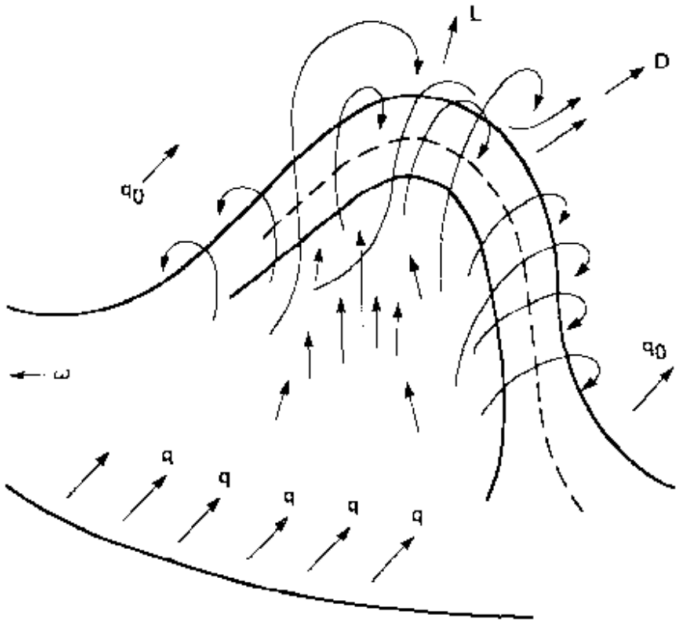

Fig. 2.3. Horseshoe vortex sketched by Theodorsen [149].

create and lift the near-wall streaks by creating cross-flows very close to the wall.

Smith et al. [138] proposed a model based on hairpin vortices by describing the fluid dynamics of the momentum exchange in the near-wall region of a turbulent flow. This model explains the processes of generation of new vortices and their growth to larger scales moving towards the outer region. They also noted that the majority of vortices in a TBL are asymmetric or single-legged hairpin vortices, while symmetric vortices rarely appear. The low-speed streaks were defined as traces of vortex interaction with the fluid in the wall-layer. More detailed eddy models are available in [110, 111, 112].

It was noted that the shape and size of hairpins depend on the Reynolds number as mentioned in Adrian et al. [2] and Head and Bandyopadhyay [49].

Various vortex identification methods have been proposed to distinguish vortex motions from other structures including vorticity. Several methods were summarized in Zhou et al. [173]. Hunt et al. [53] noted that the second invariant of the velocity gradient tensor, which is known as Q-criterion, can be used to identify vortices which measures the dominance of vorticity over strain. Another method, based on local pressure minima, was also proposed where the pressure in the vortex core is lower than that outside the vortex boundary. Chong et al. [19] investigated a vortex core in relation to complex eigenvalues of the velocity gradient tensor. These complex quantities imply that the local streamline is closed or spiral shaped.

Large-scale motions

Using temporal correlation of the streamwise velocity fluctuation, Townsend [151] has investigated large-scale structures in wall-bounded flows. In the boundary layers, these structures can be classified into two categories: large-scale motions (LSM) and very large-scale motions (VLSM), where LSMs elongate in the streamwise direction from 1 to 3δ and VLSMs are larger than 3δ [65]. LSMs are generally located in the logarithmic and lower wake regions of TBL [55, 33]. Recently, several studies have been devoted to such structures which contribute significantly to the turbulent kinetic energy as well as to the Reynolds stresses for high Reynolds number turbulent flows [40, 58, 168].

The study of these structures and their organization is therefore essential to understand the physics of wall turbulence and to improve turbulent flow models. Using single-plane PIV measurements of a turbulent boundary layer on a flat plate, Adrian et al. [2] linked the origins of LSMs to the streamwise alignment of hairpin vortices in the form of packets that move forward with the same convective velocity and induce large regions of low speed between their legs, (see Fig. 2.4).

The existence of large-scale structures is linked with various observations and changes in the turbulent boundary layer behavior. Above the near-wall peak that appeared in the streamwise velocity fluctuation profiles, a local minimum or flattened region was observed at sufficient Reynolds numbers in the logarithmic region around $y^+ = 100$ [52, 55, 145]. This constant region is followed by a second outer peak that appears in the wake region as the Reynolds number increases. This outer peak is generally associated with large-scale structures [55]. The intensity of the outer peak largely depends on the Reynolds number and grows with increasing Reynolds number, whereas the inner peak is less affected by the Reynolds number variation.

A DNS of a channel flow with a sufficiently high Reynolds number ($Re_\tau = 5200$) has been achieved by Lee and Moser [81]. However, the implementation of a DNS of a turbulent boundary layer on a flat plate is still more complicated and therefore restricted to moderate Reynolds numbers. The behavior of very large-scale structures obviously depends on the Reynolds number, and they are expected to have an increasing impact on the flow dynamics at very high Reynolds numbers. However, these very large Reynolds numbers are not yet accessible by DNS. But DNS remains an essential tool for studying the spatial and temporal organization of these structures at moderate Reynolds numbers [34, 125, 131] large enough to see the emergence of these very large-scale structures. As an alternative to DNS, higher Reynolds numbers have been achieved using wall-resolved large eddy simulations (LES) [115], but the spatial resolution was not sufficient to study coherent structures down to the buffer region.

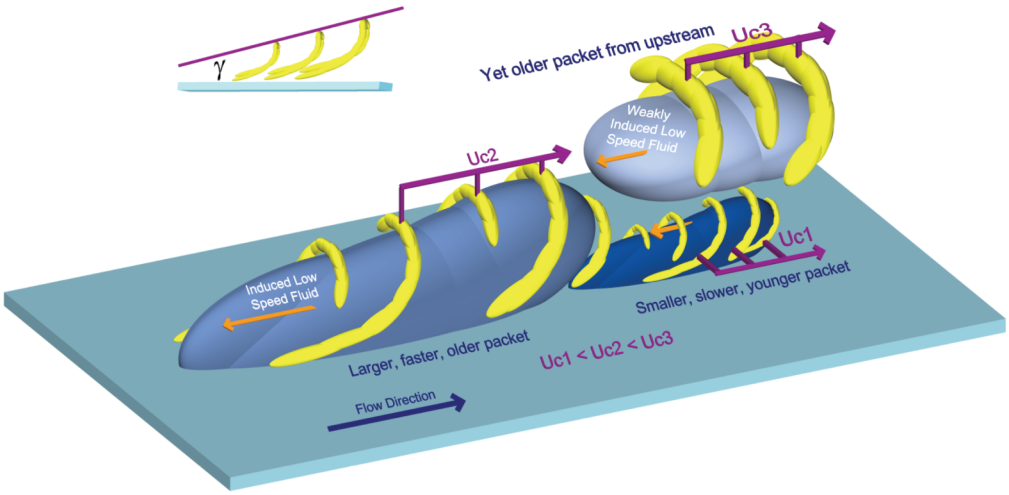

Fig. 2.4. Conceptual model of nested packets of hairpins vortices growing up from the wall. (Reproduced from Adrian et al. [2]).

Observations based on space-time velocity correlation are commonly used to highlight the presence of large-scale motions. Two-point velocity correlation has been widely used to present a mean statistic of large-scale structures. The isocontours of the two-point correlation always exhibit an elliptical shape with a downstream tilt angle. Based on this average quantities the average angle of the LSMs is found in the literature to be from 9° to 33° [13, 20, 26, 37, 44, 62]. This large variation in the mean angle depends on the importance of the Reynolds number and the history of the pressure gradient, knowing that an adverse pressure gradient can significantly increase the angle of the LSMs (Comparison of the two-point spatial correlation between ZPG and APG cases is presented and discussed in Chapter 5).

Lee et al. [80] investigated the large-scale motions using DNS of turbulent channel flows ($Re_\tau = 930$). They have related the production of VLSM to the merging of the LSMs. Balakumar and Adrian [7] found that VLSMs in pipe, channel and boundary layer flows have almost the same behavior, implying that they result from similar mechanisms. They also highlighted the importance of LSM and VLSM in the transfer of kinetic energy and shear stress. A significant portion of the kinetic energy $(40 - 65\%)$ and Reynolds shear stress $(30 - 50\%)$ is contributed by VLSMs in canonical flows [7, 45, 58, 77].

Using spectral information and probability density function from channel flow simulations up to $Re_\tau = 2000$, Jiménez and Hoyas [59] investigated the velocity fluctuations in the logarithmic and outer layers of turbulent channel flow. They have stated that the long-wavelength range of the streamwise and spanwise energy spectra scales with the half-width channel and associated these wavelengths with the very long structures. Del Álamo and Jiménez [31] observed in turbulent channel

flows VLSMs which extend up to $20h$, where h corresponding to the half-width channel.

In order to investigate TBL at an extremely large Reynolds number, Hutchins and Marušić [55] analyzed hot wire measurement in an atmospheric boundary layer. They found very large structures extending up to 20δ and largely located in the logarithmic region [55]. The very large-scale motions have been shown by Mathis et al. [92] to have a footprint down to the near-wall region. Using this observation of the correlation between the inner and the outer region they developed a model based on the concept of a universal inner region that is modified through modulation and superposition of the large-scale outer motions [91].

The large-scale coherent motions in boundary layers were investigated in [132] to focus on the large-scale structures in the outer layer and their influence on the near-wall motions. A three-dimensional representation of the two-point correlation of the streamwise velocity fluctuations for a boundary layer is reproduced from [132] in Fig. 2.5 where the reference point is located in the outer region ($y = 0.6\delta$). The middle elliptical shape represents the high-speed motion and the white ones corresponding to low-speed motions. In order to compare the characteristics of different turbulent flows, the two-point correlation C_{uu} conditioned on different intensities of u from channel and boundary layer flows was compared with the pipe flow simulation of Lee and Sung [77]. The authors found that far from the wall in channel flows, low-momentum structures are substantially longer than high-momentum ones, while both lengths are similar in pipe and boundary layer flows.

Large-scale motions have been considered to be responsible for the k_x^{-1} behavior of the streamwise velocity spectrum [139] and thought to be the attached eddies discussed in the model of Townsend [152] (this model is detailed in section 2.2.3). Using spectral coherence analysis for relatively high Reynolds number TBL flows, universal wall-attached structures have been identified in [5]. The authors emphasize the need for an unobstructed view of a k_x^{-1} scaling that is consistent with such a self-similar wall-attached eddy structure.

Although the general extent of large-scale structures is almost kept for a long time, the detail of the complex shape of these structures may evolve more rapidly. For this purpose, several methods have been used to identify the existence of large-scale motions and to detect their shape accurately. Spectral decomposition method is used in Abreu et al. [1] to extract the coherent structures from DNSs of Pipe flow at $Re_\tau = 180$ and 550.

The large-scale motions of streamwise velocity fluctuations u are detected in Solak and Laval [140] using a method based on simple threshold of u. The data was extracted from DNS of flat plate TBL up to $Re_\theta \sim 2500$. In order to investigate the effect of detecting meandering large-scale structures from 1D hot-wire measurement

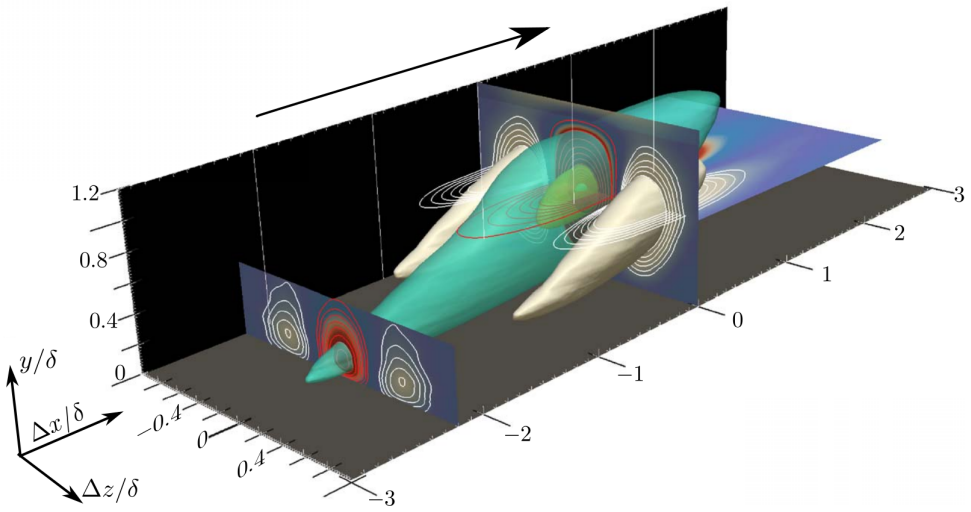

Fig. 2.5. Three-dimensional representation of the correlation of the streamwise velocity fluctuations, for a boundary layer at $y = 0.6\delta$ corresponding to $y^+ = 1530$. (Reproduced from Sillero et al. [132]).

or 2D PIV, statistics of 2D and 3D detection methods are compared and a good equivalence was shown between the two methods.

2.3 Effect of pressure gradient

Although turbulent boundary layers subjected to an adverse pressure gradient are present in a large variety of flows in many industrial problems, the majority of studies have been performed on canonical wall-bounded flows with zero or low pressure gradient. This is mainly due to the complexity of studying flows subjected to an APG compared to canonical ZPG flows. The presence of a pressure gradient in wall-bounded flows is mainly caused by the wall curvature. Since the pressure gradient in the streamwise direction dominates in other directions, we only consider the streamwise pressure gradient in our studies. At the edge of the boundary layer, a relationship between external velocity U_e and pressure P_e has been established by Bernoulli's equation:

$$\frac{\partial P_e}{\partial x} = -\rho U_e \frac{\partial U_e}{\partial x} \tag{2.26}$$

In addition to the ZPG case, two cases of pressure gradient occur. Firstly, the favorable pressure gradient (FPG) corresponds to a decrease in pressure ($\frac{\partial P_e}{\partial x} < 0$) and an acceleration of the flow ($\frac{\partial U_e}{\partial x} > 0$). The FPG tends to reduce turbulence and a strong FPG can change a turbulent flow to laminar. Secondly, the adverse pressure gradient (APG) case, $\frac{\partial P_e}{\partial x} > 0$ leads to decelerated flow and an increase in turbulence. For example, in the aeronautical industry, the forward part of an airfoil

corresponds to the FPG case, but its downstream part is subjected to APG. One effect of an APG is to increase the growth rate of the boundary layer thickness.

A non-dimensional pressure gradient parameter is defined by Clauser [23] as

$$\beta = (\delta_1/\tau_w)\partial P_e/\partial x. \tag{2.27}$$

This parameter represents the "intensity" of pressure gradient normalized by inner variables. This parameter can be interpreted physically as the ratio between the pressure forces and the shear stress. Also, the three categories of TBL can be related to β, where $\beta = 0$ in the absence of pressure gradient (ZPG), $\beta < 0$ in FPG cases and for an APG, $\beta > 0$. When a TBL is exposed to a very strong APG ($\beta \to \infty$), the flow separates from the wall. This flow separation is generally undesired to achieve good aerodynamic performance in aeronautical applications. Reverse flows have been observed close to the wall in turbulent channel and boundary layer flows with zero or small pressure gradient [166, 167] and up to the log layer for a strong adverse pressure gradient TBL [12].

Detailed studies of the effects of APG on the various parameters of TBL have been proposed by Mellor and Gibson [95] and Mellor [94]. The APG is represented by the pressure gradient parameter β and the exponent of the power law which states that the streamwise velocity (U) far from the wall changes proportional to the streamwise position x, this law is given as

$$U(x) \sim x^m \tag{2.28}$$

where the exponent m changes depending to the intensity of the pressure gradient. The effects of both m and β on the velocity defect was shown for a wide range of pressure gradient ($-0.5 < \beta < \infty$) using several experimental cases.

In order to better understand the effects of APG on the turbulence properties of a boundary layer, a lot of experimental and numerical studies were performed for a wide range of Reynolds numbers and pressure gradients. However, due to the difficulty to implement a well defined APG in numerical simulations more DNSs are available in the literature on a flat plate with ZPG.

The first DNS with APG was produced by Spalart and Watmuff [144]. A non-self-similar attached APG TBL up to $Re_\theta = 1600$ was simulated with $\beta = 2$. The Reynolds stress profiles and the momentum balance were compared with experimental data. A comparison of the mean velocity profile shows that a favorable pressure gradient shifts up the U^+ profile in the buffer and lower log region, and down in APG TBL. They also stated that there is no way to distinguish a buffer-layer effect from one that persists in the logarithmic layer because of the low Reynolds number

obtained in the DNS.

As the parameter β is directly linked to the exponent of power law m of the decelerating velocity in a TBL with APG, Tennekes and Lumley [148] proposed the relationship (2.29) between these two parameters based on a linear analysis

$$m = -\frac{\beta}{1+3\beta} \tag{2.29}$$

Non-linear analysis of the TBL equations was performed by Skote et al. [136] in order to relate both previous parameters with the shape factor which is also used to identify the importance of a pressure gradient. Equation (2.30) was found, and better agreement than the previous formula is reported. In this study, the turbulent statistics of two APG cases are compared with a reference ZPG case. The APG data are obtained from two DNS at low Reynolds numbers (up to $Re_\theta = 690$) of self-similar TBL that is subjected to low APG ($\beta \approx 0.24$ and $\beta \approx 0.65$). The constant streamwise pressure gradient is obtained by changing the freestream velocity according to the power law.

$$m = -\frac{\beta}{H\,(1+\beta)+2\beta} \tag{2.30}$$

Skote and Henningson [135] suggested a method to impose an APG by adapting the boundary condition for numerical simulations of flat plate TBL. This condition was validated by performing a DNS of attached TBL and another one which separates over a large part of the domain. Through an analysis of the turbulent kinetic energy and its production at several streamwise positions, the authors show that the near-wall flow depends mainly on local parameters rather than on the history of TBL.

Kitsios et al. [67] performed a DNS of flat plate TBL at Reynolds number up to $Re_\theta = 13800$ that is subjected to a strong APG at the edge of separation ($\beta = 39$). As the use of a curved wall in high accuracy simulations is difficult, the authors obtained APG by applying a wall-normal velocity suction at the top of the computational domain opposite to the wall. The velocity suction is calculated based on a potential flow solution of an expanding duct. The detail of this method will be summarized in chapter 3. The effects of increasing pressure gradient are shown in the mean streamwise velocity profiles and the Reynolds stress terms in comparison to another mild APG TBL ($\beta = 1$) [66] and ZPG one. By analysis of the streamwise averaged momentum terms for the strong APG TBL, the authors noticed that in the inner region the viscous term ($-\nu\partial_y\partial_y\langle U\rangle$) is positive, the Reynolds stress gradient ($\partial_y\langle uv\rangle$) is negative, and they are balanced with the positive streamwise pressure gradient. They have explained this by a net transfer of streamwise momentum from

the mean field to the fluctuating field. They show that a net momentum transfer from the fluctuating field to the mean field occurs in the outer region. Since the viscous term becomes negligible and the $(\partial_y \langle uv \rangle)$ term reaches a positive outer peak in balance with the convective terms. They also reported that the transfers of the wall-normal momentum are reversed from those of the streamwise momentum.

An analysis of three large-defect APG TBLs was presented by Gungor et al. [47]. One of them was obtained from a DNS of APG TBL at moderate Reynolds number $Re_\theta = 1003 - 4638$ starting from a recycling plane of an auxiliary DNS ZPG TBL. Their study showed that the transferring of turbulent energy from the mean flow to turbulence in the outer region is less efficient in large-velocity-defect than in ZPG cases, since all Reynolds stresses decrease with the increase of the velocity defect in the outer region.

2.3.1 Influence of APG on TBL statistics

The global organization of boundary layer as discussed in section 2.2.1 is globally the same in the presence of small to moderate adverse pressure gradient. However, the range of definition, as well as the property of each approximated law, will be modified by the presence of a pressure gradient.

According to Durbin and Belcher [35], the separation of the boundary layer into inner and outer parts, based on relative strength of viscous forces, might not be valid anymore when the boundary layer is subjected to a strong APG. The authors emphasized the need for a middle region to match the near-wall region with the wake layer of the TBL because the overlapping between the inner (with the wall-unit scaling) and outer region (scaled by the boundary layer thickness δ) leads to the following contradiction, $\delta \sim L$, where L is the streamwise length scale.

Since the fluctuations vanish at the outer edge of the boundary layer, integration in the wall-normal direction of equation (2.11) leads to the formation of the following equation:

$$P + \rho \langle vv \rangle = P_e \tag{2.31}$$

As the streamwise gradient of wall-normal Reynolds stress is almost negligible, the streamwise pressure gradient can be substituted by its value at the edge of boundary layer:

$$\frac{\partial P}{\partial x} \approx \frac{dP_e}{dx} \tag{2.32}$$

Close to the wall, in the presence of APG, the equation (2.10) can then be simplified to

$$\mu \frac{\partial^2 \langle U \rangle}{\partial y^2} - \rho \frac{\partial \langle uv \rangle}{\partial y} - \frac{dP_e}{dx} = 0 \tag{2.33}$$

Integration in the wall-normal direction of (2.33) by taking into account that $\tau = \tau_w = \rho u_\tau^2$ at the wall, leads to the equation which describes the inner region of TBL subjected to an APG

$$\mu \frac{\partial \langle U \rangle}{\partial y} - \rho \langle uv \rangle = \frac{dP_e}{dx} y + \rho u_\tau^2 \tag{2.34}$$

Viscous sublayer

In the viscous sublayer that is very close to the wall, where viscosity dominates the Reynolds stress term in the left-hand side of (2.34), a significant adverse pressure gradient makes the linear wall law no longer valid. The new law that represents the behavior of the mean velocity profile in the presence of an adverse pressure gradient becomes

$$U^+ = y^+(1 + \frac{1}{2} p^+ y^+) \tag{2.35}$$

where p^+ is the streamwise pressure gradient scaled by the inner quantities

$$p^+ = \frac{\nu}{\rho u_\tau^3} \frac{dP_e}{dx} \tag{2.36}$$

The equation (2.35) demonstrates that the second-order derivative of the mean velocity profile is positive at the wall for adverse pressure gradient ($p^+ > 0$). As the second-order derivative is necessarily negative in the outer part of the boundary layer, this implies that the mean velocity profile exhibits at least one inflection point at some distance from the wall.

Most of RANS models are generally based on the $U^+ = y^+$ equation, which only describes the cases of ZPG and low pressure gradient $\left(p^+ {y^+}^2 \ll 1\right)$. As the pressure gradient term in (2.35) cannot be neglected for a significant pressure gradient, these RANS models fail to correctly predict such flows.

In addition to the Reynolds number effects on the skin friction noted in [101], where C_f decreases with increasing in the Reynolds number, Vinuesa et al. [160] found that an increase of APG also leads to decrease the skin friction by comparing three turbulent boundary layers ($\beta = 0$, 1 and 2).

log-region

The logarithmic law has been derived for very large Reynolds number flows, however it is able to characterize flows in situations where this condition is not respected. The universality of this law is still questioned, especially for describing the mean velocity profile in presence of an adverse pressure gradient.

The effect of the pressure gradient is noticeable on the mean velocity profile in

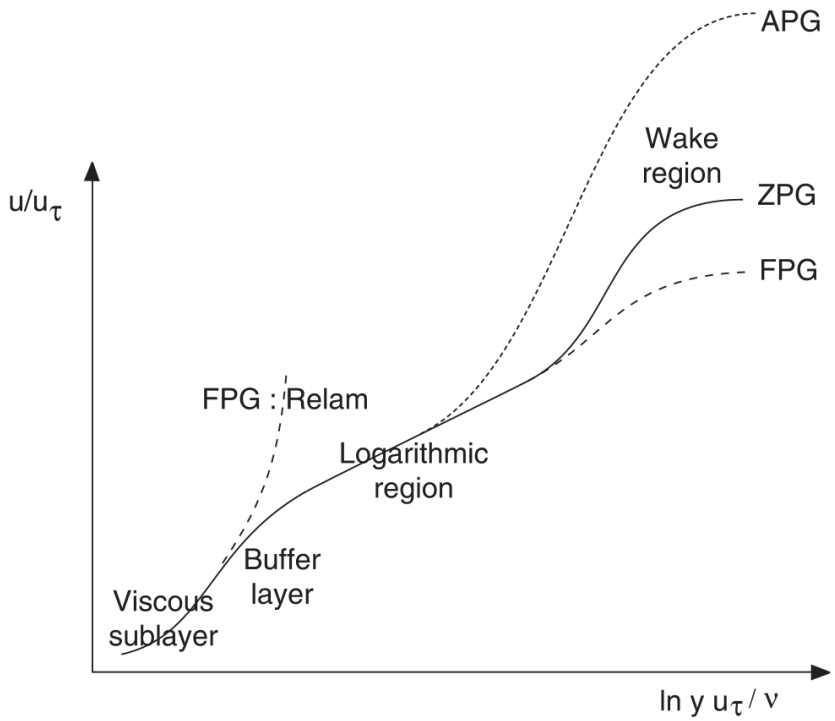

Fig. 2.6. Effect of various pressure-gradient on the mean velocity profile in a boundary layer. (Reproduced from Catris and Aupoix [18]).

the wake region where the deflection from the logarithmic behavior is smooth in the case of a favorable pressure gradient and becomes steeper with the increase in adverse pressure gradient. Catris and Aupoix [18] showed a comparison of the mean velocity profile between favorable, zero and adverse pressure gradient boundary layers (see Fig. 2.6). The dashed line (FPG: Relam) in the buffer layer corresponds to a very strong FPG case, where the flow returns to laminar (relaminarization) [103, 104]. The effect of the pressure gradient is clearly shown on the magnitude of the freestream velocity that must affect the extent of the logarithmic region. Brown and Joubert [14] and Huang and Bradshaw [51] have also reported an increase of the wake-region which reduces the extent of the log-layer. Kitsios et al. [67] noted that an increase of adverse pressure gradient reduces the extent of the logarithmic layer until the log-layer almost entirely disappears in the presence of a very strong APG.

In agreement with the experiments of Nagano et al. [99] and simulations of Spalart and Watmuff [144], Catris and Aupoix [18] stated that, in the case of a moderate pressure gradient, the slope of the logarithmic region κ_0 remains constant and the pressure gradient only affects the intercept of the log-law, C, in eq. (2.23).

However, using low Reynolds number turbulent boundary layers subjected to strong APG, Nickels [106] noticed that the presence of an APG alters both the slope and the intercept of the logarithmic region. He suggested a modified log-

law based on the observation of Clauser [22] that the sublayer grows up to reach a critical Reynolds number Re_c that is approximately the minimum critical Reynolds number of a laminar boundary layer. A critical wall-distance y_c was introduced which is corresponding to the sublayer edge and it was found to be $y_c^+ \approx 12$. For adverse pressure gradient, the logarithmic law defined in eq. (2.23) was modified by Nickels [106] through changing the constant κ_0. The relation of the variable slope κ_p is given by the following equation (the hypothesis and the derivation can be found in [106])

$$\kappa_p = \frac{\kappa_0}{\sqrt{1 + p^+ y_c^+}} \tag{2.37}$$

where p^+ is the streamwise pressure gradient defined in (2.36).

The modified log-law of a boundary layer with APG is then written as follows

$$U^+ = \frac{1}{\kappa_p} \log y^+ + C' \tag{2.38}$$

with C' is the new intercept of the logarithmic law, which changes simultaneously with κ_p as the pressure gradient increases. Moreover, in addition to the high resolution required to validate the new law (2.38), George [41] exposed another difficulty related to the Reynolds number to validate this law. They distinguish within the logarithmic region between the 'mesolayer' where the turbulence scales of motion remain affected by viscosity and the true 'inertial layer' where they separate approximately at $y^+ = 300$. Furthermore, a sufficiently large logarithmic law region is always required with a sufficiently strong pressure gradient, hence a very large Reynolds number. The authors concluded that $\delta^+ > 3000$ (corresponding to $Re_\theta > 10000$) is a necessary condition to investigate the logarithmic behavior in this region.

Effects on the Reynolds stress profiles

In addition to the effects of the pressure gradient on the mean velocity in the wall and log regions, the Reynolds stress profiles were also affected by the presence of the pressure gradient, especially the adverse one. Besides the near-wall peak that was observed in the streamwise turbulence intensity profile in all wall-bounded flows, a second outer peak was also noticed when a boundary layer is subjected to an adverse pressure gradient even at a moderate Reynolds number. Using a wind tunnel experiment of TBL subjected to a strong adverse pressure gradient ($\beta \sim 20$) up to $Re_\theta \simeq 50000$, Skåre and Krogstad [134] noticed an outer peak in the turbulence production rate located at $y/\delta \simeq 0.45$. They stated that this peak is due to the very high turbulent shear stresses found in the outer region. Moreover, for sufficiently

large adverse pressure gradient, this peak of production is associated with the peak of the Reynolds stresses that appeared at the same wall distance. Using results from a DNS of self-similar APG TBL, Kitsios et al. [67] noticed that an outer peak in all of the Reynolds stresses was located at approximately the same wall-normal position $y = 1.3\delta_1$ for the mild APG ($\beta = 1$) and at $y = \delta_1$ for the strong APG at the verge of separation. Furthermore, they noticed that this peak coincides with the outer inflection point of the mean streamwise velocity profile, suggesting instability of the shear flow. Moreover, the increase in the pressure gradient makes this peak more noticeable and spatially located.

George et al. [43] stated that the initial conditions and the way of imposing the APG have a significant influence on the position of the outer peak of the streamwise Reynolds stress. They also associated the position of this outer peak with the inflection point occurring in the mean velocity profile at approximately the same wall-normal distance. The effect of the pressure gradient on the turbulence statistics will be investigated in more detail in chapter 4 using the results of our new DNS with moderate pressure gradient.

2.3.2 Coherent structures in presence of APG

Furthermore, while turbulence was initially and mainly studied in canonical wall-bounded flows, these flows remain less understood than homogeneous or free shear flows. Hence, the dynamic of non-canonical wall-bounded flows such as APG TBLs is much less documented. The numerous existing studies on APG TBLs have generally focused on statistical properties rather than on investigating the coherent structures and their dynamics.

The near-wall low-speed streaks are still present in TBL with moderate APG as noticed by Kline et al. [68] in their experiment up to $Re_\theta = 1680$. These streaks appear to be shorter and more wavy in the presence of an adverse pressure gradient. They also mentioned that a favorable pressure gradient reduces the bursting rate, while an adverse pressure gradient tends to make these events more frequent and violent. Lian [82] investigated the coherent structures in APG TBLs using the hydrogen bubble technique. He noticed that in ZPG the high-speed streaks are relatively wider than the narrow low-speed ones, in agreement with the observation of [68]. However, in presence of APG, especially in the vicinity of separation, the low-speed streaks become wider and their width becomes comparable to that of the high-speed ones. Consistent with the results found by Na and Moin [98] and Spalart and Coleman [143], Skote and Henningson [135] noticed in their work that the near-wall streaks are reduced by the effect of an APG. Furthermore, the authors stated that even the streaks vanish at separation but they start to develop again

after reattachment.

A direct numerical simulation of a converging-diverging channel flow was performed by Marquillie et al. [90] at Reynolds number $Re_\tau \approx 617$. It is important to note that this DNS was the first one that was made using a curved shape to generate the pressure gradient and nowadays it is still rare to make this type of DNS as it is very difficult to perform. Just after the onset of the APG zone, regions of high kinetic energy production were found on both walls. By performing a streaks stability analysis, the peak in turbulent kinetic energy was then explained as a result of the increase of the streaks instabilities in the APG region leading to the generation of strong vortices (see Fig. 2.7).

In their experimental study, Krogstad and Skåre [69] noted that the importance of the second and fourth quadrants is comparable with the case of ZPG TBL. Whereas in the APG TBL, the Q_4 events (sweep motions) are more frequent and longer lasting than the motions of the other quadrants near the wall as well as in the lower part of the outer region. Using HW measurements, Skåre and Krogstad [134] found that large turbulent kinetic energy production occurred in the outer layer of a strong APG TBL in addition to the near-wall region. These observations are interpreted through the presence of strong turbulent shear stresses in the wake region (around 0.4δ) where $-\langle uv \rangle$ achieves $\sim 16^+$.

Moreover, three cases of strong APG TBLs were investigated in Gungor et al. [47]. They found that the Reynolds stresses and turbulence production rate reached their maximum in the middle of the boundary layer and not in the near-wall region. Investigation of the quadrants of the Reynolds shear stress reveals that sweeps dominate the ejection events in the near-wall region, whereas the outer region is dominated by ejections.

Starting from direct numerical simulations of a ZPG turbulent boundary layer and two equilibrium TBLs subjected to an adverse pressure gradient, Lee and Sung [79] investigated the statistics of low-momentum regions and hairpin vortex packets, as well as their sensitivity to the presence of APG. A three-dimensional analysis shows that the outer layer is populated by streamwise hairpin packets. The average tilt angle of the hairpin vortices was also evaluated and found to be 13° for the ZPG and 18.5° for the APG. Recently, the coherent vortices were identified by using the swirling criterion (λ_2) from the mild Reynolds-number well-resolved LES of Tanarro et al. [147], for two APG cases (NACA0012 and NACA4412) and one ZPG.

Several turbulent boundary layers with different moderate APGs ($\beta = 1 - 4.75$) have been performed in the experimental study of Monty et al. [96]. In the outer region, this investigation has shown that large-scale coherent structures of the streamwise velocity fluctuation contain more energy than small-scale ones based on a com-

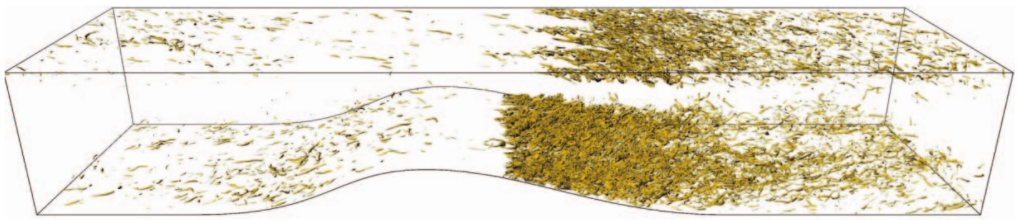

Fig. 2.7. Visualization of intense vortices generated in the APG region of the flow from a DNS of converging-diverging channel flow using a positive iso-value of the Q criterion. (Reproduced from Laval et al. [74]).

parison of the contribution of different scale coherent structures on the mean streamwise Reynolds stress (structures with streamwise length less than δ are considered as small-scale structures).

Furthermore, Lee [76] performed DNS of TBLs subjected to mild, moderate and strong APG to investigate the large-scale structures of the streamwise velocity fluctuations in the logarithmic region. Using two-point spatial correlations and instantaneous flow fields of the streamwise velocity fluctuations, he noted that the pressure gradient strongly affects the spatial organization of the streamwise velocity structures in the log layer, where increasing the APG ($\beta > 2$) clearly shows a reduction in the streamwise extent of the u-structures comparing to the mild APG ($\beta < 2$). Moreover, the increase in the spanwise length scale of large-scale structures for the mild APG TBL flow promotes the merging between the adjacent structures, which explains the increase in streamwise length scale for these structures in an APG flow compared to a ZPG one. Also, it was noticed based on skin-friction analysis that these large-scale structures in the log-region have stronger imprints on the near-wall region comparing to ZPG. On the other hand, Lee and Sung [79] have used two-point correlations and linear stochastic estimation to characterize the low-speed regions in both inner and outer layers in order to also investigate this type of coherent structures.

Hot-wire measurements of ZPG and three APG TBLs were performed by Vila et al. [158] to distinguish the effects of both APG and Reynolds number on the boundary layer. A scale decomposition analysis showed that for a sufficiently high Reynolds number, a large-scale spectral peak was shown in the outer region of both ZPG and APG TBLs with a streamwise wavelength of $\lambda_x/\delta_{99} \approx 6$, which is associated with high Reynolds numbers and another related to the APG effect $\lambda_x/\delta_{99} \approx 3$.

The coherent structures of streamwise velocity fluctuations are also investigated using data from DNS of an APG TBL ($\beta = 1.43$) of Yoon et al. [169] up to $Re_\theta = 5700$. The structures have been detected based on the root mean square of the

velocity fluctuation u_{rms} as a function of wall-normal distance y. In order to model the large-scale motions in the outer layer in TBL, Bross et al. [12] detected the uniform-momentum zones in an experiment of adverse pressure gradient turbulent boundary layer using time-resolved PTV measurements with high spatial resolution. The effects of large-scale motions on the reverse flows are discussed in detail herein, as well as the interaction between the near-wall and the outer structures.

2.4 Equilibrium boundary layer

Equilibrium boundary layer is considered as important academic case to investigate even though there is no universal definition of "equilibrium". This notion was firstly proposed by Clauser [23, 22], assuming that equilibrium in a boundary layer is achieved when the pressure gradient parameter β is constant.

Most of the theoretical studies focus on equilibrium TBLs, especially in APG cases, as it is easier to link it to the Navier-Stokes equations, where all terms of the governing equations must maintain the same relative weight while the flow develops. However, most existing turbulent boundary layer flows are out of equilibrium since it is not easy to obtain and maintain an equilibrium in the flow as length and time scales vary downstream and TBL parameters are interrelated.

Bradshaw [11] showed that in order to maintain equilibrium in a turbulent boundary layer, a necessary condition is that the contribution of the pressure gradient to the momentum deficit growth must be proportional to the contribution of the wall shear stress. Furthermore, it has been shown that this stress implies that the parameter β is constant. Clauser [22] and Lee [76] observed that a boundary layer in equilibrium state must have a self-similar velocity-deficit profile $(U_e - U)/u_\tau = f(y/\delta)$. Furthermore, according to the theories of Mellor and Gibson [95] and Townsend [150], a sufficient condition for β to be constant is that the freestream velocity (U_e) distribution follows the power law (2.28).

Skote et al. [136] and Lee and Sung [78] present results from a numerical simulation for an equilibrium boundary layer. They imposed a quasi-constant pressure gradient along the simulation domain by prescribing a free-stream velocity distribution following the power-law. Furthermore, self-similarity analysis was done for the DNS data of the strong APG boundary layer of Kitsios et al. [67], where different quantities were found to be independent of the streamwise direction.

Townsend [150] also shows that if β is constant, the shape factor $H = \delta_1/\theta$ must be a constant and δ_1 should vary linearly in the streamwise direction. Both of these results have been verified experimentally by Clauser [23] and Skåre and Krogstad [134]. Castillo and George [16] have shown that most TBLs seem to

be in equilibrium if the latter is established when the pressure gradient parameter Λ = constant. The behavior of this parameter has been tested and analyzed in more detail in section 4.2.1. Other parameters have also been proposed such as the Clauser factor G defined as

$$G = \frac{H-1}{H\sqrt{C_f/2}}. \tag{2.39}$$

The streamwise pressure gradient parameter scaled by the viscous quantities p^+ (2.36) can also be used to identify an equilibrium boundary layer.

In absence of an analytical solution of the Navier-Stokes equations, several similarity laws are proposed to describe the boundary layer, which give us a partial overview. But we still do not know the conditions where these laws are valid for corresponding velocity defect, i.e. which pressure gradient parameter is better to use? in which Reynolds number range? what is the physical meaning of the parameters used to normalize the TBL quantities? in addition to the effect of upstream conditions. In order to answer the different questions, a lot of studies are dedicated to the scaling of different wall-bounded turbulent flows. Numerous velocity and length types of scalings have been proposed in the literature.

The wall-unit scaling based on the friction velocity u_τ and the kinematic viscosity ν is efficient to collapse the profiles of different cases in the inner region, especially in canonical ZPG flows. However, the important challenge is still to find an appropriate scaling of the different quantities in the outer layer, where the mean velocity and its fluctuations depend on the Reynolds number and the presence of adverse pressure gradient.

A deep investigation will be presented in chapter 4, in which various velocity scales will be discussed and analyzed in detail.

Chapter 3

Direct Numerical Simulation

A Direct Numerical Simulation of a turbulent boundary layer on a flat plate subjected to an adverse pressure gradient has been performed up to $Re_\theta \sim 8000$. The parameters of the simulation were chosen to generate original databases. These databases will contribute to better access to the effect of mild pressure gradient in a TBL out of equilibrium. Time-resolved velocity components in a normal plane from a precursor DNS of ZPG TBL [140] at $Re_\theta \sim 2250$ was used as inlet boundary conditions for this new DNS. This allows us to reach a fairly large Reynolds number in the downstream part of the simulation domain.

The present DNS was performed with the open-source code INCOMPACT3D[1]. The characteristics and the parameters of the code are detailed below. More details about the code can be found in Laizet and Lamballais [71] and Laizet and Li [72].

Because of the complexity of simulating turbulent boundary layer flows, the first DNS were understandably performed without pressure gradient. This is only recently that the first DNS with an adverse pressure gradient have emerged. Some of these DNS as well as a small selection of relevant experiments are summarized in Table 3.1 and classified from oldest to newest one. Firstly, the DNS of Spalart and Watmuff [144] is the first DNS performed for an APG TBL. It has a pressure gradient coefficient $\beta = 2$ comparable to the current study with a lower Reynolds number. Skote et al. [136] have realized the first DNS of a self-similar boundary layer subjected to an APG. Recently, due to the increase of computational resources, much larger Reynolds numbers have become possible. The DNS of Kitsios et al. [66] presents a TBL subjected to low APG and the second DNS of Kitsios et al. [67] represents a very strong APG TBL at the verge of separation up to $Re_\theta = 13800$ which represents the largest Reynolds number obtained from a boundary layer DNS. The DNS of Lee [76] and the experiment of Srinath et al. [145] have an APG strength close to that obtained in the present DNS. The experiment of Bross et al. [12] has

[1] http://www.incompact3d.com/

Table 3.1. Summary of a selection of TBL subjected to an APG.

Authors	Year	Data	β	Re_θ
Spalart and Watmuff [144]	1993	DNS	2	1600
Skote et al. [136]	1998	DNS	0.65	$430-690$
Kitsios et al. [66]	2016	DNS	1	$300-6000$
Kitsios et al. [67]	2017	DNS	39	$570-13800$
Lee [76]	2017	DNS	2.2	2180
Srinath et al. [145]	2018	Exp.	2	$1720-23430$
Bross et al. [12]	2019	Exp.	13.5	11500

a Reynolds number comparable with that achieved in the current study although it has a stronger pressure gradient, which allows us to distinguish Reynolds number effects from APG ones.

3.1 Numerical code

INCOMPACT3D is an open-source code written in FORTRAN 90 that solves the incompressible Navier-Stokes equations. The code was optimized to work on the massively parallelized supercomputers using the powerful 2DECOMP&FFT[2] library. 2D domain decomposition strategy using "pencils" is used to parallelize the computation as shown in Fig. 3.1 in order to run larger simulations and/or to significantly reduce the wall clock time of the simulations [72]. Each variable is flipped from one configuration to another several times during one time step in order to compute the derivatives along the direction of the pencils. However, the method which prevents ALLTOALL communications is very efficient even with a large number of computing units. Note that this decomposition method does not lead to any changes in the derivation/interpolation routines or in the solution of the Poisson equation since the calculations are performed in the same spatial direction at a time. INCOMPACT3D is a high-performance tool that allows to perform DNS with up to $O(10^5)$ computational cores through this efficient 2D domain decomposition. The efficiency of the code was assessed up to 1 million cores on several super-computers using a large number of simulations [72].

Sixth-order compact finite difference schemes are used to calculate the spatial differentiation (derivative and interpolation). Moreover, third-order Adams-Bashforth explicit scheme was used for the time advancement (third and fourth-order Runge-Kutta schemes are also available). Furthermore, the explicit type of time discretization does not produce any particular problems in terms of adaptation to parallel

[2] `http://www.2decomp.org`

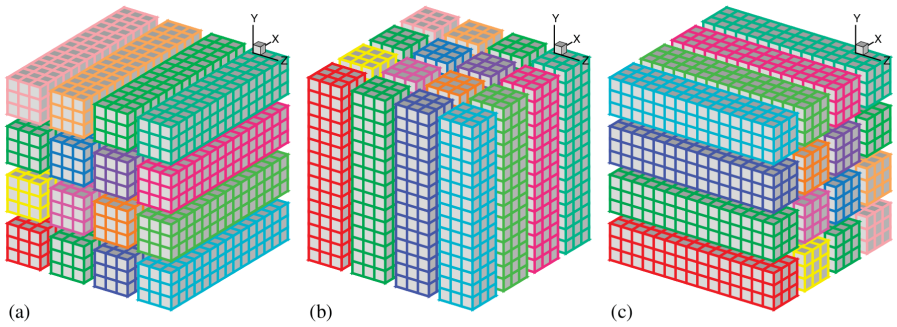

Fig. 3.1. 2D domain decomposition strategy used in INCOMPACT3D, (a) x-pencils, (b) y-pencils, and (c) z-pencils. (Reproduced from Laizet and Li [72]).

computation.

Fractional step method [64] is used to ensure the incompressibility condition and the pressure is computed by solving the Poisson equation. It is important to note that solving of the Poisson equation in physical space using sixth-order compact schemes can be computationally very expensive and not necessarily simple to implement, especially for simulations with several billion computational nodes. To overcome this problem while preserving sixth order accuracy, the Poisson equation is solved entirely in spectral space using the Fast Fourier Transform (FFT) libraries. The library FFTW[3] which is a C subroutine for computing the discrete Fourier transform in one or multiple dimensions was used in the code. The use of FFT subroutines does not affect the scalability of the code and it is much faster than solving the pressure in physical space [72].

In order to reduce the oscillations in the pressure field, a staggered mesh is used where the pressure field mesh is shifted by a half grid distance in each direction from the velocity one. This staggered mesh for the pressure field, first proposed by Fortin et al. [38] and then used by Almgren et al. [3] for second order schemes, is quite simple to implement with the use of sixth order interpolators and fast Fourier transforms [146, 165].

Using a stretched mesh in one spatial direction is quite simple to implement for a traditional finite difference scheme. But as the Poisson equation is solved in Fourier space in the code and a staggered mesh was used, the implementation of a stretched meshing must also work in Fourier space as well as in physical space. In order to solve this problem, a new uniform coordinates s is used and related to the physical coordinates by a stretching function as $x = h(s)$. This function was chosen based on single parameter β_{str} (see definition in [71]) to make an equivalence between spectral and finite difference operators. In the current case, a non-homogeneous (stretched) grid was used in the wall-normal direction with $\beta_{str} = 9$. The numeric and algorithm

[3] `http://www.fftw.org`

used in the code is described in more detail in [71, 72].

3.2 Parameters of the DNS

This section includes the numerical setup and parameters that are used in the simulation, the boundary conditions applied to the borders of the computational domain, as well as the spatial resolution.

As usual, x, y and z are used as the positions in the streamwise, wall-normal and spanwise directions respectively and U, V and W are the corresponding instantaneous velocity components.

3.2.1 Boundary conditions

As in all numerical simulations of TBLs over a flat plate, a no-slip boundary condition

$$U|_{y=0} = 0,\ V|_{y=0} = 0,\ W|_{y=0} = 0$$

is applied at the bottom surface ($y = 0$) which represents the wall over which the boundary layer will develop. A periodic boundary condition was also applied in the homogeneous spanwise direction.

3.2.1.1 Far-field wall-normal velocity boundary condition

Several possibilities exist to generate an adverse pressure gradient. One is to simulate a flow over a curved wall. This was done for instance by Marquillie et al. [90] for a channel flow configuration. However, for an accurate description of the near-wall flow, the mesh should follow the curvature of the wall. In the case of Marquillie et al. [90], this was done by using a mapping of coordinate combined with an efficient algorithm. For the current study, a more conventional but efficient solver on a cartesian grid was chosen in order to reach a significant Reynolds number on a large simulation domain. In this case, the only option is to generate the adverse pressure gradient by prescribing a wall-normal velocity for the top boundary condition parallel to the wall.

A wall-normal suction velocity at the far-field boundary was proposed by Kitsios et al. [67]. It is based on a potential flow solution in an expanding duct and was corrected to compensate the boundary layer growth.

Referring to Mellor and Gibson [95], the outer reference velocity must be proportional to $(x - x_o)^m$, where the exponent $m = -0.23$ in the case of flow at the edge of separation, and x_o is the virtual origin of the boundary layer.

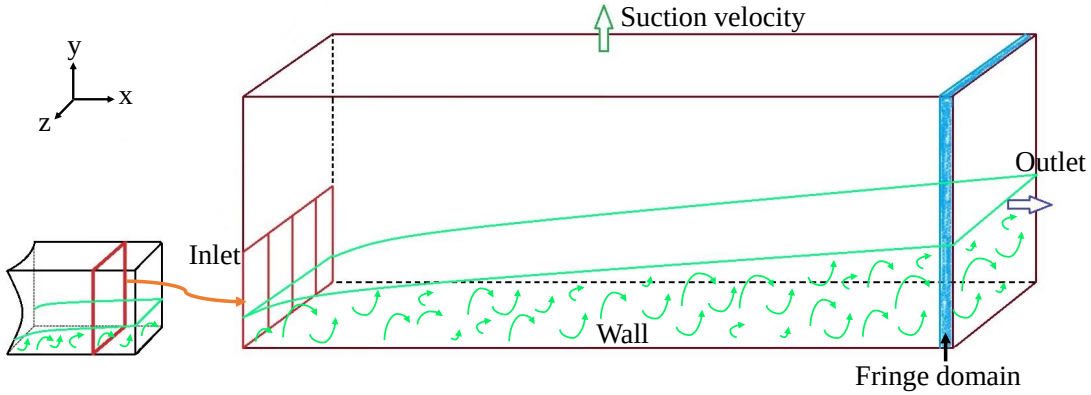

Fig. 3.2. Configuration of the simulation box.

The stream function along with the centerline of the duct is given by

$$\psi_{PF}(\hat{x},\hat{y}) = Ar^{m+1}\sin(\gamma), \tag{3.1}$$

where the constant A is a scaling parameter, $r^2 = \hat{x}^2+\hat{y}^2$, and $\gamma = (m+1)\arctan(\hat{y}/\hat{x})$, with $\hat{x}$ and $\hat{y}$ are the streamwise and wall-normal coordinates respectively. The superscript $(\hat{.})$ has been used here for the potential flow coordinates to distinguish them from the DNS coordinates used below.

The streamwise (U_{PF}) and wall-normal (V_{PF}) components of general potential flow were calculated by derivation of the stream function (3.1).

$$U_{PF}(\hat{x},\hat{y}) = \partial_y\psi_{PF} = A(m+1)[\hat{x}r^{m-1}\cos(\gamma) + \hat{y}r^{m-1}\sin(\gamma)], \tag{3.2}$$

$$V_{PF}(\hat{x},\hat{y}) = -\partial_x\psi_{PF} = A(m+1)[\hat{y}r^{m-1}\cos(\gamma) - \hat{x}r^{m-1}\sin(\gamma)]. \tag{3.3}$$

As this potential flow solution does not account for the boundary layer growth, it must be corrected by the displacement thickness which grows linearly along the TBL as the functional form $\delta_1(x) = K(x - x_o)$, where K is the growth rate of δ_1. In the present case, we choose to evaluate the value of K from experimental PIV data of Srinath et al. [145]. The mentioned experiment was performed in the LMFL wind tunnel to study the TBL over a ramp with an inclination of $-5°$. A moderate adverse pressure gradient was obtained and the flow remained attached to the wall along the ramp. Using the parameters obtained from that study allows us to obtain an equivalent pressure gradient, which leads to focus on the effect of the APG, especially in the presence of different Reynolds numbers. However, it is not possible to obtain a high Reynolds number as in the experiment due to the limitation of computational resources. The value of $K = 0.01121$ was obtained by a linear fit of the displacement thickness profile of [145] as a function of the streamwise position.

Then, the potential flow coordinates $(\hat{x},\hat{y})$ are substituted by the DNS coordi-

nates (x, y), and the requiring relationship is given by

$$\hat{x} = x - x_o, \text{ and } \hat{y} = y - K(x - x_o). \tag{3.4}$$

The exponent m is chosen to create a moderate adverse pressure gradient. As mentioned in Skote et al. [136], the power-law exponent $m = -\frac{\beta}{H(1+\beta)+2\beta}$ was defined with an empirical value of the shape factor $H = 2.35$ from Mellor and Gibson [95]. $m = -0.2075$ was used in the boundary conditions of the present DNS to introduce a pressure gradient comparable to the experiment of Srinath et al. [145].

The virtual origin of the boundary layer x_o was estimated by extending back the streamline from the inlet boundary layer edge at the position $(x, y) = (x^I, \delta^I)$, to obtain $x_o = x^I - \delta^I \times U(x^I, \delta^I)/V(x^I, \delta^I)$, where $(.)^I$ represents the relevant quantity that is evaluated at the inlet position. $x_o = -80\delta_0$ is used as the virtual origin of TBL in the present DNS, where δ_0 is the inlet boundary layer thickness of the precursor DNS of ZPG TBL [140].

The parameter A in (3.2) and (3.3) is calculated using the modified potential flow solution $U_{PF}(x-x_o, y-K(x-x_o))$ that is obtained by substituting the relationships (3.4) into (3.2). In special case, the inlet position and the edge of boundary layer are replaced instead of the coordinates (x, y) respectively in the streamwise potential flow solution U_{PF}. Then, the parameter A was obtained by comparing U_{PF} with the inlet streamwise velocity at the same coordinates. The careful choice of this parameter provides a potential flow solution with the same scale as the inlet velocity.

The far-field wall-normal boundary condition as a function of the streamwise direction (x) is given as

$$V_\infty(x) = V_{PF}(x - x_o, y_\infty - K(x - x_o)). \tag{3.5}$$

The far-field BC along the streamwise direction is computed based on (3.5) and illustrated in Fig. 3.3 normalized by the free-stream inlet velocity.

The steady far-field wall-normal velocity should be prescribed to ensure the pressure stability which is very sensitive to any small change. On the contrary, the streamwise velocity must be calculated at each time step based on a zero spanwise vorticity condition that is applied to the top of the domain to obtain an irrotational flow at the far-field. The following equation was implemented as a Neumann condition at the top of the computational domain using one order Eulerian scheme.

$$\frac{\partial U_\infty}{\partial y} = \frac{\partial V_\infty}{\partial x} \tag{3.6}$$

Furthermore, using coarse mesh at the far-field can produce strong fluctuations

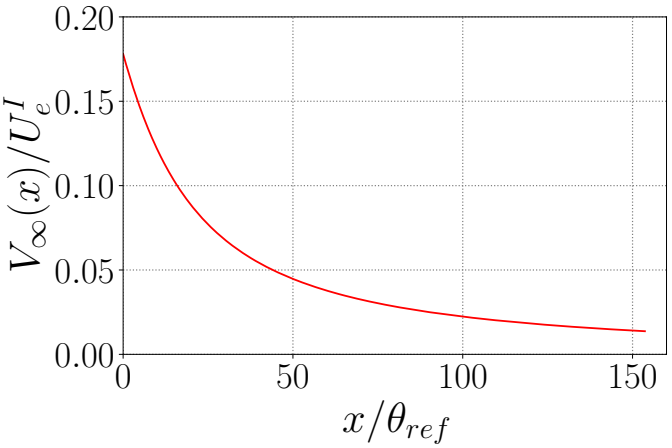

Fig. 3.3. Far-field wall-normal velocity boundary condition of the APG TBL DNS is scaled by the edge velocity at the inlet position. The streamwise position is normalized with the momentum thickness at the reference streamwise position θ_{ref} such that $Re_\theta = 7240$.

in the velocity field, especially close to the inlet where the implemented far-field normal velocity experience a fast decrease downstream as shown in Fig. 3.3. This provides a strong lack in the streamwise velocity referring to eq. (3.6).

3.2.1.2 Inlet conditions

In an APG case, the growth rate of the boundary layer is much larger than for a ZPG TBL. This is the reason why the simulation domain was extended two and a half times in the wall-normal direction in order to avoid any influence of the box's limitation on the TBL (this height was estimated based on several tests followed by TBL extrapolation).

The extent of the domain in the normal direction requires an extrapolation of the inlet velocity boundary conditions extracted from the precursor DNS. Firstly, a cubic interpolation in the wall-normal direction of the three velocity components is performed up to the edge of the boundary layer to adapt the inlet velocity with the new wall-normal grid, as the number of points and the stretching profile were modified. Other procedures were performed to adapt the velocity outside the boundary layer as new boundary conditions have been applied.

Extrapolation in wall-normal direction

In the free-stream region, new velocities are generated as a continuous and smooth extension of the velocities at the boundary layer thickness with the constraint to be compatible with the boundary conditions applied to the far-field. So, the interpolation of each velocity component is performed independently for each time

step.

The zero spanwise vorticity condition at the top of the inlet is imposed by using $\partial_y U|_\infty = \partial_x V|_\infty$, where the right side is prescribed to apply a given adverse pressure gradient. So, a linear interpolation of the wall-normal derivative of the streamwise velocity was performed in the free-stream region between $\partial_y U|_\infty$ and $\partial_y U|_\delta$ (computed from the streamwise velocity profile at the edge of the boundary layer). Then, the profiles of $\partial_y U$ are integrated in order to ensure the continuity of the streamwise velocity profile and its derivative along the wall-normal direction.

Concerning the wall-normal velocity, a potential flow profile based on (3.3) was added to the interpolated velocity along with the domain's height in order to obtain the aforementioned far-field boundary condition at the top of the domain. Also, the wall-normal velocity is small in the boundary layer region, this procedure ensures the continuity and the smoothness of the final wall-normal velocity profile.

When no additional treatment is applied to the spanwise inlet velocity, a linear interpolation was performed starting from its very small values at the edge of the turbulent part to reach exactly zero at the top of the domain.

This careful interpolation of the 3 velocity components happened to be useful in order to avoid any discontinuities which could affect all the solutions downstream at the edge of the boundary layer.

Periodization in spanwise direction

In order to keep the conformity between the dimensions of the simulation box and to account for the growth of the boundary layer thickness, the simulation domain in the spanwise direction was extended by a factor 4 (as showing in Fig. 3.2) with respect to the precursor DNS of ZPG TBL. This factor 4 was estimated such as the spanwise size of the simulation is at least twice the maximum boundary layer thickness at the outlet. Because of the increase in domain size, the inlet planes were also duplicated. As the original inlet conditions were extracted from a simulation using spanwise periodicity, the extension of the inlet by a factor of 4 is straightforward.

However, to avoid the exact repetition in the results because of duplication of inlet planes, a spatial-temporal noise of small amplitude was added to the inlet velocity components;

$$G(y, z, t) = u_{rms}(y) g(z, t), \tag{3.7}$$

where u_{rms} is the root-mean-square of the three velocity fluctuations. The function noise $g(z, t)$ was chosen to be similar to the numerical forcing used by Schlatter and

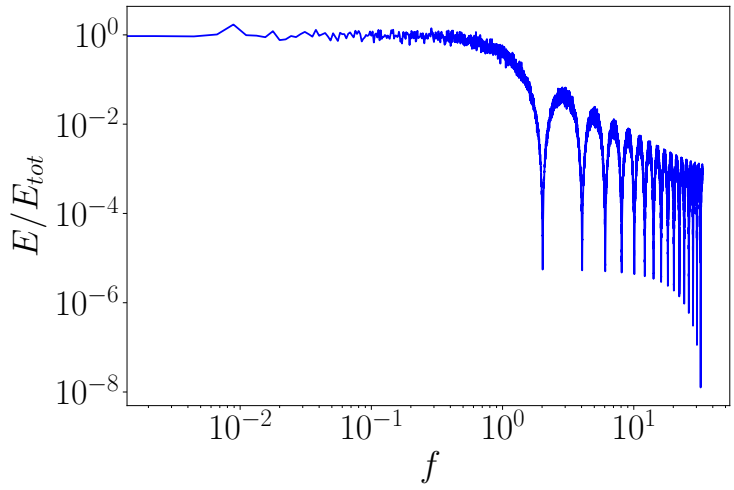

Fig. 3.4. Temporal power spectrum normalized by the total energy of the random noise super-imposed on the periodized inlet BC.

Örlü [126] and it is defined as

$$g(z,t) = A_f \left[(1 - b(t))h^i(z) + b(t)h^{i+1}(z) \right], \tag{3.8}$$

A_f is a normalization amplitude chosen to keep the noise less than 1% of the corresponding velocity fluctuation. This amplitude was chosen such that the solution forgot the periodization procedure after the first half of the simulation domain. The time evolution is defined with $b(t) = 3p^2 - 2p^3$, $p = t/t_s - i$, where i is the integer part of t/t_s.

The spanwise function $h^i(z)$ is defined as the following Fourier series

$$h^i(z) = \frac{1}{\sqrt{N_f}} \sum_{j=1}^{N_f} \alpha_j \cos\left(\frac{2\pi j z}{L_z} + \phi_j \right), \tag{3.9}$$

where N_f is the selected number of modes, α_j is a random amplitude, and ϕ_j is a random phase shift.

The temporal and spanwise cutoff scale of the signal are fixed at $t_s = 3.7\delta/U_\infty$ and $z_s = 0.6\delta$ respectively, where δ is the boundary layer thickness at the inlet and the numbers of modes $N_f = L_z/z_s = 14$ modes. In Fig. 3.4, we show the resulting temporal spectrum; the spectral energy remains stable until a temporal cutoff is reached, and then a steep decrease of the energy towards zero, as a consequence of the third-order polynomial function in g.

Interpolation in time

The decrease of wall friction in the APG case as well as the free-stream velocity allows us to use a larger time step than the one used in the ZPG case (0.015 instead of 0.008). As a consequence, a linear interpolation in time (using "interp1d" from scipy library in python3) was made for the extrapolated inlet planes. The full procedure produces a 2D time-resolved $u(y, z, t)$ inlet boundary conditions fully adapted to the new simulation domain and to the boundary conditions.

3.2.1.3 Outlet conditions

Since the pressure is calculated based on the velocity, a temporal fluctuation was observed in the pressure. These oscillations of the pressure can be due to the turbulent velocity field at the outlet. In order to solve this problem, a fringe region has been applied on the last 3% of the computational domain in order to ensure the laminarity of the outgoing flow. This technique firstly proposed by Nordström et al. [109] consists in the addition of a localized forcing term F in the right-hand side of the Navier–Stokes Equation (2.6) with

$$F = \lambda(x)(\tilde{U} - U) \tag{3.10}$$

where $\tilde{U}$ is a target velocity field and $\lambda(x)$ a modulation function allowing a local activation of the forcing in the region where λ is not zero. Here, the corresponding fringe region is defined using $\lambda(x) = \frac{1}{2}(1+tanh(x))$ as used by Dairay et al. [28]. The effects of this condition are only local and do not affect the solution apart from the region where the forcing is applied. This method was able to improve significantly the stability of the pressure signal.

3.2.2 Spatial and temporal discretization

As already explained in the description of the inlet condition, the spanwise size was selected in order to be at least twice the boundary layer thickness at the outlet of the domain. One of the objectives of the present simulation is to investigate the large-scale structures of streamwise velocity. These structures have been found to extend up to one boundary layer thickness in the spanwise direction and more than one order magnitude more in the streamwise direction. A domain of size at least 2.5δ in the region of interest far enough from the outlet should be enough to not constrain too much the largest streamwise structures. The streamwise size of the simulation domain was selected to reach the maximum Reynolds number accessible with our computing resources. With these constraints, a computational domain of

Table 3.2. Parameters of the TBL are normalized by the quantities (δ_{max}, u_τ) at the outlet. N_x, N_y, and N_z are the number of grid points in the streamwise, wall-normal and spanwise direction respectively. In addition, L_x, L_y, and L_z are the dimensions of the domain. Indeed, Δy_δ^+ is the maximum grid spacing at the edge of boundary layer.

Re_θ	$N_x \times N_y \times N_z$	$(L_x, L_y, L_z)/\delta_{max}$	$\Delta x^+, \Delta y_{wall}^+, \Delta y_\delta^+, \Delta z^+$
$2250 - 8000$	$6401 \times 1025 \times 1280$	$23.2,\ 2.9,\ 2.3$	$5.1,\ 1.0,\ 4.7,\ 2.4$

$L_x = 800\delta_0$, $L_y = 100\delta_0$ and $L_z = 80\delta_0$ was selected. For a fully resolved DNS, the spatial and temporal resolutions must be estimated very precisely to obtain correct results using the minimum computing resources. The spatial resolution must be adapted to be of the order of the Kolmogorov scale on the full simulation domain, especially in the region of interest.

When the friction velocity couldn't be estimated a priori, several test simulations were performed to estimate the decrease of the friction velocity along with the streamwise direction. This is done in order to choose the best spatial resolution on the full domain. The homogeneous spatial resolution in streamwise and spanwise directions normalized by the wall-units along with the computational domain are presented in Fig. 3.5a, where the Δx^+ is around 5 in the targeted region after the transition from ZPG to APG near the inlet, and $\Delta z^+ \sim 2.5$. The grid spacing agrees with those used in the literature. For instance, Jiménez et al. [60] used a spatial resolution of 6.1^+ and 4.1^+ in the streamwise and spanwise directions respectively in his DNS of zero pressure gradient TBL.

The main parameters of our simulation are summarized in Table 3.2: The number of grid points in the three directions, the dimensions of the simulation box which is normalized by the largest boundary layer thickness (achieved at the outlet), and the spatial resolutions (in wall-units) evaluated at the same position.

As the aim was to generate a database that could be used to study the outer region of the boundary layer and possibly the turbulent/non-turbulent interface, the stretching in the normal direction was adapted accordingly. Wall-normal resolution for DNS of TBL is commonly used to be $\leq 1^+$ near the wall. For example, Maciel et al. [88] used a wall-normal resolution which varies from $\Delta y^+ = 0.32$ at the wall to 10.2 at the edge of the boundary layer. Also, Jiménez et al. [60] used $\Delta y^+ = 0.3$ at the wall for DNS of ZPG TBL.

The method proposed by Laizet and Lamballais [71] and implemented in INCOMPACT3D to stretch the mesh in one direction is based on an analytical stretching function compatible with the solution of the Poisson equation in spectral space, as well as in the physical space. In the case of TBL, the stretching is applied in the wall-normal direction. Moreover, as the stretching is controlled by a single param-

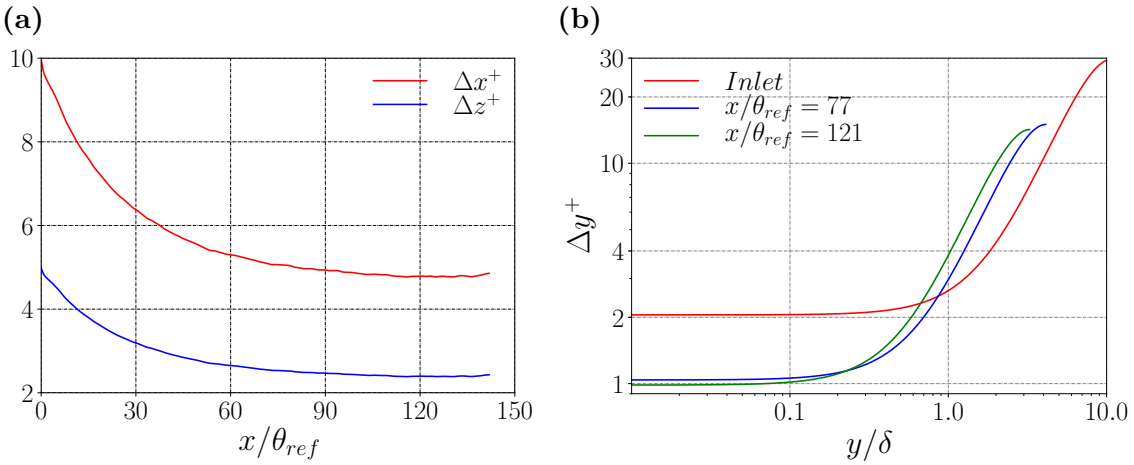

Fig. 3.5. (a) Variation of streamwise and spanwise spatial resolution as a function of the streamwise position. (b) Variation of the spatial resolution in the wall-normal direction as a function of the wall-normal distance scaled by the local boundary layer thickness. The red line represents the resolution at the inlet, the blue one in the middle of the domain, and the green one at the reference streamwise position.

eter, a compromise was selected in order to correctly resolve the near-wall region ($y^+ = 1$) in the region of interest. Fig. 3.5b illustrates the wall-normal resolution that is used in the present DNS at three streamwise positions (the inlet, the center of domain, and the reference streamwise position). The grid spacing is around 1^+ at the wall in the second half of the domain (in the region of interest), and it does not exceed 4^+ at the edge of the boundary layer. Hence, this allows us to focus on the turbulent/non-turbulent interface in future work.

Due to a fine spatial resolution in the three directions, the simulation can be considered as well resolved in the full domain. Additionally, it is highly resolved on the downstream part of the domain and on the full boundary layer thickness. This allows us to perform detailed and accurate statistics of both large scales and small dissipative scales.

In order to validate the compatibility of the spatial resolution with the dissipative scales, a comparison with the Kolmogorov scale was performed. The Kolmogorov length scale is defined as $\eta = (\nu^3/\epsilon)^{1/4}$, where ϵ is the dissipation rate of the kinetic energy and ν is the kinematic viscosity. Fig. 3.6 shows different ways to compare the spatial resolution with the Kolmogorov scale along the boundary layer. The comparison was performed at the reference streamwise position such that $Re_\theta = 7240$. It is noticed that the maximum spatial resolution in the three directions represents $\sim 5\eta$ near the walls to reach $\sim 2.5\eta$ in the outer region. However, it should be mentioned, that, in the very near-wall region, the most relevant comparison is

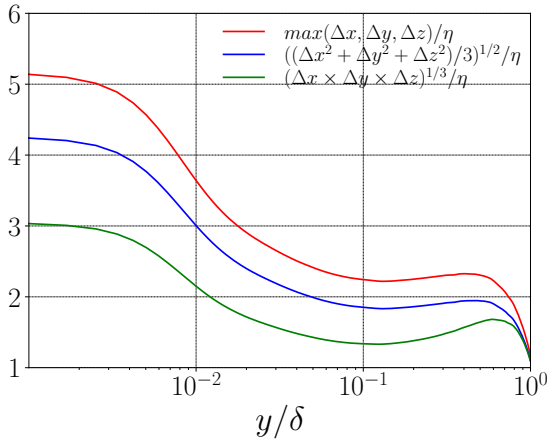

Fig. 3.6. Comparison of the grid spatial resolution with the Kolmogorov scale along the wall-normal direction. η and δ are evaluated at the reference streamwise position. As the mesh is stretched in the wall-normal direction, the comparison is evaluated using three definitions of the characteristic grid spacing.

with respect to the wall-normal grid spacing which is 5 times smaller than the streamwise one. Overall, the spatial resolution is adapted on the full simulation domain and allows us to study statistics down to the dissipative scales.

In order to choose a time step adapted with our simulation taking into account the minimum computation cost, preliminary tests have shown that the maximum CFL allowed to stabilize the simulation should be of the order of 0.15. To be conservative, a constant time step $\Delta t = 0.015$ (corresponding to a maximum CFL equal to 0.137) was used for the full simulation. Computed in terms of local wall-units, the time step Δt^+ decreases from 0.04 at the inlet to achieve 0.01 at the outlet due to the decrease of the friction velocity.

3.3 Description of the databases

The growth of the turbulent boundary layer along the streamwise direction is visualized in Fig. 3.7a by a snapshot of the instantaneous spanwise vorticity in a streamwise - wall-normal plane on the full simulation domain. A zoomed region of the vorticity in the spanwise direction shows that the spatial resolution is well-adapted down to the small scales corresponding to the vortex filaments. A snapshot of the streamwise velocity fluctuations is also presented in Fig. 3.7b.

The DNS was performed on a grid with more than 8 billion nodes using 2048 cores. The simulation was effectuated on the Occigen[4] supercomputer of CINES (Intel Xeon E5-2690V3@2.6 GHz) and on the supercomputer Jean-Zay[5] of IDRIS

[4] `https://www.cines.fr/calcul/materiels/occigen/`
[5] `http://www.idris.fr/jean-zay/`

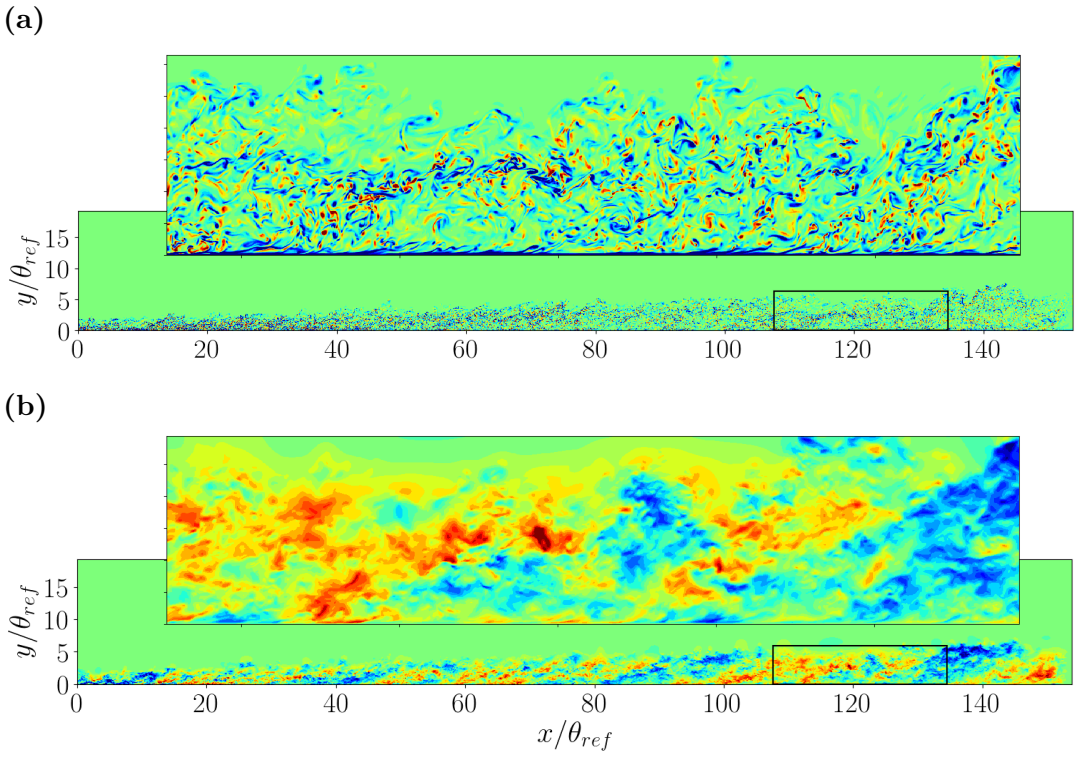

Fig. 3.7. Snapshot in a streamwise wall-normal plane on the full simulation domain of (a) the spanwise vorticity and (b) the streamwise velocity fluctuations. The coordinates are normalized with the momentum thickness at the reference streamwise position θ_{ref} such that $Re_\theta = 7240$.

(Intel Cascade Lake 6248 2.5 GHz). A total cost of $\sim$ 4 million CPU hours from the GENCI allocation has been used to perform this simulation.

A large database of more than 100 TB was collected from this simulation after the transient part. This database includes three types of raw data:

The first one is composed of time-resolved wall-normal spanwise planes of the three components velocity and the pressure field collected at the three streamwise positions are represented in Fig. 3.8 by the black vertical lines (corresponding to $Re_\theta = 6038$, 7237 and 7795). They were collected every 5 time-steps ($\Delta t^+ \simeq 0.06$) that correspond to a half grid spacing displacement in the free-stream region. These datasets allow us to perform a time-resolved analysis. For example, the time correlation function was calculated using the middle plane datasets (see section 4.3).

The second dataset is composed of 211 three-dimensional fields of the full simulation domain for the same previous quantities with a time spacing $\Delta t^+ = 7.8$. This dataset is useful to obtain statistics along the streamwise direction and the evolution of various quantities downstream.

Furthermore, there are 1315 fields of a 3D restricted domain in the downstream region of the flow ($Re_\theta = 6818 - 7582$), for the velocity components, their temporal

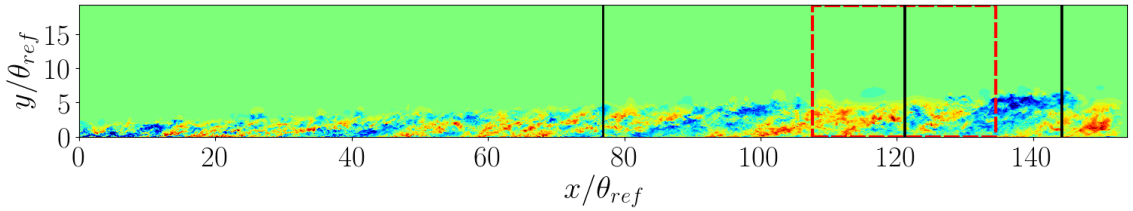

Fig. 3.8. Visualization of the streamwise velocity fluctuation in the full simulation domain. The three black lines represent the streamwise positions of the 2D time-resolved planes and the red dashed box corresponding to the borders of the 3D small fields.

derivative, as well as the pressure. These fields are well-resolved (collected every 1.2 wall-unit time) which allow us to accurately track and analyze the coherent structures over time in this region. The borders of this domain are shown in Fig. 3.8 using the red dashed box. The position of the middle planes ($Re_\theta = 7240$) coincides with the center of these fields.

This large database was collected over 45 large-scale characteristic times $T = \delta_{max}/U_e$ after the transient part, with δ and U_e evaluated at the outlet position.

The main parameters of the 2D time-resolved planes are summarized in Table 3.3. The streamwise positions normalized by the momentum thickness at the reference streamwise position and both Reynolds numbers for the three planes are given. The evolution of the boundary layer thickness between the three positions is also presented, as well as the local characteristic time over which the datasets were collected.

Table 3.3. Parameters of the wall-normal-spanwise time-resolved planes. The boundary layer thickness δ and the edge velocity U_e are measured at the local streamwise location x and normalized by θ_{ref}. T is the total time of the datasets.

x/θ_{ref}	Re_θ	Re_τ	δ/δ^I	TU_e/δ
76.9	6038	986	2.56	59.47
121.1	7240	1182	3.24	44.38
144.2	7795	1348	3.61	39.23

As mentioned in the previous chapter in section 2.2.4, the Q-criterion was commonly used to identify the vortical or swirling motions beside other methods and criteria. For incompressible flows in three-dimensional space, we have $Q = -\frac{1}{2}tr\left((\nabla\mathbf{u})^2\right)$, where $tr(.)$ is the trace of the relevant tensor and $\nabla\mathbf{u}$ is the velocity gradient tensor.

In order to give a qualitative indication of the evolution and complexity of the vortical coherent structures, Fig. 3.9 shows an instantaneous iso-surface of the Q criterion for a 3D domain downstream ($6818 < Re_\theta < 7582$). The threshold used was adapted to focus on the high values of Q that represent eddies. Further analysis of

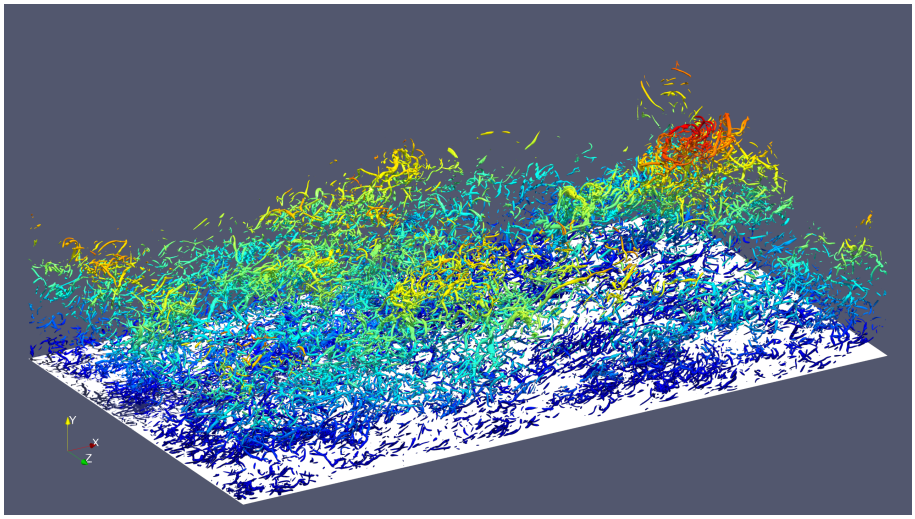

Fig. 3.9. Instantaneous iso-surface of the Q-criterion in the domain such that $6818 < Re_\theta < 7582$. The direction that is directed inwards into the page has been used as the streamwise direction, the wall-normal direction is perpendicular to the white plan. The color table is proportional to the distance from the bottom wall.

the temporal evolution of the vortices shows that the 3D database used to calculate the Q criterion is well resolved in time because of the continuous motion of the vortices, in addition to the compatible spatial resolution that allows us to identify the vortex filaments up to the boundary layer edge.

3.4 Boundary layer statistics

It is noticed that in the presence of an adverse pressure gradient the streamwise velocity is no longer constant in the free-stream non-turbulent region. Additionally, it will not be possible to define the edge velocity U_e based on the maximum velocity, particularly in the presence of suction velocity and zero spanwise vorticity conditions that are applied to the top of the domain. A reference velocity scale, based on the mean spanwise vorticity, is firstly proposed in Lighthill [83]. Kitsios et al. [67] used this velocity scale as an outer velocity instead of the classical free-stream velocity. The new characteristic velocity is given by

$$U_e(x) = U_\Omega(x, y_\Omega), \text{ where} \tag{3.11}$$

$$U_\Omega(x, y) = -\int_0^y \langle \Omega_z \rangle (x, \tilde{y}) d\tilde{y} \tag{3.12}$$

where $\langle \Omega_z \rangle$ is the mean spanwise vorticity, and y_Ω is the wall-normal position at which $\langle \Omega_z \rangle$ is 0.2% of $\langle \Omega_z \rangle|_{y=0}$.

When a boundary layer is subjected to an adverse pressure gradient, i.e., the pressure increases along the streamwise direction; hence, the free-stream velocity must be decelerated downstream based on Bernoulli's equation (2.26). Fig. 3.10a shows the decrease in the edge velocity U_e up to 70% of its initial value at the inlet position. U_e was calculated based on the mean spanwise vorticity as explained in (3.11).

The growth of boundary layer thickness along the streamwise direction is also presented in Fig. 3.10b. Here, δ is calculated using the traditional method where it is the wall-normal position at which the mean streamwise velocity represents 99% of the edge velocity U_e. As noticed in the figure, the outlet TBL thickness (δ_{max}) reaches $\sim$ 3.5 times of the inlet one where the extent of the simulation domain downstream represents $23.2\delta_{max}$ evaluated at the outlet position.

The two length scales which describe the boundary layer, the displacement and momentum thickness, that are detailed early in section 2.1.3 need to be adapted with the presence of adverse pressure gradient as mentioned in [67]. Since the equations (2.12) and (2.13) are no longer efficient in the case of a decelerating boundary layer, Spalart and Watmuff [144] proposed new formula for both thicknesses based on the mean spanwise vorticity

$$\delta_1 = \frac{-1}{U_e} \int_0^{y_\Omega} y \langle \Omega_z \rangle dy \tag{3.13}$$

$$\theta = \frac{-2}{U_e^2} \int_0^{y_\Omega} y U_\Omega \langle \Omega_z \rangle dy - \delta_1 \tag{3.14}$$

The above definitions have been used to evaluate the corresponding length scales in our simulation. Moreover, to analyze the growth rate of both thicknesses in comparison to the boundary layer thickness, the three quantities are plotted in Fig. 3.10b normalized by their values at the inlet position. It is clearly noticed that the growth rate of δ_1 and θ is greater than this of δ which seems to follow a linear evolution. To be more specific, a comparison of these thicknesses at two streamwise positions were performed, where the first one is the inlet position which represents a ZPG case and the second one is chosen downstream at $x = 120\theta_{ref}$ (corresponding to $Re_\theta = 7240$) inside the APG region in order to focus on the effects of the pressure gradient. It is noticed that δ_1 increases from 0.18δ in ZPG TBL to achieve 0.28δ in APG domain. And the momentum thickness θ increases from 0.12 to 0.16δ. The increase of both displacement and momentum thicknesses in comparison to δ between ZPG and APG cases can be explained as the mean velocity profile in APG TBL is steeper than ZPG case, where both δ_1 and θ are based on the mean velocity deficit.

The shape factor $H = \frac{\delta_1}{\theta}$ is also presented in Fig. 3.10c. The value of H increases

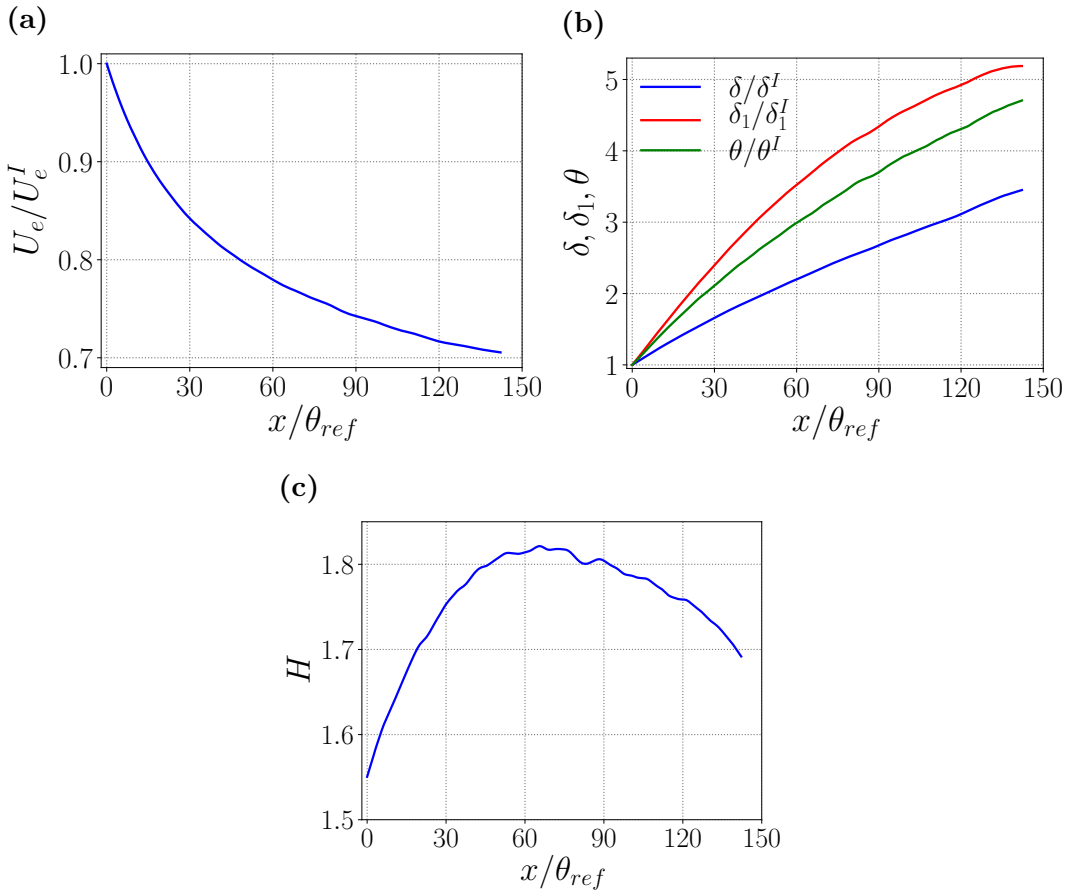

Fig. 3.10. (a) Free-stream velocity U_e; (b) boundary layer thickness δ, displacement thickness δ_1, and momentum thickness θ are plotted normalized by the corresponding inlet quantities indicated by the superscript $(.)^I$; (c) shape factor $H = \delta_1/\theta$. All quantities are plotted as function of the streamwise position normalized by θ_{ref}.

downstream to reach a maximum of 1.82 at $Re_\theta \simeq 5500$ followed by a slow decrease downstream. The range of variation of the shape factor $H \sim (1.7 - 1.8)$ is usually associated in the literature to a moderate adverse pressure gradient.

Even the shape factor gives an idea of the pressure gradient but it does not represent directly the pressure gradient. In order to focus on the evolution of adverse pressure gradient downstream, the pressure gradient parameter proposed by Clauser [23] as $\beta = \delta_1 \partial_x P_e / \tau_w$ was presented in Fig. 3.11a, where $\partial_x P_e$ is evaluated at the boundary layer edge. The parameter β was commonly used in the experimental and numerical investigations of turbulent flows subjected to a pressure gradient. The intensity of APG in the TBL examples summarized in Table 3.1 are evaluated using the parameter β, where $\beta \simeq 1$ corresponds to mild APG and $\beta \sim 20 - \infty$ corresponds to strong APG and separated flows. In the current TBL APG, the value of β presents an increase from 2.2 to reach its maximum at $Re_\theta \sim 5000$ that corresponds to 20 boundary layer thickness (obtained by integration of the local boundary layer

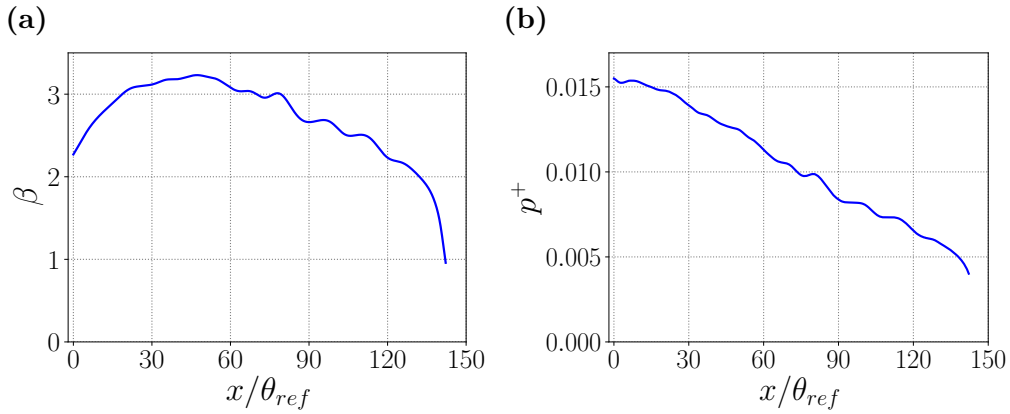

Fig. 3.11. (a) Non-dimensional pressure gradient parameter $\beta = \delta_1 \partial_x P_e / \tau_w$, where $\partial_x P_e$ is the pressure gradient at the edge of boundary layer; (b) streamwise pressure gradient scaled by the inner quantities $p^+ = \frac{\nu}{\rho u_\tau^3} \frac{dP_e}{dx}$.

thickness $\delta(x)$) then it slowly decreases toward the outlet. The steep decreasing close to the end of the domain is due to the outlet conditions. This non-constant evolution of pressure gradient parameter β leads that the current APG TBL is out of equilibrium.

Another indicator of the pressure gradient was also presented in Fig. 3.11b which is the streamwise pressure gradient scaled by the inner quantities $p^+ = \frac{\nu}{\rho u_\tau^3} \frac{dP_e}{dx}$. p^+ was used in the modified formula of the wall-law in presence of APG (see eq. (2.35)). The value of p^+ decreases when moving downstream from ~ 0.015 down to 0.005 close to the outlet. The present values of p^+ are not sufficiently strong to affect strongly the behavior of boundary layer as a moderate pressure gradient has been imposed.

In order to study the friction and the viscous forces, the friction velocity (used in the wall-unit scaling) and the friction coefficient $C_f = 2\left(u_\tau / U_e\right)^2$ are evaluated at the wall along the streamwise direction. As expected, both quantities decrease downstream due to the effect of adverse pressure gradient which leads to a deficit of momentum in the near-wall region with respect to the ZPG case at the same global Reynolds number. Their evolution is presented in Fig. 3.12a and 3.12b as function of the streamwise position. The friction velocity u_τ reduces to almost 50% of its value at the inlet. It is also noticed that in the second half of the domain the friction remains constant at ~ 0.019. Concerning the friction coefficient, C_f has a steep decreasing close to the inlet before stabilizing at 1.5×10^{-3}. For comparison a friction coefficient of $C_f \sim 2.5 \times 10^{-3}$ was obtained by Kitsios et al. [66] in their DNS of TBL subjected to a mild APG ($\beta = 1$) and the value of C_f reduced to 0.5×10^{-3} in presence of strong APG ($\beta = 39$) [67]. The small increase noticed in the outlet region is due to the effects of outlet conditions.

The Reynolds number was presented using two different length and velocity scales. Firstly, the Reynolds number based on momentum thickness Re_θ defined in (2.18) is shown in Fig. 3.12c. Re_θ increases from 2250 at the zero pressure gradient inlet position up to almost 8000 at the outlet position. A higher Reynolds number ($Re_\theta = 13800$) was achieved in the DNS of APG TBL of Kitsios et al. [67], but this was with a much stronger pressure gradient ($\beta = 39$) for which the increase of the momentum thickness is much faster. On the other hand, the available DNSs of TBL subjected to a moderate APG are still limited in terms of Reynolds number, e.g., $Re_\theta = 2180$ is obtained in the DNS of Lee [76] ($\beta = 2.2$) and the DNS of [169] ($\beta = 1.43$) has a maximum of $Re_\theta = 5700$. The current DNS of APG TBL reached the biggest Reynolds number obtained with this range of moderate adverse pressure gradient, which contribute to focus on the effects of moderate APG at higher Reynolds than previously obtained. The statistics will be compared in the next chapter with the experiments of Srinath et al. [145] over a ramp ($\beta = 2 - 3.7$) at Reynolds number $Re_\theta = 13800$ and 23400. The growth of the friction Reynolds number Re_τ from 750 up to 1350 along the streamwise direction is also presented in Fig. 3.12d. Re_τ is evaluated using the friction velocity and δ as mentioned in (2.19).

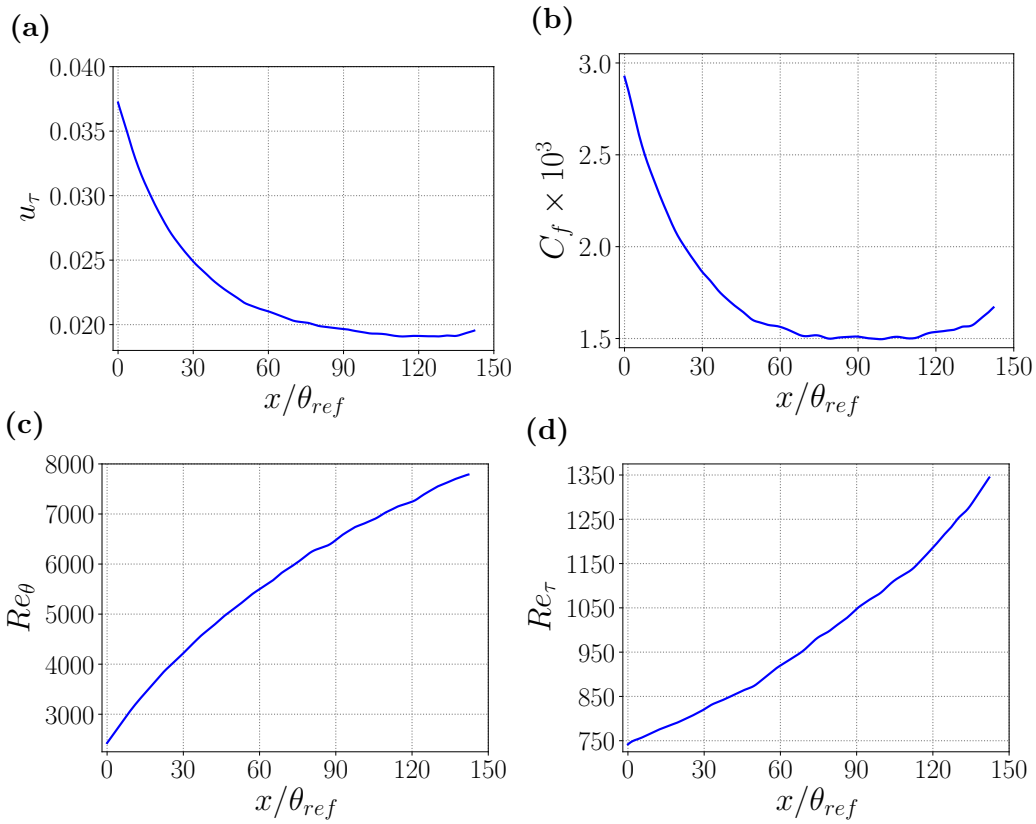

Fig. 3.12. (a) Friction velocity u_τ; (b) friction coefficient $C_f = 2\,(u_\tau/U_e)^2$; (c) Reynolds number based on the momentum thickness $Re_\theta = U_e\theta/\nu$; (d) Reynolds number based on the friction velocity $Re_\tau = u_\tau\delta/\nu$.

Chapter 4

Statistical analysis

This chapter is devoted to the statistics of the current turbulent APG boundary layer. The mean streamwise velocity and the Reynolds stresses are presented in comparison with a ZPG TBL. A deep investigation of the outer peak of Reynolds stresses was also performed as well as an analysis of the energy balance. Different types of velocity scaling have been tested, especially in the outer region. Finally, the spanwise energy spectra of the streamwise velocity fluctuations are presented.

4.1 Statistics of turbulent boundary layer

4.1.1 Mean velocity profiles

The mean streamwise velocity and the Reynolds stresses profiles are plotted in Fig. 4.1 at several streamwise positions including at the inlet (red line) which corresponds to a ZPG case. The wall-unit scaling already defined in chapter 2 was used to normalize both lengths and velocities. The APG profiles are compared with ZPG ones at similar Reynolds numbers (both Re_θ and Re_τ) from the DNS of Sillero et al. [131, 132](dash-dotted lines). Fig. 4.1a shows that the mean velocity profiles collapse close to the wall and follow the $U^+ = y^+$ equation as p^+ is small ($0.005 < p^+ < 0.015$) and then the theoretical profile derived in eq. (2.35) taking into account the pressure gradient is impossible to distinguish from $U^+ = y^+$ in the viscous region. The comparison with ZPG clearly shows the effect of adverse pressure gradient on the logarithmic layer. The profile at $Re_\theta = 3000$ which is very close to the inlet and experiences a fast transition between ZPG inlet condition and APG exhibits a much steeper log layer. However, moving downstream at $Re_\theta > 4500$, which is close to the maximum of β, the log layer recovers a similar slope as for ZPG. As already observed for APG TBL, the departure from log-layer to the wake region, also identified as square root region by Nickels [106], is stronger with APG.

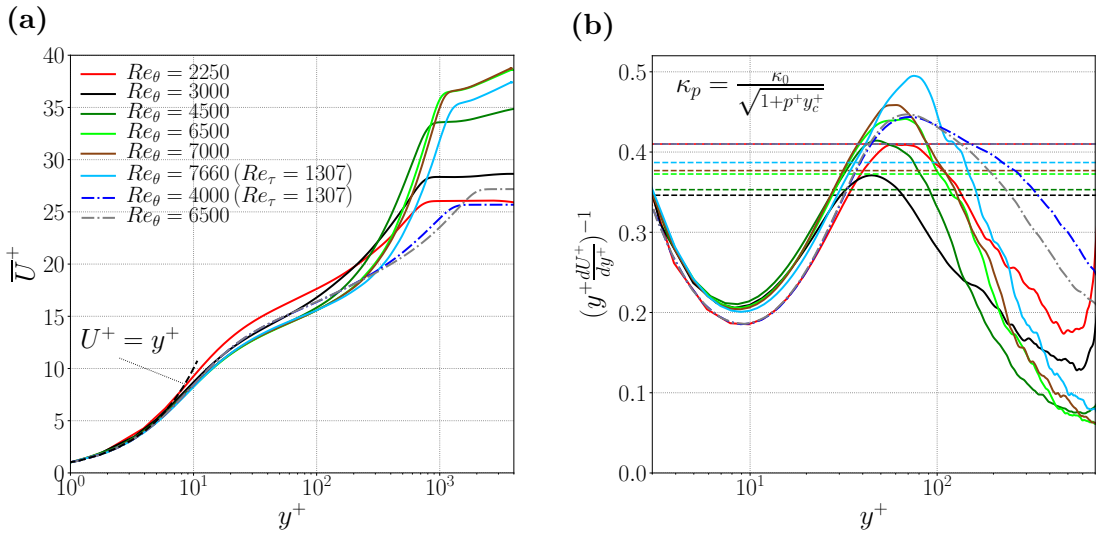

Fig. 4.1. (a) Mean velocity profiles of the current APG study (solid lines) in comparison with ZPG profiles from Sillero et al. [131, 132] (dash-dotted lines). (b) Diagnostic plot at the same streamwise locations as (a). The dashed horizontal lines correspond to κ_p computed with eq. (2.37).

To investigate in more detail the log-law scaling in the current APG TBL, a diagnostic plot was performed at the same locations used earlier (see Fig. 4.1b). The value of the modified log-law constant κ_p defined in (2.37) was also expressed in the same figure using the dashed horizontal lines. To calculate κ_p, the most commonly used value of 0.41 is used for κ_0 and the critical wall-distance was set to $y_c^+ = 12$ as mentioned in [106]. The normalized pressure gradient p^+ has been evaluated at the corresponding local positions. It is clearly shown that the values of κ_p predicted by the model (2.37) do not match with the results. This mismatch is clearly not linked to the choice of κ_0. Furthermore, a logarithmic behavior should appear as a plateau in $(y^+ \frac{dU^+}{dy^+})^{-1}$ profile, but as shown, the logarithmic range is not well defined as no plateau is present even at the highest Reynolds. All the profiles exhibit a maximum which moves toward the wall for the lowest Reynolds number ($Re_\theta = 3000$) under the effect of APG and then moves away from the wall like the square root of Re_θ when moving downstream. This peak does not seem to flatten for any Reynolds numbers.

4.1.2 Reynolds stresses

In Fig. 4.2a, we presented the streamwise velocity fluctuations at the same streamwise positions as the mean velocity profiles. The position of the near-wall peak is not affected by the APG and is located at $y^+ \simeq 12$ [52]. The intensity of the near-wall peak seems slightly increased as compared to the ZPG at equivalent Reynolds

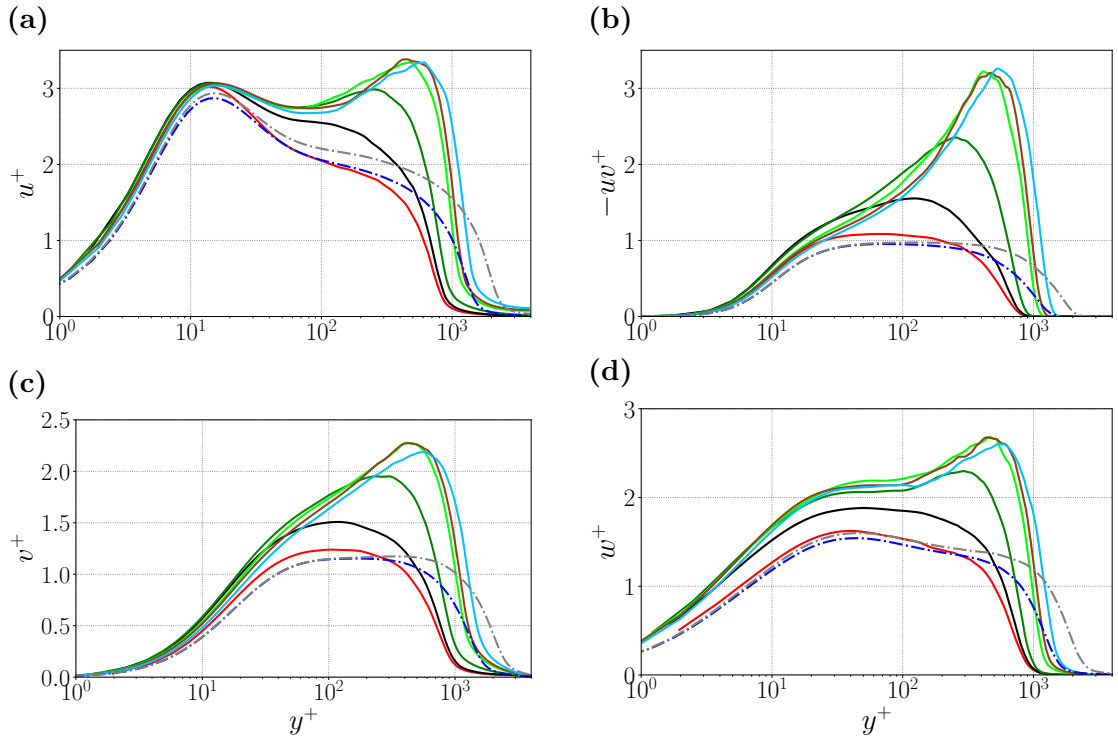

Fig. 4.2. Reynolds stresses profiles of the current APG study (solid lines) in comparison with ZPG profiles from Sillero et al. [131, 132] (dash-dotted lines). The profiles corresponding to the same Reynolds numbers as Fig. 4.1.

number. However, the main effect of APG is to generate a second peak in the outer layer even at the moderate Reynolds number, whereas in canonical ZPG flows, an extremely high Reynolds number is required to produce an outer peak which is much closer to a plateau even at Reynolds number up to $Re_\tau = 70000$ as it was shown by Vallikivi et al. [155] or at even larger Reynolds number available from atmospheric boundary layer flows [54]. In the current study, the outer peak increases by moving downstream up to $Re_\theta \simeq 6500$ before stabilizing despite the increase of Reynolds number. The intensity of the outer peak appears to be higher than that of the inner peak when Re_θ exceeds 5000. It is also noticed that the wall-normal position of the outer peak moves away from the wall when increasing the Reynolds number. Furthermore, if this strong outer peak is associated with an enhancement of attached eddy structures, it is expected that these structures have an impact down to the buffer region and participate in the increase of the inner peak as it does for extreme Reynolds numbers ZPG TBL. It will be shown that the outer peak observed in APG cases is related to an excess in the production rate of turbulent kinetic energy which exceeds the turbulent dissipation rate at the position of the outer peak.

The Reynolds shear stress, the wall-normal and spanwise Reynolds stress are also shown in Fig. 4.2. The evolution of the outer peak is clearly shown in all cases

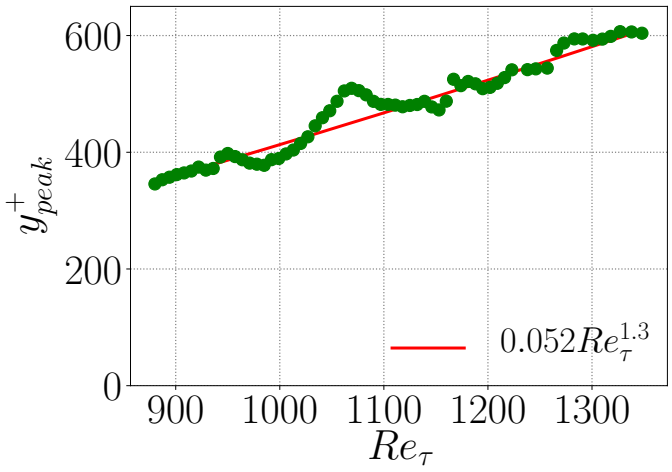

Fig. 4.3. Evolution of outer peak position of the streamwise Reynolds stress normalized by the wall-unit length scale δ_ν as a function of Re_τ.

similar to the streamwise velocity fluctuation and is found at the same wall-normal positions. This observation leads to think that this peak in all Reynolds stresses may be associated with a single dynamics of turbulent structures.

As shown previously, the wall-normal position of outer peak y^+_{peak} grows with increasing of Reynolds number downstream (using the wall-unit scaling). The evolution of this peak position is shown in Fig. 4.3 as a function of Reynolds number Re_τ. The outer peak position is investigated in a quasi-equilibrium region where β is almost stable and far from the ZPG/APG transition region near the inlet, as well as far from the outlet effects (corresponding to $870 < Re_\tau < 1350$). The wall-unit position of this peak increases from 350^+ to 600^+ with a scaling which can be fitted by $0.052\,Re_\tau^{1.3}$. The wavy evolution of the outer peak is due to the insufficient convergence of the current database but this does not affect the main conclusion on the Reynolds stresses statistics. Using wall-unit scaling can not scale the position of the outer peak as this scaling is expected to scale the near-wall region where the viscosity is dominant.

For further study and to simultaneously analyze the outer peak of the different Reynolds stresses, the positions of the outer peak of the streamwise and wall-normal velocity fluctuations as well as the Reynolds shear stress for the current TBL APG are presented in Fig. 4.4 using the outer length scale δ. However, using a constant scale (δ^I or δ_{max}) to normalize the streamwise position is not appropriate in the APG TBL where the boundary layer thickness grows rapidly. For this purpose, we used a local scaling based on δ evaluated at the local streamwise position. The local position x/δ_{loc} is obtained by integrating the inverse of the local boundary layer

thickness in the streamwise direction as follows

$$x/\delta_{loc} = \int_0^x \frac{1}{\delta(x)} dx \tag{4.1}$$

It is clearly noticed that the position of the outer peak for the three Reynolds stresses grows similarly, except for the streamwise velocity fluctuation in the region before $x/\delta_{loc} = 17$, where the inner peak is stronger than the outer one. The position of the outer peak increases downstream for almost 20 local boundary layer thickness before stabilizing at $y_{peak} \simeq 0.45\delta$. In order to compare with the experimental results, an equivalent plot has been established in Fig. 4.4b for the data of Srinath et al. [145] at a much higher Reynolds ($Re_\theta = 23000$) and a different but comparable evolution of β. Although this TBL experiment was performed on a ramp of about 4 meters long, it represents only ~ 23 local boundary layer thickness.

The peak position when scaled with the displacement thickness exhibits a comparable evolution as a function up to 23 local boundary layer thickness (the maximum values for the experiments). As the DNS domain extends further, one can see that the position of the peak seems to converge around $1.5\delta_1$. To estimate this value with a good accuracy would require a much better convergence of the Reynolds stresses profiles. When scaled with the boundary layer thickness, the position of the peak is closer to the wall than for the DNS case in the same range of streamwise position (scaled with δ_{loc}). One can see that the position of the peak which is of the order of 0.25δ still increases linearly at $x/\delta_{loc} = 23$ in the experiments when the same curve starts to flatten in the DNS to converge to a value slightly below 0.5δ at the end of the simulation domain. This difference can be due to the different shapes of the boundary layer but also to the accuracy of the computation of the boundary layer thickness. Srinath et al. [145] have noticed that depending on the definition of δ (95% or 99% of the position of the mean velocity maximum) its value may vary from 25%. Taking the δ_{95} for the estimation of the boundary layer thickness for the experiments would therefore leads to a better comparison of the evolution of the position of the peak with the DNS case.

The same scaling of the outer peak position of the Reynolds stresses normalized by the displacement thickness δ_1 is also presented in Fig. 4.4. The present evolution shows that, in both cases, the peak position increases from 0.5 to $1.3\delta_1$ for $x \simeq 23\delta_{loc}$. However, for the DNS of TBL, the peak position still increases slowly after that position and does not stabilize contrary to what is observed with normalization by the boundary layer thickness. Moreover, δ_1 can also collapse the outer peak position for all Reynolds stresses.

These results are in agreement with those obtained by Kitsios et al. [67], where they found that the outer peak position change from $1.3\delta_1$ for mild APG TBL

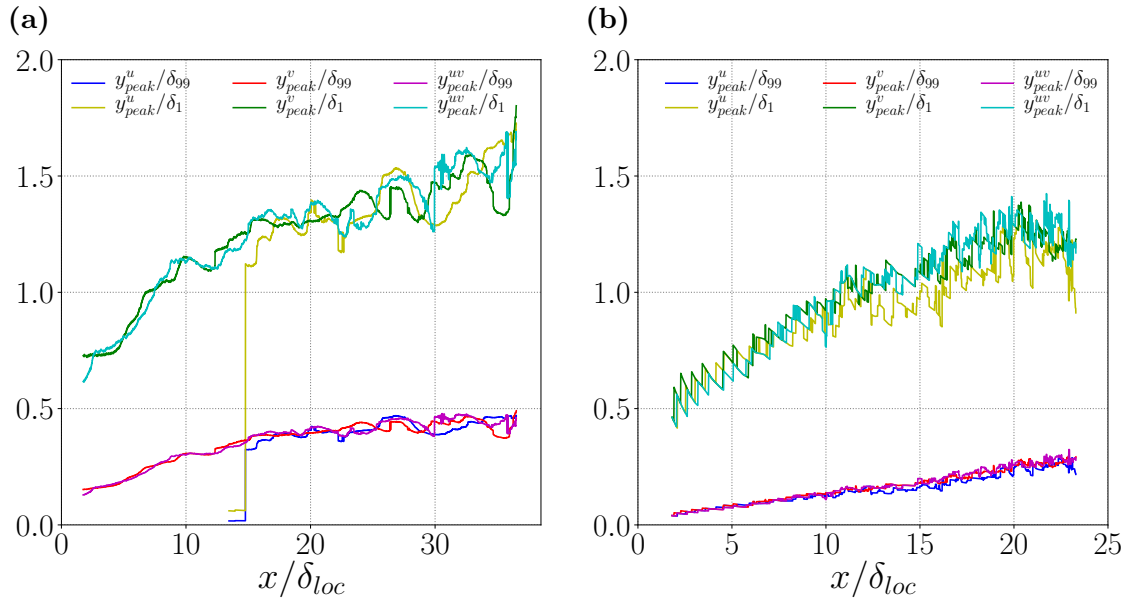

Fig. 4.4. Evolution of the outer peak position of streamwise and wall-normal velocity fluctuations as well as the Reynolds shear stress. The streamwise position is normalized by the local boundary layer thickness computed by eq. (4.1). (a) for the current APG TBL and (b) for the experiment of Srinath et al. [145] at $U_\infty \simeq 9m/s$.

($\beta = 1$) to $y_{peak} = \delta_1$ with strong APG. They have obtained an almost constant peak position for each case as the boundary layer is in equilibrium. However, they have shown that the position of the outer peak is not universal and depends on the intensity of the adverse pressure gradient. They also noticed that this outer peak is located approximately at the same position of an inflection point in the mean streamwise velocity profile.

On the other hand, the intensity of the outer peak of Reynolds stresses is presented in Fig. 4.5 for the current APG TBL as well as for the experiment of Srinath et al. [145] as a function of the streamwise position normalized by the local boundary layer thickness. Wall-unit scaling of the intensity of these peaks in the current DNS (not shown) presents a fast increase downstream up to a maximum at $x \simeq 30\delta_{loc}$ then the intensity decrease due to the increase of friction velocity close to the outlet. However, the intensities shown in Fig. 4.5 are normalized by the outer velocity scale U_e and in both cases all the Reynolds stresses increase downstream almost linearly except the wall-normal quantities which have a steep increase in the inlet region. The streamwise Reynolds stress is multiplied by one half to ensure a simple comparison as its value is much larger than the other quantities. Note that in the DNS, u^2 profile is plotted only in the region where the outer peak dominates the inner one. Comparing with the experiment, one can notice that the Reynolds stress

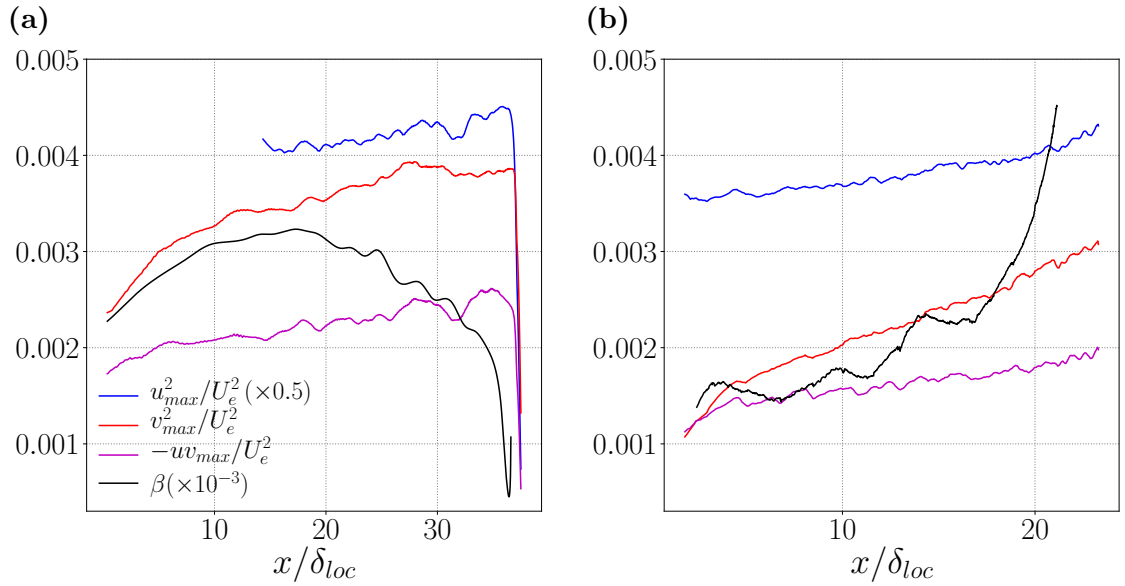

Fig. 4.5. Evolution of the outer peak intensity of streamwise and wall-normal velocity fluctuations as well as the Reynolds shear stress. The peak intensity is normalized by the local freestream velocity and the streamwise position is normalized by the local boundary layer thickness based on eq. (4.1). The streamwise quantities are multiplied by one half to ensure a simple comparison. (a) For the current APG TBL and (b) for the experiment of Srinath et al. [145] at $U_\infty \simeq 9m/s$. Black lines corresponding to the pressure gradient parameter β.

intensities develop similarly in the region of $x < 23\delta_{loc}$ with lower intensity for the experimental profiles, especially for the wall-normal velocity fluctuations which are $\sim 40\%$ less than that of the DNS case. On the other hand, it is not simple to compare both cases even with a comparable magnitude of APG. As shown in Fig. 4.5, the parameter β has a different behavior between both cases. However, it is clearly noticed that despite the drop in β in the DNS case, the Reynolds stress intensity still increases downstream. This may be attributed to the Reynolds number which is still increasing for a time delay between the effect of the pressure gradient and the magnitude of the peak. In this case, as the change of pressure gradient is not sudden it is difficult to distinguish between the two possible effects.

4.1.3 Energy budget

As mentioned in section 4.1.2, the outer peak which appears due to the APG effect on the Reynolds stress profiles can be related to an excess in the production rate of turbulent kinetic energy over the turbulent dissipation rate ϵ. To focus on this purpose, we investigate the dominance of the turbulent production rate P in

comparison with ϵ.

The turbulent production rate and the turbulent dissipation rate are defined by $P = -\langle u_i u_j \rangle \partial_j \langle U_i \rangle$ and $\epsilon = \nu \langle \partial_j u_i \partial_j u_i \rangle$ respectively. In order to investigate the balance of these two quantities, the energy source which represents the difference between P and ϵ is also presented in Fig. 4.6a normalized by the wall-unit. The results from the current APG TBL at $Re_\theta = 6500$ are compared with DNS data of ZPG TBL from Sillero et al. [131, 132] at the same Re_θ (APG TBL corresponding to $Re_\tau = 1100$ and 1990 for ZPG TBL). As expected, the turbulent dissipation rate has its maximum value near the wall due to high viscous effects, then it decreases away from the wall to reach zero near the boundary layer edge similarly in both ZPG and APG cases, whilst, in the outer region of APG TBL, the dissipation rate profile has a plateau before reaching zero at the edge of TBL. Regarding the mean production rate, a peak has been shown near the wall ($y^+ \simeq 10$) in both ZPG and APG TBLs. Its wall-normal position is very close to the inner peak position noticed in the streamwise turbulence intensity (see Fig. 4.2a). The intensity of the inner peak of production as well as the maximum dissipation at the wall normalized by inner variables is slightly larger for the APG case as compared to the ZPG case despite the higher friction Reynolds number of the ZPG TBL. In the outer region, an outer peak appears in the production profile only in the APG case.

Focusing on the energy source, the inner peak of production dominates the dissipation rate and the energy source remains positive up to sightly below the lower bound of the logarithmic region ($y^+ = 30$). Then, in ZPG TBL, a small negative value has been obtained in the log-layer until reaching zero in the outer region. However, in the presence of APG, the energy source profile exhibits an inflection from negative to positive at the upper edge of the logarithmic region to reach a maximum in the middle of the outer layer near 0.5δ. This peak, which represents the dominance of production over dissipation rate, leads to excessive turbulence being produced within this region and at least partly explains the outer peak which appears in the Reynolds stress profiles. Furthermore, Kitsios et al. [67] noticed that a net transfer of the mean streamwise momentum from the turbulent fluctuations to the mean field has occurred in that region.

Further investigation of this outer peak was conducted by comparing the energy source at different streamwise positions. First, a comparison using viscous scaling (not shown) shows that the outer peak of the energy source grows with increasing Reynolds number, in agreement with the results previously found by Cimarelli et al. [21]. They also noticed that the extent of the production dominance region expands as the Reynolds number increases. However, scaling of the energy source using outer quantities such as boundary layer thickness (δ) and freestream velocity (U_e) seems to almost collapse all curves corresponding to $Re_\theta > 5000$ along the

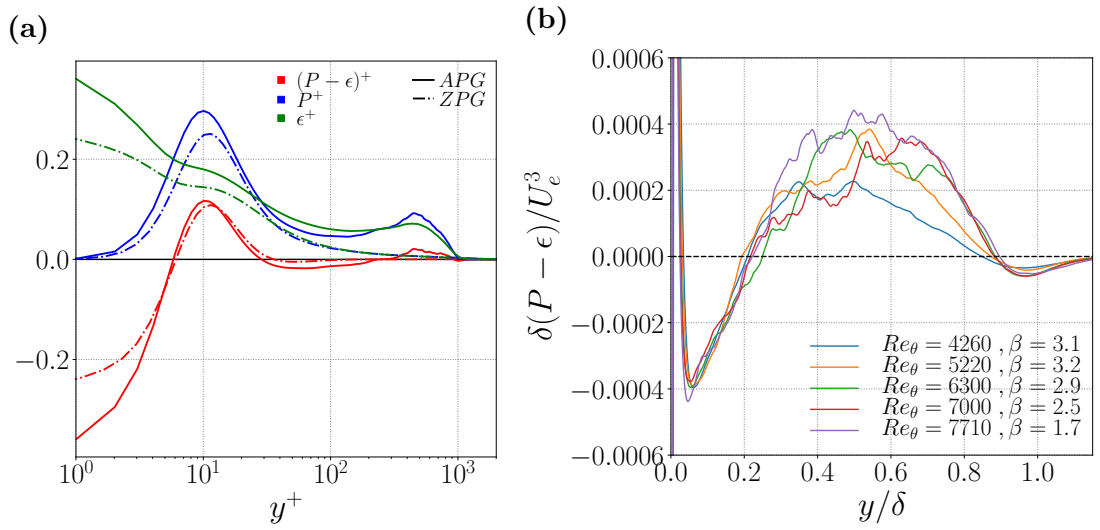

Fig. 4.6. (a) The energy source, production and turbulent dissipation rate of turbulent kinetic energy at $Re_\theta = 6500$. The ZPG data are from the DNS of Sillero et al. [131, 132]. (b) The energy source scaled by the outer quantities δ and U_e collected at several streamwise positions with the corresponding Reynolds number Re_θ and pressure gradient parameter β.

entire outer region (see Fig. 4.6b). The energy source corresponding to $Re_\theta = 4500$ presents a different behavior because at this position, the pressure gradient was not high enough and one can clearly notice that the outer peak of the streamwise velocity fluctuation at this position is slightly smaller than the inner one. Based on this observation, we can see that the outer parameters scale this outer peak much better than viscous scaling, similar to what we have already shown in the scaling of the outer peak of the streamwise velocity fluctuations.

4.2 Velocity scaling

Finding a good scaling of mean and turbulent quantities is an important challenge in the turbulent flow, especially those subjected to an APG where the outer region is more energized than ZPG and an outer peak is found in the Reynolds stresses which affects the statistics of the boundary layer down to the inner region. Shah et al. [130] suggested that the outer peak is triggered by the adverse pressure gradient, and has its origin in an instability of the turbulent boundary layer. This may explain why it has not been possible to find a universal scaling for APG turbulent boundary layers.

As we noticed previously, the wall-unit scaling works perfectly in the near-wall region to scale the mean velocity as well as the turbulence intensities using the friction velocity and the viscous length scale (δ_ν). However, the similarity theory

developed by Rotta [120], Clauser [22] and Townsend [152] suggested that in the outer region the velocity deficit and the Reynolds stress quantities normalized by the friction velocity must be a function of y/Δ_{RC}, where $\Delta_{RC} = \delta_1 U_e/u_\tau$ is known as the Rotta-Clauser length scale [121].

In the case of strong APG and separation, the wall friction vanishes and u_τ no longer corresponds to an appropriate velocity scale. In many APG studies, as mentioned in [135], a velocity scale based on the pressure gradient has been used and is defined as $u_P \equiv (\nu \frac{1}{\rho}\frac{dP}{dx})^{1/3}$. Since the pressure velocity is meaningless in the ZPG case, Skote and Henningson [135] proposed a new mixed velocity scale between u_P and u_τ defined as

$$u_*^2 = u_\tau^2 + u_P^2 y^P \tag{4.2}$$

where $y^P \equiv y u_P/\nu$ represents the wall-distance normalized by the pressure velocity instead of u_τ.

Castillo and George [16] (CG) showed that the proper outer velocity scale in TBL is the freestream velocity U_e based on similarity analysis when the Reynolds number tends to infinity. They showed that the velocity deficit normalized by U_e collapses in the outer region using different cases of the pressure gradient. But at finite and intermediate Reynolds numbers, scaling with U_e is no longer valid for the entire outer layer. Furthermore, using U_e instead of u_τ in the velocity defect law (2.24) exhibits much better scaling.

Other types of velocity scales are presented and detailed in the following. Data from the current DNS of the non-equilibrium APG TBL were used to examine the validity of these velocity scales at moderate Reynolds numbers and medium APG.

4.2.1 Outer scaling

As previously noted, the friction velocity has been successfully used as a velocity scale in the near-wall region since viscous forces dominate there. On the other hand, the main challenge of boundary layer scaling is to find an appropriate velocity scale for the outer part, where viscosity is no longer dominant and large energy transfers occur in this region.

Further to the freestream velocity proposed in [16], Zagarola and Smits [172] also introduced an outer velocity scale in pipe flows based on the velocity deficit. This scaling was observed to better collapse the velocity profiles at different Reynolds numbers into a single curve in the outer region. Then, the Zagarola and Smits (ZS) scaling was generalized for all turbulent wall flows as follows

$$U_{ZS} = U_e \frac{\delta_1}{\delta} \tag{4.3}$$

This scaling was validated using TBLs subjected to different types of pressure gradients and successfully collapsed the velocity deficit profiles into a single curve. Castillo and Walker [17] showed the influence of upstream conditions on the development of the flow downstream. They have shown that the ZS scaling eliminates these effects as well as the dependence on the local Reynolds number [16]. The ZS scaling provides an outer velocity independent of the local Reynolds number as well as the strength of the pressure gradient.

Maciel et al. [89] investigate in great detail the outer region of TBLs subjected to an APG. Six APG and one ZPG databases (experimental and numerical) have been used to investigate the outer scaling of the velocity deficit and the Reynolds stresses. Four types of velocity and length scales have been compared, to conclude that the better scaling is obtained with U_{ZS} and δ for various velocity-defect. The ZS scaling is widely used in the literature as an appropriate outer velocity scale [157, 158, 163].

Fig. 4.7 shows a comparison between the CG scaling based on U_e, and the ZS scaling for our DNS data in a wide range of Reynolds numbers. Both types of scaling for the mean velocity deficit seem much better than the scaling using the friction velocity (not shown) which does not work at all to scale the outer part of TBL. U_{ZS} works perfectly to scale the mean velocity deficit where the profiles seem to almost collapse into a single curve. However, as mentioned in [16], the velocity deficit profiles are not expected to collapse into a single curve using the CG scaling as the Reynolds number stays moderate and far from the infinite hypothesis.

The ZS scaling is able to better scale the streamwise fluctuating velocity profiles of the current APG TBL than the scaling based on U_e. However, it fails to collapse all the velocity profiles of this APG TBL which is out of equilibrium into a single curve. Furthermore, the scaling of the Reynolds shear stress clearly shows the importance of ZS scaling, where the curves are much better collapsed than those scaled by the free stream velocity, except for the blue curve corresponding to $Re_\theta = 7600$ which may already be affected by the outlet conditions. The black curve corresponding to a profile relatively close to the inlet shows a different scaling behavior from the other profiles because it is located in a region with a fast transition between ZPG and APG, (see Fig. 4.7c to 4.7f).

Gungor et al. [46] introduced a new outer velocity scale that is used for both TBLs and mixing layer and is defined as twice the velocity deficit at the middle of the shear layer

$$U_m = 2[U_e - U(y = 0.5\delta)] \tag{4.4}$$

The scope of this scaling is rather limited as it can scale only the region where $y > 0.5\delta$ (not shown), when the efficiency of ZS scaling starts at $\sim 0.2\delta$. However,

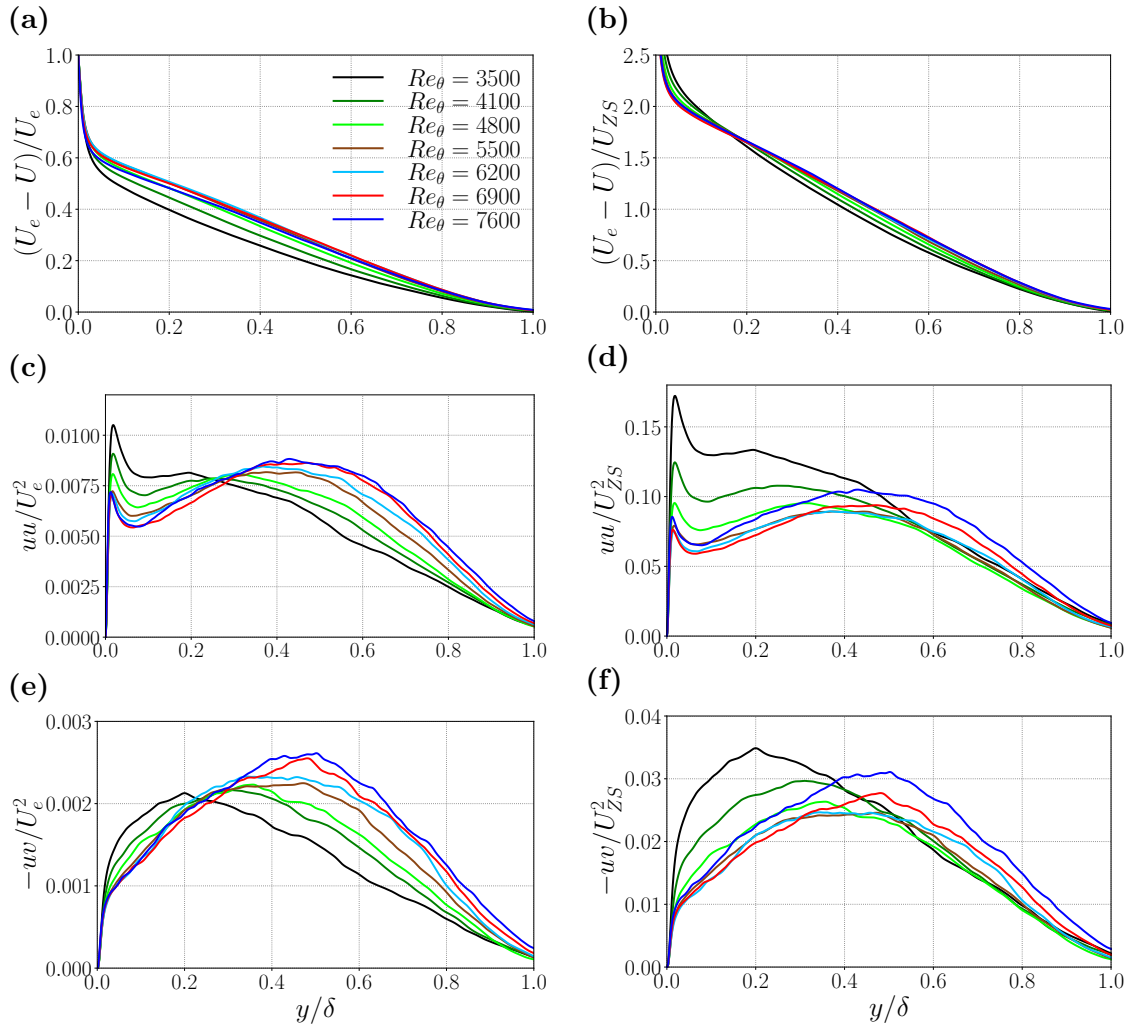

Fig. 4.7. The mean velocity deficit normalized by (a) U_e and (b) U_{ZS}. Streamwise velocity fluctuations normalized by (c) U_e and (d) U_{ZS}. Reynolds shear stress normalized by (e) U_e and (f) U_{ZS}. The velocity scales U_e, U_{ZS}, and the boundary layer thickness δ were collected at the corresponding streamwise position.

according to Gungor et al. [47] this mixing-layer-type scaling is expected to scale the strong APG case.

Based on several observations of the evolution of the freestream velocity as a function of the boundary layer thickness, Castillo and George [16] noticed that three basic behaviors can be observed corresponding to ZPG, APG and FPG cases. This observation leads to define the pressure gradient parameter Λ, where it should be constant for each case of pressure gradient and almost independent from the Reynolds number effects. The parameter Λ is defined as following

$$\Lambda \equiv \frac{\delta}{\rho U_e^2 d\delta/dx}\frac{dP_e}{dx} = -\frac{\delta}{U_e d\delta/dx}\frac{dU_e}{dx} \tag{4.5}$$

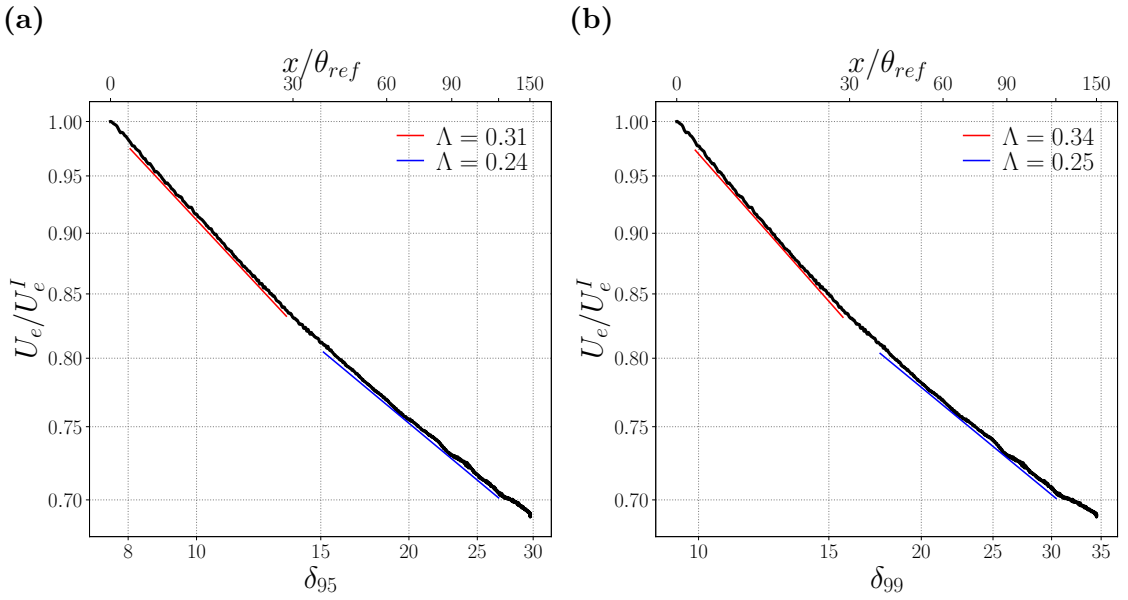

Fig. 4.8. Pressure gradient parameter Λ, fitted from $\delta \sim U_e^{-1/\Lambda}$ for two definition of the boundary layer thickness. (a) δ_{95} (b) δ_{99}.

As mentioned before, Λ = constant in each case of TBL flows ($\Lambda = 0$ in ZPG case), and in the presence of pressure gradient ($\Lambda \neq 0$). A constant value of Λ leads to a variation of the boundary layer thickness which goes like $\delta \sim U_e^{-1/\Lambda}$. Therefore, to calculate the value of Λ in the current APG TBL, one must simply determine the slope of U_e vs δ in a log-log plot. Indeed, for TBL with a pressure gradient, the boundary layer thickness is not as clearly defined as for ZPG TBL as the mean velocity profile exhibits a maximum larger than the external velocity. Moreover, DNS data do not allow us to obtain a very good convergence of the mean velocity profile. In that case, using the usual definition of δ as being the position such as $U = 0.99U_e$ can be inaccurate. Srinath et al. [145] have shown with experimental results that the definition of the boundary layer thickness can modify slightly the value of the CG parameter. This is why two definitions of boundary layer thickness (δ_{95} and δ_{99}) are used to check the sensitivity of Λ to the definition of δ.

As show by Castillo and George [16], Λ is around 0.22 for very strong APG (close to separation) [105] and increase to 0.23 in a strong APG case [87]. Referring to different mild and moderate APG results CG found that the value of Λ varies from 0.189 and 0.279. In our case, we notice two different values in each case of Fig. 4.8 where the red fit corresponding to the transition region from ZPG to APG which has a completely different behavior from the APG one obtained by the blue line. Fig. 4.8 shows that the values of Λ with both definitions of boundary layer thickness are quite similar in the APG domain far enough from the inlet obtained

from ZPG and not affected by the outlet condition corresponding to a range of Reynolds number of $Re_\theta \simeq 5000$ to 7300. In view of the uncertainty of the fit, the value of 0.24 to 0.25 is very close to the value 0.25 observed by CG in the case of moderate adverse pressure gradient database of Bradshaw [11] corresponding to a flow far from separation.

4.2.2 Scaling based on the momentum flux

On the other hand, Lozano-Durán and Bae [85] have hypothesized in their work that the wall is not the element that organizes the momentum-carrying eddies, whose intensities and sizes are controlled instead by the mean production rate of turbulent kinetic energy, i.e, the mean momentum flux and mean shear control these eddies with no explicit reference to the distance to the wall. As a consequence, they proposed the following characteristic velocity scale

$$u^* \equiv \sqrt{-\langle uv \rangle} \tag{4.6}$$

A characteristic time scale based on the mean shear was also proposed and interpreted as the average time required for the eddies to extract energy from the mean shear

$$t^* \equiv \left(\frac{\partial \langle U \rangle}{\partial y} \right)^{-1}. \tag{4.7}$$

An associated length scale is defined as $l^* \equiv u^* t^*$.

This scaling has been validated on standard channel flows at $Re_\tau = 550$ as well as forced channel flows to prescribed parametric mean velocity profiles in order to force the flows to encounter very different dynamics. For all these cases u^* was shown to collapse successfully the turbulence intensity profiles into a single curve. The characteristic velocity u^* based on the Reynolds shear stress i.e. on the mean production rate of turbulent kinetic energy shows that the production rate has a common "footprint" in the three turbulence intensities.

The scaling u^* was tested on the three turbulence intensities for the present DNS of APG TBL. The three components of the velocity fluctuations are presented in Fig. 4.9 (solid lines) at four streamwise positions corresponding to $Re_\theta = 4500$, 5500, 6500 and 7600 within a streamwise range where the pressure gradient is not constant. Scaling of APG TBL was compared with ZPG TBL of Sillero et al. [131, 132] at similar Reynolds numbers (unless $Re_\theta = 7600$) and the ZPG curves are plotted using the dashed lines.

Fig. 4.9b, 4.9d and 4.9f show the evolution of Reynolds stresses normalized by u^* as a function of wall-normal distance scaled with the outer length scale δ in order

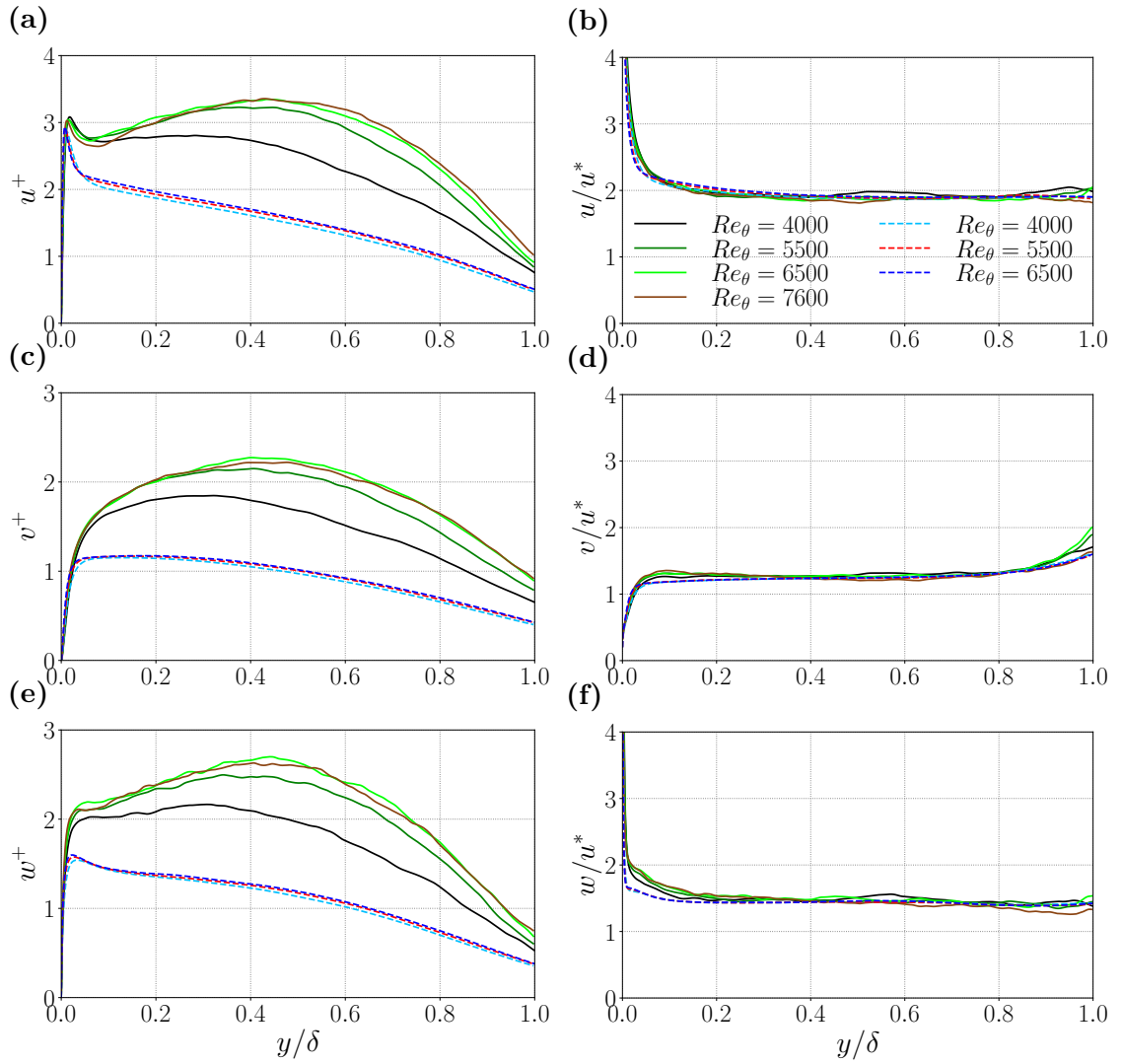

Fig. 4.9. Streamwise, wall-normal, and spanwise root-mean-squared velocity fluctuations scaled with (a,c,e) u_τ and (b,d,f) u^*, respectively. All the figures are plotted as a function of wall distance normalized by the boundary layer thickness δ. Solid lines are for the current APG TBL and the dashed lines for the ZPG case [131, 132].

to focus on the outer layer. Each velocity fluctuations normalized by u^* collapse for different Reynolds numbers and have a constant value from the upper part of the log region ($y^+ > 100$) up to the top of the boundary layer for u and w and up to 0.8δ for v. These constant values are 2, 1.3 and 1.8 for the streamwise, wall-normal and spanwise Reynolds stress respectively. u^* scales the outer region much better than the wall-unit scaling that presents a clear dependence on the Reynolds number except in the near-wall region as well as a strong sensitivity to the presence of adverse pressure gradient. Lozano-Durán and Bae [85] interpreted the increase in the wall-normal Reynolds stress normalized by u^* very far from the wall as a lack of mean shear, where this scaling is no longer applicable there.

The same quantities were plotted in Fig. 4.10 as a function of wall-unit distance y^+ in order to focus on the efficiency of u^* scaling in the buffer region. The scaling using u^* leads to collapse the fluctuating velocity profiles into a single curve in the inner part but it is not as accurate in this region except for the normal fluctuating velocity.

The efficiency of the u^* scaling, already validated on channel flow [85], to scale all turbulent intensities of our APG TBL is clearly demonstrated. It is able to scale both the inner and the outer region in an investigated Reynolds number range. This scaling gives some indication of the property of the flow. However, the weak point of this scaling is the dependence of a local internal quantity (Reynolds shear stress) which varies with boundary layer position and it was not based on external or global quantities e.g. U_e.

4.2.3 Embedded shear layer scaling

As mentioned in Schatzman and Thomas [124], the existence of an inflection point (IP) in the mean velocity profile implies the existence of an inviscid instability due to the instantaneous inflectional profiles. They also pointed out the important effect of the coherent large-scale spanwise-oriented vorticity located in the shear layer, on the spatial and temporal development of the flow, especially at a sufficient distance from the wall.

Regarding the previous observation, the authors have introduced a scaling related to the shear layer, and the local embedded shear layer vorticity thickness δ_ω has been proposed as the length scale,

$$\delta_\omega \equiv \frac{(U_e - \overline{U})_{IP}}{(d\overline{U}/dy)_{IP}}, \tag{4.8}$$

where $(.)_{IP}$ represents the corresponding quantity evaluated at the inflection point position of the mean velocity profile. Moreover, the local velocity deficit at the inflection point is taken as the velocity scale of the present scaling

$$U_d \equiv (U_e - \overline{U})_{IP} \tag{4.9}$$

Similarity variables are defined as

$$\eta \equiv \frac{y - y_{IP}}{\delta_\omega},\ U^* \equiv \frac{U_e - \overline{U}}{U_d}, \tag{4.10}$$

where η is the distance from the inflection point normalized by local δ_ω, and U^* is the local velocity deficit normalized by U_d (i.e. normalized by its value at the

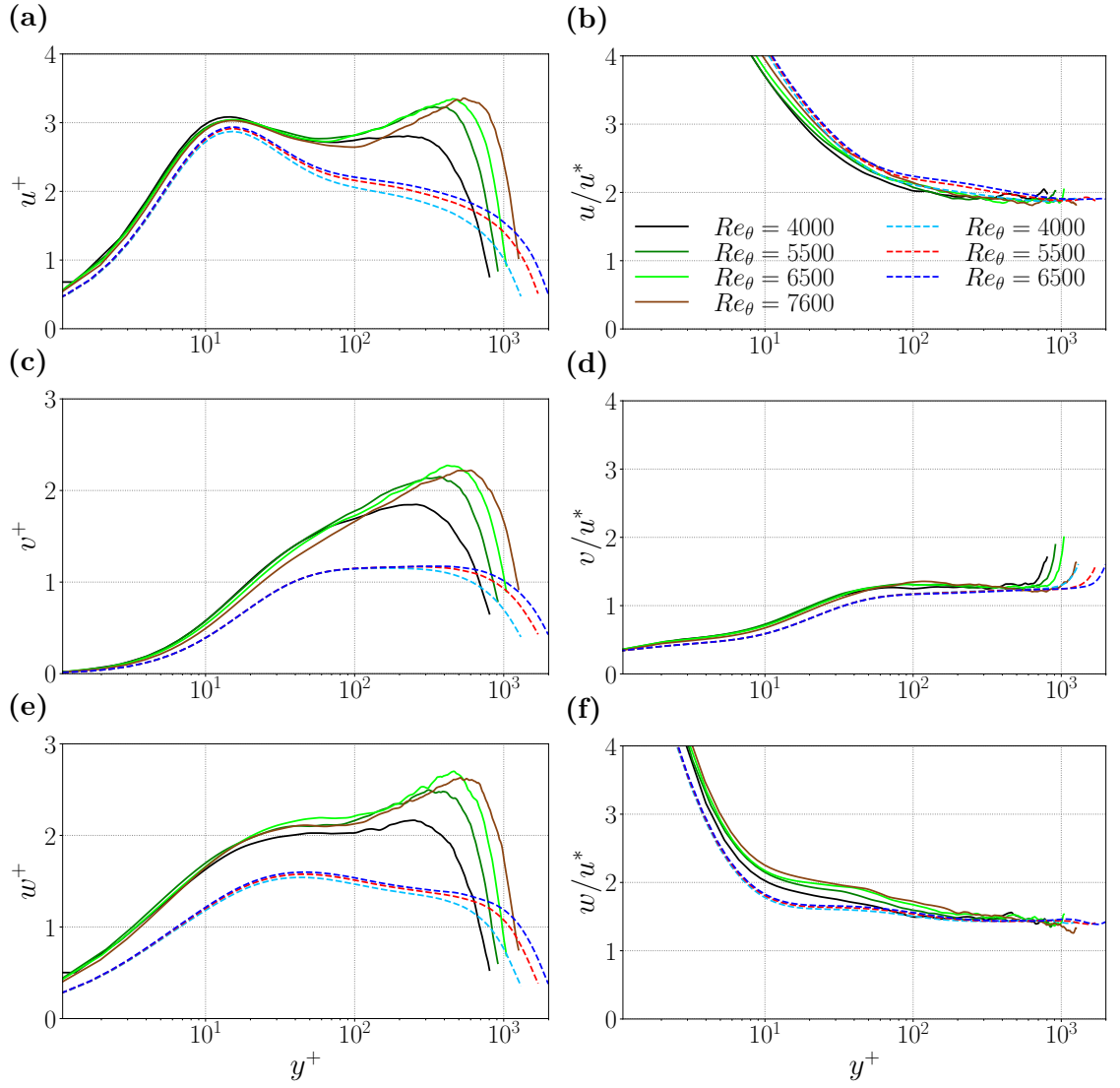

Fig. 4.10. Same quantities as Fig. 4.9 plotted as a function of wall-unit normal distance.

inflection point).

The shear layer scaling was tested by Schatzman and Thomas [124] over a ramp boundary layer in presence of a moving airfoil in the freestream region. In this experiment the APG was varying within a time cycle in a range $-3 < \beta < 5$. The length and velocity scales were tested by plotting the evolution of U^* as a function of η at several points in the time cycle which corresponds to different APG behaviors. All the mean velocity deficit profiles were found to collapse onto a single curve. The embedded shear scaling was found to better perform than the ZS scaling.

This scaling was tested using data from the current DNS of APG TBL. The velocity deficit at six streamwise positions (corresponding to various APG conditions) are presented in Fig. 4.11a using the embedded shear layer scaling. It is clearly

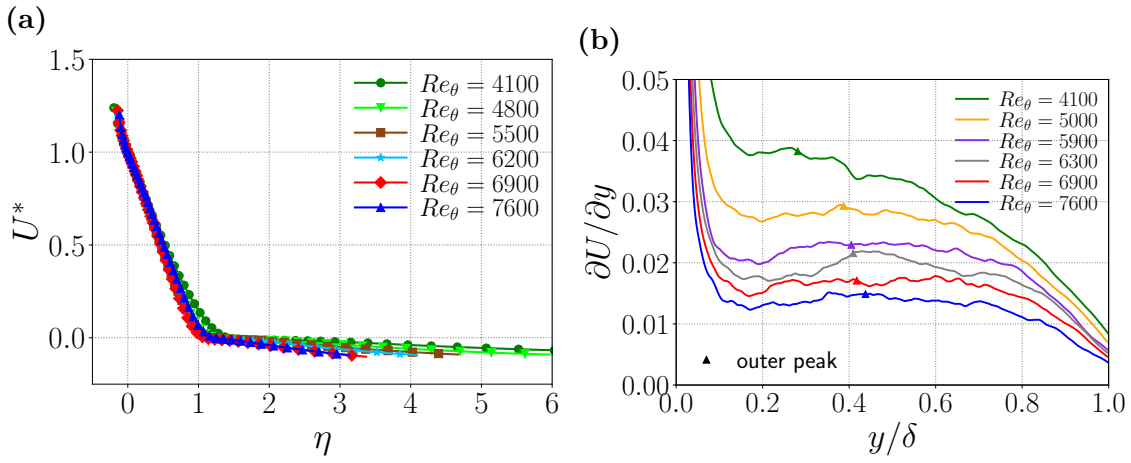

Fig. 4.11. (a) Mean velocity deficit profiles from the current APG TBL at various streamwise positions using embedded shear layer scaling defined in (4.10). (b) Evolution of $\partial U/\partial y$ along the boundary layer at six streamwise positions. Small triangles represent the positions of outer peak of streamwise Reynolds stress.

shown that the profiles of U^* as a function of η almost collapse into a single curve especially near the inflection point (i.e. $\eta = 0$) as by construction all the curves cross at this point.

On the other hand, Fig. 4.11b shows the evolution of $\frac{\partial U}{\partial y}$ as function of wall distance normalized by local δ. Note that the maximum of this profile in the outer region ($y > 0.2\delta$) corresponds to the desired inflection point. However, one can see that it is not easy to locate this maximum because the profile is slightly wavy and it becomes like a plateau when moving downstream ($Re_\theta > 6500$). Furthermore, the aforementioned position of the outer peak of the Reynolds stress is also presented in the same figure. Despite the difficulty in locating the position of the IP, one can see that both positions are approximately close which agrees with the results of Kitsios et al. [67] stating that the outer peak of the velocity fluctuations is located at the same position of an inflection point in the mean streamwise velocity.

Moreover, the present velocity scale U_d was tested on the streamwise velocity fluctuation and was compared with the scaling using the freestream velocity U_e at the same streamwise positions used in the velocity deficit scaling (see Fig. 4.12). The near-wall profiles are not plotted as these scalings are not supposed to scale the inner layer. In the experiments of Schatzman and Thomas [124], the embedded shear layer velocity scale was able to perfectly collapse the streamwise velocity profiles. The streamwise Reynolds stress normalized by U_d is presented in Fig. 4.12b. U_d encloses the Reynolds stress curves better than U_e, excluding the dark green line corresponding to $Re_\theta = 4100$ which is still affected by the ZPG/APG transition as well as the

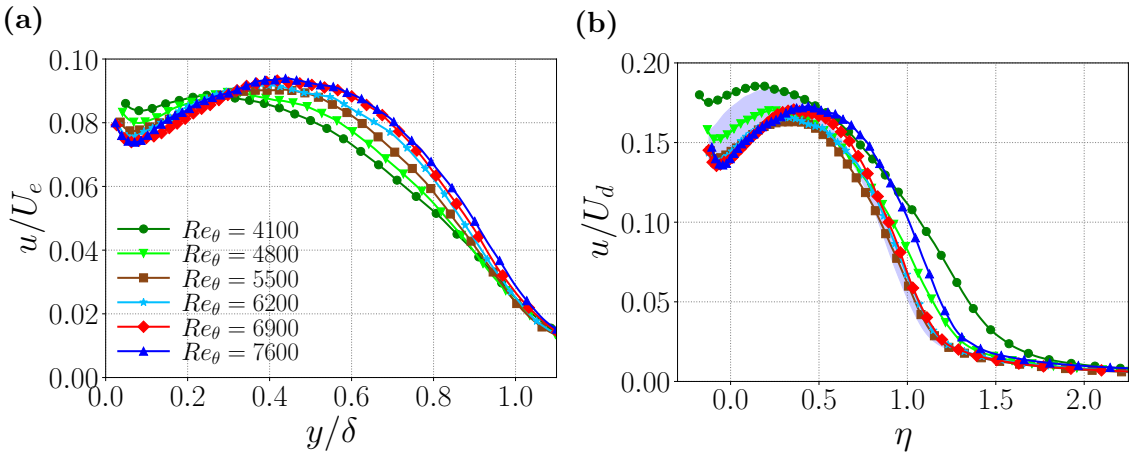

Fig. 4.12. The streamwise Reynolds stress profiles normalized (a) by U_e as function of y/δ and (b) by U_d as function of η at different Reynolds numbers. The blue shadowed area represents the streamwise Reynolds stress, normalized by U_d taking into account the error bar on the position of the inflection point.

blue line ($Re_\theta = 7600$) in the vicinity of the outlet which may be influenced by the outlet conditions. The difficulties in performing the embedded shear layer scaling come from the high dependence on the position of the mean velocity inflection point where the length and velocity scales are evaluated. Moreover, the inflection point is located close to the logarithmic region, which complicates the accurate determination of its position as shown in Fig. 4.11b. In this study, the inflection point at such a position is determined by fitting the profile of the second derivative of the mean velocity ($\partial^2 U/\partial y^2$) which strongly oscillates around zero (i.e. IP position), then the intersection with zero is considered as the inflection point. Therefore, the velocity scale U_d used to scale the Reynolds stress profiles in Fig. 4.12b was calculated based on an approximate determination of the location of the inflection point.

In order to analyze the effect of the IP position on this scaling, we focused on a single streamwise position (corresponding to $Re_\theta = 6200$) and we calculated the velocity scales based on all the possible values of the IP. The streamwise fluctuating velocity at the corresponding streamwise position was normalized using all the corresponding values of velocity scales U_d. The scaled profiles are plotted in Fig. 4.12b covering the blue shadowed area. It is clear that the position of IP has a great impact on the scaling of the Reynolds stress around its position, then the dependence on the IP position decrease as moving away from it. Furthermore, it is clearly shown that most of the scaled Reynolds stress profiles are included in this area that presents the relevance of this scaling when the IP is precisely detected.

4.2.4 Shear scaling

A new characteristic length scale was proposed by Sekimoto et al. [129] to be a universal scaling for the large and small scales and free from the definition of boundary layer thickness δ. The new length scale is based on the non-dimensional shear rate parameter defined by [27] as

$$S_c \equiv \frac{\partial U}{\partial y}\frac{q^2}{|\epsilon|}, \tag{4.11}$$

where $q^2 = \langle u_i u_i \rangle = 2K$, K is the mean kinetic energy and $\epsilon = -\nu\langle\left(\partial_j u_i\right)\left(\partial_j u_i\right)\rangle$ is the pseudo-dissipation rate.

The Corrsin shear parameter S_c illustrates the importance of the interaction of the mean shear with the energy-containing turbulent structures [57, 47]. The shear thickness δ^* was proposed as a relevant length scale and defined as the wall-normal position of the peak of the S_c profile. The suggested length scale was tested and validated by Sekimoto et al. [129] using turbulent channel and boundary layer flows with various pressure gradients. The profile of S_c with respect to δ^* for all investigated flows exhibits similar behavior for wall distance $y < \delta^*$. In addition, the authors distinguished between two regions: $y < \delta^*$ is called an 'active' shear-driven layer and $y > \delta^*$ 'inactive' decaying turbulence. This partition is associated with the effect of the shear which becomes negligible very far from the wall so that a shear-based scaling is not expected to work in this region.

They also proposed a characteristic velocity scale mixed between the friction and pressure velocity using a new definition related to the shear-thickness. The pressure velocity is re-defined as $u_P^* = \sqrt{\delta^* P_e'}$, where P_e' is the streamwise pressure gradient at the edge of boundary layer. The Clauser's pressure gradient parameter is also noted as, $\beta^* = (u_P^*/u\tau)^2$. As a consequence, the relevant velocity scale is provided as

$$u^* = u_P^* \sqrt{\frac{1}{\beta^*} + \frac{y}{\delta^*}} \tag{4.12}$$

u^* was shown by Sekimoto et al. [129] to scale each Reynolds stress term for the various flows, except for the near-wall region.

A similar analysis with current APG TBL shows that this scaling does not perform well. The main reason is probably because this scaling is designed to scale an equilibrium wall-bounded flow and our APG boundary layer is out of equilibrium. Moreover, the current scaling is based on the position of the maximum Corrsin shear parameter and the determination of this position requires very converged statistics which is not the case with our DNS results. As shown in Fig. 4.13, the S_c profile is very disturbed, especially around the position of the peak which makes the exact determination of δ^* very difficult and hence the scaling of Reynolds stresses will

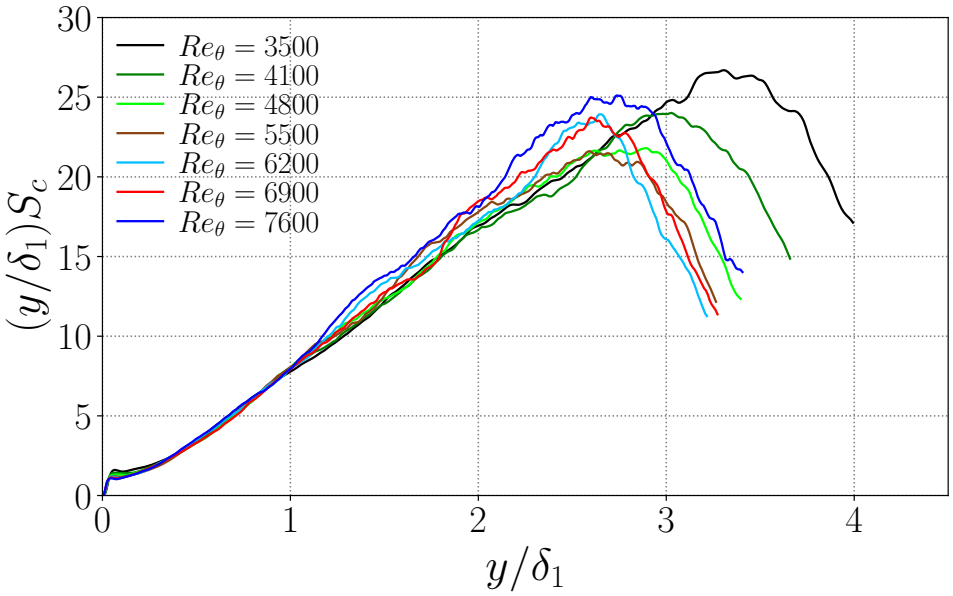

Fig. 4.13. The premultiplied Corrsin shear parameter S_c as function of the displacement thickness δ_1 at different Reynolds numbers. The peak position corresponds to the shear thickness δ^*.

be strongly affected. It is therefore difficult to conclude about the validity of this scaling.

4.3 Characteristic length scales

In addition to the outer length scale (δ) and the inner one based on the wall-unit (δ_ν) the Taylor micro-scale and the integral scale are known to play an important role in turbulent flows. Even if the estimation of these scales requires a very large number of uncorrelated data, estimations of each of these scales will now be presented.

4.3.1 Taylor micro-scale

The Taylor micro-scale is defined in Larssen and Devenport [73] by $\lambda = \sqrt{15\nu u^2/\epsilon}$ in isotropic flows, where u^2 is the mean streamwise turbulence intensity and ϵ is the turbulent dissipation rate. However, in anisotropic turbulence, the term u^2 must be replaced by $2K/3$, where K is the turbulent kinetic energy. Then, the mentioned micro-scale is now defined as $\lambda = \sqrt{10\nu K/\epsilon}$.

The evolution of the micro-scale along the boundary layer at a streamwise position corresponding to $Re_\theta = 6900$ is presented and normalized by the outer scale (δ) in Fig. 4.14a in comparison with the ZPG case of Sillero et al. [131, 132]. In Fig. 4.14b, the same quantities have been shown using the wall-unit scaling. As pre-

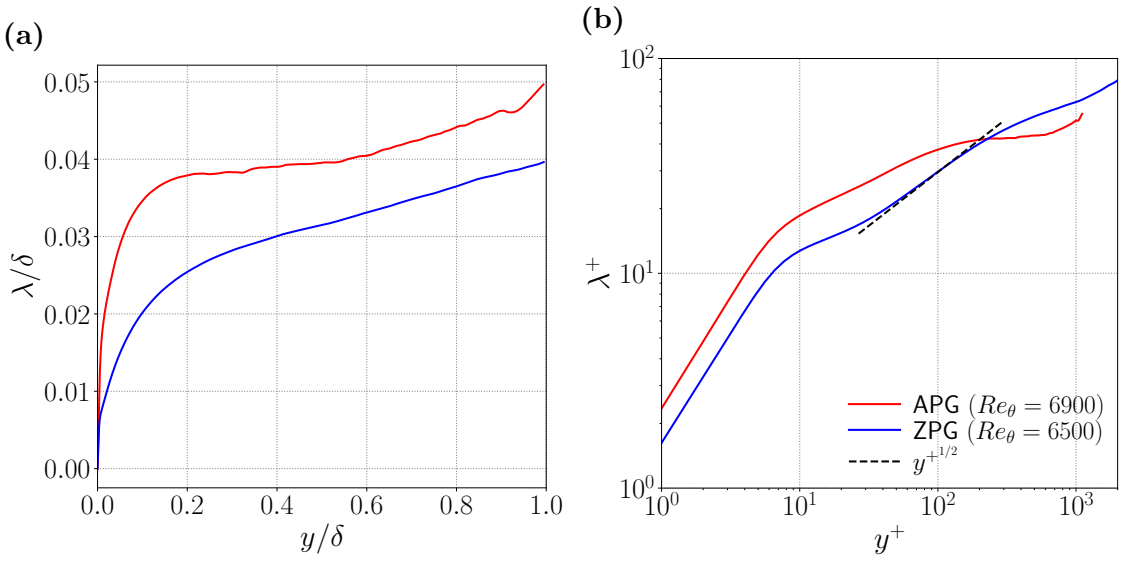

Fig. 4.14. Taylor micro-scale λ as function of wall-normal positions normalized by (a) δ and (b) δ_ν. The current APG case is evaluated at a streamwise position such that $Re_\theta = 6900$ (red line) and $Re_\theta = 6500$ for a ZPG TBL collected from the database of Sillero et al. [131, 132] (blue line).

dicted by Dallas et al. [29] on the basis of the number density of fluctuating velocity stagnation points, which scales as $1/y^+$ in the region where production approximately equals dissipation, $\lambda \sim \sqrt{y^+}$ in the log region for the ZPG case. However, the scaling for the APG case is slightly different in the log region which is shifted toward low $y+$.

4.3.2 Integral length scale

The time auto-correlation function is defined in Benedict and Gould [9] by

$$R_{uu}(\tau) = \frac{\langle u(t)u(t+\tau)\rangle}{\langle u^2(t)\rangle}, \tag{4.13}$$

where t is the time and τ is the time interval over which the correlation function is calculated.

R_{uu} is calculated over 40 characteristic times based on the outer quantities (U_e and δ) evaluated at the outlet. It is presented at several wall distances up to $y^+ = 300$ in Fig. 4.15a. The integral time scale is defined in [9] as

$$T_{uu} \equiv \int_0^\infty R_{uu}(t)dt \tag{4.14}$$

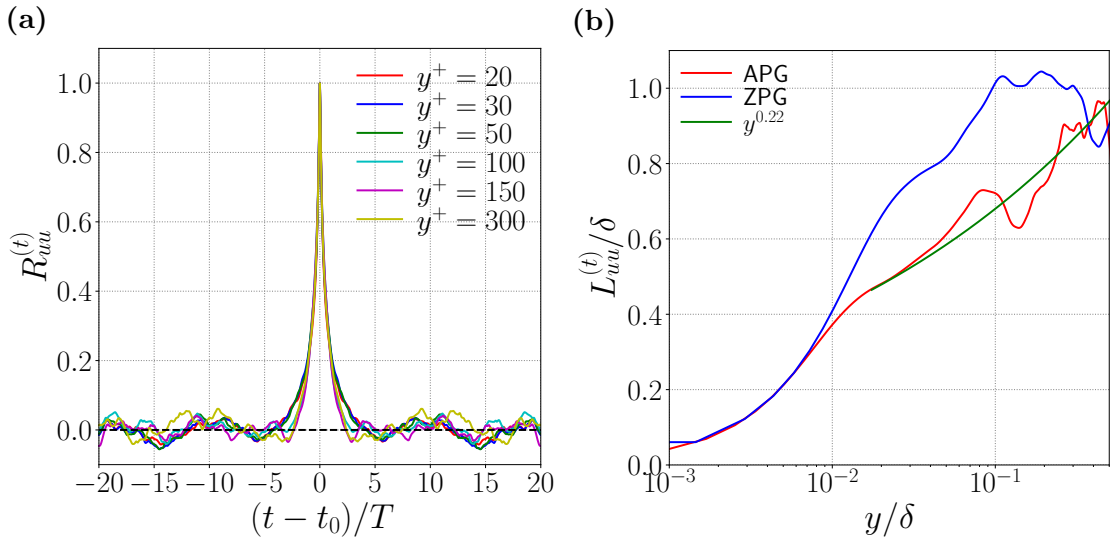

Fig. 4.15. (a) The time auto-correlation function of the streamwise velocity fluctuations for the current APG TBL at various wall distances (it is calculated using the 2D well-resolved planes at $Re_\theta = 7240$). (b) The integral length scale as a function of the wall distance, normalized by the boundary layer thickness δ. The APG case is evaluated at the streamwise position such that $Re_\theta = 7240$ (red line) and $Re_\theta = 2068$ for the ZPG TBL of Solak and Laval [140] (blue line). Fitting of the integral length scale profile for the APG case is presented in the log-layer and the lower part of the outer region (green line).

The integral length scale is related to T_{uu} by the following formula

$$L_{uu} = T_{uu}\langle U \rangle, \tag{4.15}$$

where $\langle U \rangle$ is the mean streamwise velocity. In Fig. 4.15b, the integral length scale normalized by δ of the current DNS of APG TBL (red line) is compared with the results of ZPG TBL of Solak and Laval [140] (blue line). The results are plotted up to 0.5δ as the profiles are not well converged in the upper part of the outer region. Despite this lack of convergence of the integral scale, the best fit was found to be $y^{0.22}$ in the log region. This fit is comparable with the fit $y^{1/3}$ observed in ZPG TBL at high Reynolds number by Vassilicos et al. [156]. However, the integral scale of the APG case is significantly lower than for the ZPG TBL DNS at small Reynolds number (see Fig. 4.15b).

4.4 Energy spectra of the streamwise velocity fluctuations

4.4.1 Spanwise energy spectra

The energy spectra of the streamwise velocity fluctuations are commonly used to investigate the energy transfer between different scales. As mentioned in chapter 2, Vassilicos et al. [156] proposed a modified model from the Townsend-Perry attached eddy model, by suggesting a new region in which the streamwise energy spectrum follow a k_x^{-m} scaling. However, this model holds only for very large Reynolds numbers. In addition, Srinath et al. [145] using an APG TBL experiments have noticed that (k_x^{-1}) spectrum is only valid for a single wall-normal distances in the log-layer. They have shown that the spectra at low wavenumber evolve with $E_{11} \sim (k_x\delta)^q$, where q is a weak function of the wall distance. This model can be derived from a very simple on-off model of the large-scale structure of streamwise velocity fluctuation given the hypothesis that these large-scale structures are space filling.

Most of the investigations are based on streamwise energy spectra of streamwise velocity fluctuations as this quantity is directly accessible by hot-wire measurement when using the Taylor hypothesis [5, 6, 158]. The important growth of the boundary layer thickness in our case with APG does not allow a direct calculation of energy spectra in the streamwise direction. Therefore, the energy spectra in the spanwise direction have been studied to identify the behavior of different scales of large-scale structures. Wang et al. [162] showed that the energy spectra of the streamwise fluctuating velocity in the streamwise and spanwise directions have a similar behavior using data from both ZPG boundary layer and channel flow. They investigated separately the two spectral peaks located in the inner and outer regions and have concluded that the outer large scales maintain a "footprint" down to the near-wall region.

Fig. 4.16 shows log-log plots of pre-multiplied energy spectra $k_z\phi_{uu}^+$ normalized by the wall-unit. The energy spectra have been computed from our DNS data over 1315 velocity fields which can be considered as resolved in time and averaged in a small streamwise domain (corresponding to 0.6δ) around the reference streamwise position ($Re_\theta = 7240$) at various wall distances. The spectrum profiles exhibit a large dissipative range without accumulation of energy at the largest wavenumbers which validates that the spatial resolution is enough to resolve small dissipative scales.

In Fig. 4.16a, the spectra are presented at 4 wall distances in the buffer and lower logarithmic layers. The spectrum behavior $\phi_{uu}^+ \sim k^{-1}$ proposed in the Townsend-

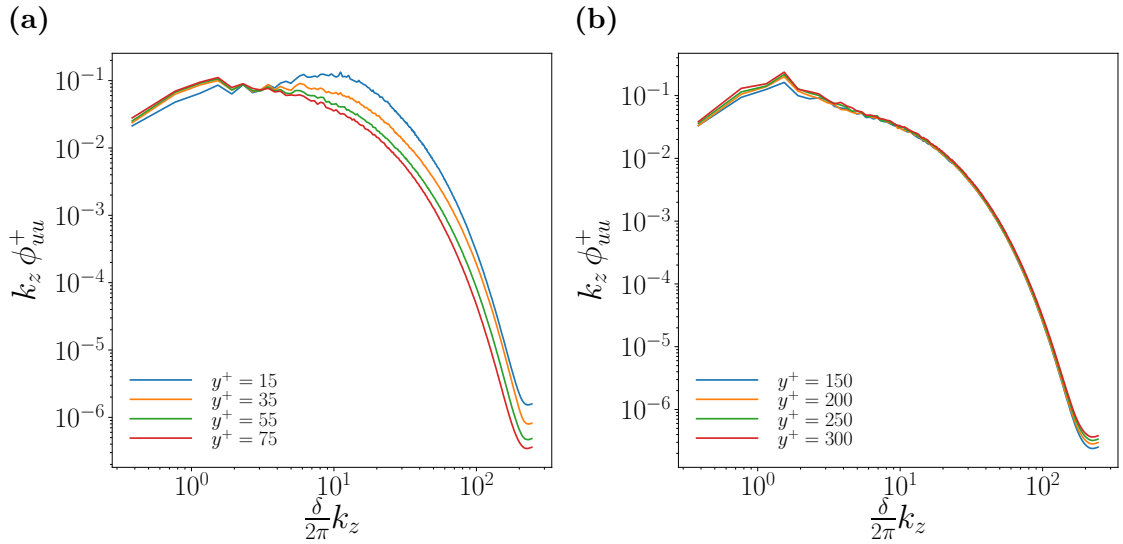

Fig. 4.16. Pre-multiplied spanwise energy spectra at different wall distances as function of wavenumber normalized by δ at $Re_\theta = 7240$. The energy spectra were computed over 1315 streamwise velocity fields in a domain corresponding to $7200 < Re_\theta < 7260$ which corresponds to approximately 0.6 local boundary layer thickness at the reference streamwise position. (a) corresponding to positions in the buffer and lower logarithmic regions (b) for the upper part of the log-layer.

Perry model was not observed in the region corresponding to large scales (corresponding to small wavenumbers) except for a few wall distances around 35^+. Then the slope of the spectra decreases far from the wall. Despite the limited convergence due to the fact that the velocity fields used for the analysis are time-resolved, it can be seen that the energy spectrum profile follows k^{-q} as mentioned in [145], where the exponent q increases when moving from the wall. Further study should be devoted to the variation of this slope with distance from the wall. The previous observation is in agreement with the results observed in [81] using streamwise spectra of the streamwise velocity fluctuation from a DNS of channel flow up to $Re_\tau \approx 5200$. This can be associated with the self-similar behavior of the large-scale structures as it will be investigated in section 2.2.3.

On the other hand, Fig. 4.16b shows the energy spectra in the upper part of the logarithmic layer, where the spectra appear almost similar, and a scaling close to k^{-1} cannot be observed.

A deeper analysis of the spectra is proposed in Fig. 4.17 using lin-log plot as a function of the wavelength. In Fig. 4.17a and 4.17c, λ_z was normalized by the boundary layer thickness, and the viscous wall-unit scaling was used in Fig. 4.17b and 4.17d. The energy spectrum at wall distance $y^+ = 15$ presents a peak corresponding to a wavelength $\lambda_z^+ \sim 125$, in agreement with the results obtained in [162]. This peak can be related to the inner peak of the streamwise velocity fluctuation

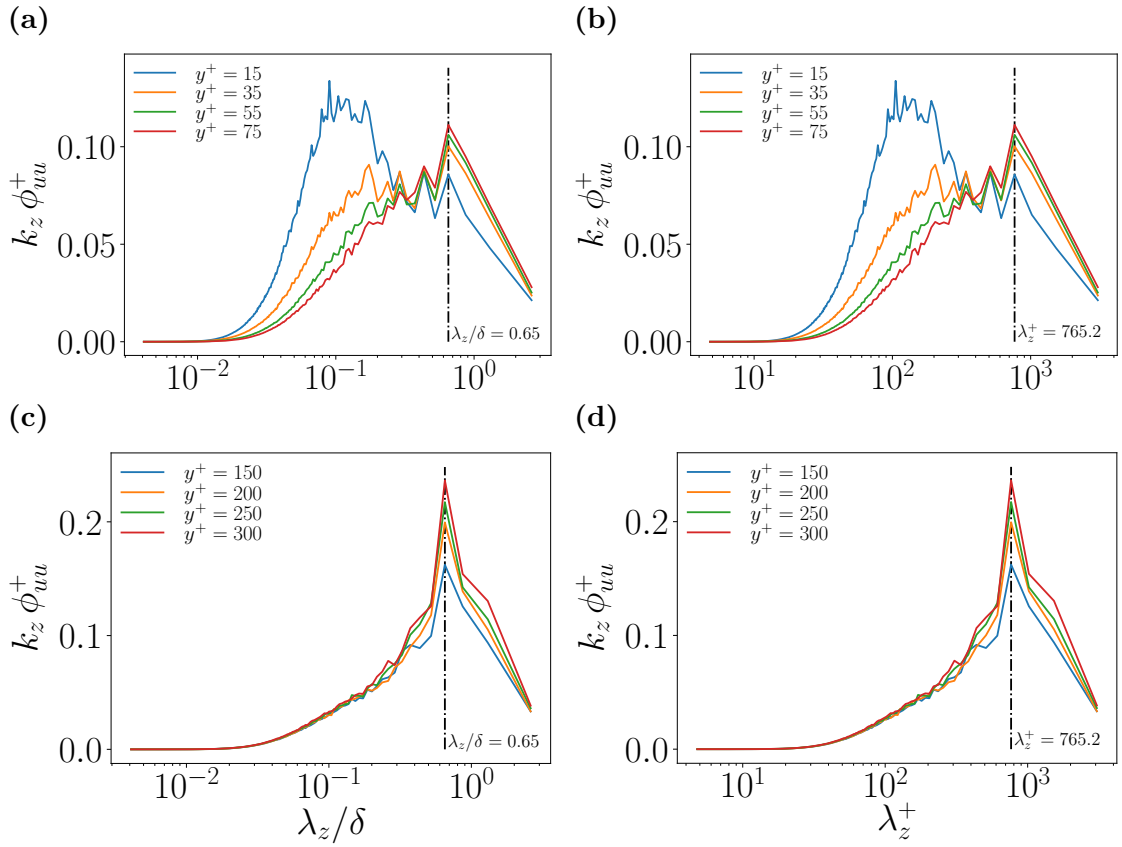

Fig. 4.17. The same energy spectra of Fig. 4.16 plotted as function of wavelength normalized by δ and unit wall. (a) and (b) corresponding to positions in the buffer and lower logarithmic regions; (c) and (d) for the upper part of the log-layer. The dash-doted black line corresponds to the wavelength of the common peak.

associated to the spacing between near-wall streaks. The use of lin-log plot better shows that the k^{-1} law is not valid for this APG TBL and is observed only at few wall-distances ($y^+ \sim 35$) on a limited range of wavelength.

Since our inlet conditions were built from a four times duplication of the original ZPG fields in the spanwise direction, we noticed that a peak appears at all wall-normal positions and corresponding to a wavelength λ_z equal to the spanwise width of the original ZPG domain. The position of these peaks is marked by the vertical dash-doted line in Fig. 4.17. This peak could be due to a reminiscence of the periodization of the inlet even if a weak random noise was added precisely to avoid this effect. However, by monitoring the spanwise energy spectra at several streamwise positions, we observed that the wavenumbers with zero energy at the inlet due to the periodization were completely filled in the second part of the simulation domain. Therefore, we expect to see no more effect of the periodization close to the outlet. The wavelength associated with this peak is of the order of 2/3 of the boundary layer thickness and could therefore be a meaningful spanwise scale.

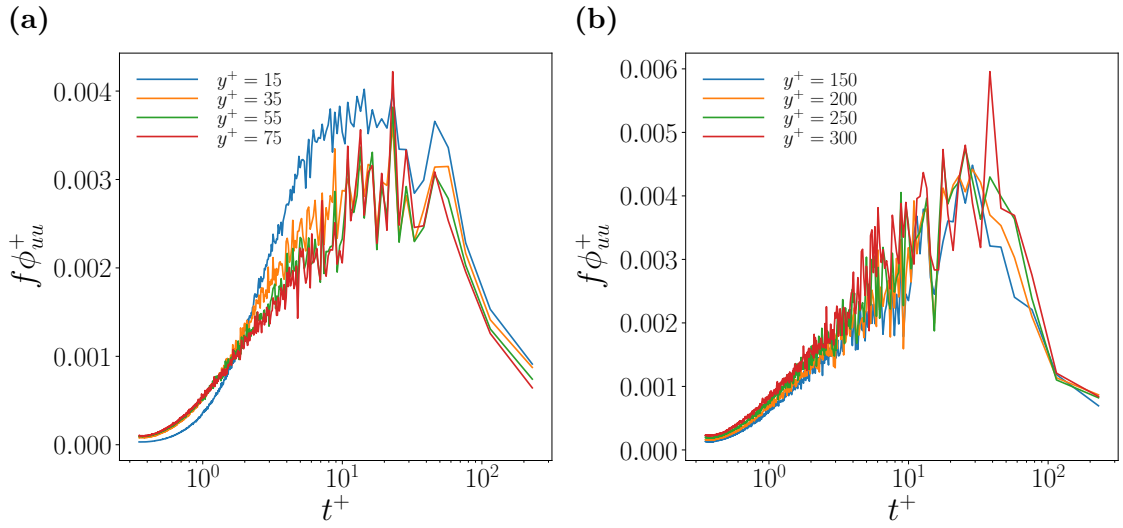

Fig. 4.18. Pre-multiplied time spectra as a function of time, normalized by wall-units. The spectra were computed over the entire spanwise direction in a streamwise domain corresponding to $7180 < Re_\theta < 7270$ which corresponds to approximately 0.8 local boundary layer thickness at the reference streamwise position. (a) corresponding to positions in the buffer and lower logarithmic regions (b) for the upper part of the log-layer.

4.4.2 Time spectra

In parallel with the spatial energy spectra, some investigations were dedicated to the temporal spectrum [125, 123, 100, 157].

In Fig. 4.18, the pre-multiplied time spectra were presented at same wall-normal positions as Fig. 4.16. The energy spectra have been calculated using the sufficiently time-resolved 3D database with time spacing $\Delta t^+ = 1.2$. The spectra are converged using 1280 grid points in the spanwise direction and 200 grid points ($\sim 0.8\delta$) in the streamwise direction. The time spectra computed from the 3 time-resolved YZ planes happen to be less converged as only the spanwise direction can be used for the average.

Based on Townsend-Perry model, it is expected to see a plateau in the pre-multiplied time spectra which correspond to the -1 slope behavior in the spatial spectrum profile. As our database is not well converged, important fluctuations are presented at low frequencies in which the mentioned plateau should be seen. However, the general evolution of the profiles in Fig. 4.18a shows that only the profile at $y^+ = 35$ can be considered having a plateau similarly to what has been obtained using the spanwise spectra. On the other hand, this plateau can not be observed further away in the upper part of the logarithmic layer even if the convergence of the spectra does not allow us to be fully affirmative (see Fig. 4.18b).

Chapter 5

Coherent structures of streamwise fluctuating velocity

Various types of coherent structures have been described in chapter 2 as well as the effects of the presence of adverse pressure gradient on the structures motion. In the present chapter, we will focus on the coherent structures of the streamwise velocity fluctuations, especially the large-scale structures located in the outer region. These large-scale motions are widely related in the literature to the hairpin vortex packets as mentioned in section 2.2.4. Special attention has been devoted to the investigation of coherent structures to the interactions between the inner and outer structures [56].

In the current study, we distinguished between low and high momentum regions of the streamwise velocity fluctuations with a special focusing on the largest scales. Therefore, a good spatial-temporal resolution is required to carefully investigate these structures. For that purpose, the 3D time-resolved database collected from the current DNS has been used to investigate the contribution of the coherent motion to the Reynolds stresses. As it has been shown for ZPG TBL by Solak and Laval [140], these large-scale structures have a very complex shape which vary in time.

5.1 Near-wall streaks

In order to investigate the impact of the adverse pressure gradient on the near-wall coherent structures, a comparison of the positive and negative streamwise velocity fluctuations between the current DNS of TBL subjected to an APG in a domain corresponding to $Re_\tau = 970 - 1270$ and the DNS of the channel flow of Del Álamo et al. [32] at $Re_\tau = 950$ has been performed. For that purpose, planes parallel to the wall at $y^+ = 15$ with dimensions of 12000^+ and 3000^+ in the streamwise and spanwise directions respectively were presented in Fig. 5.1.

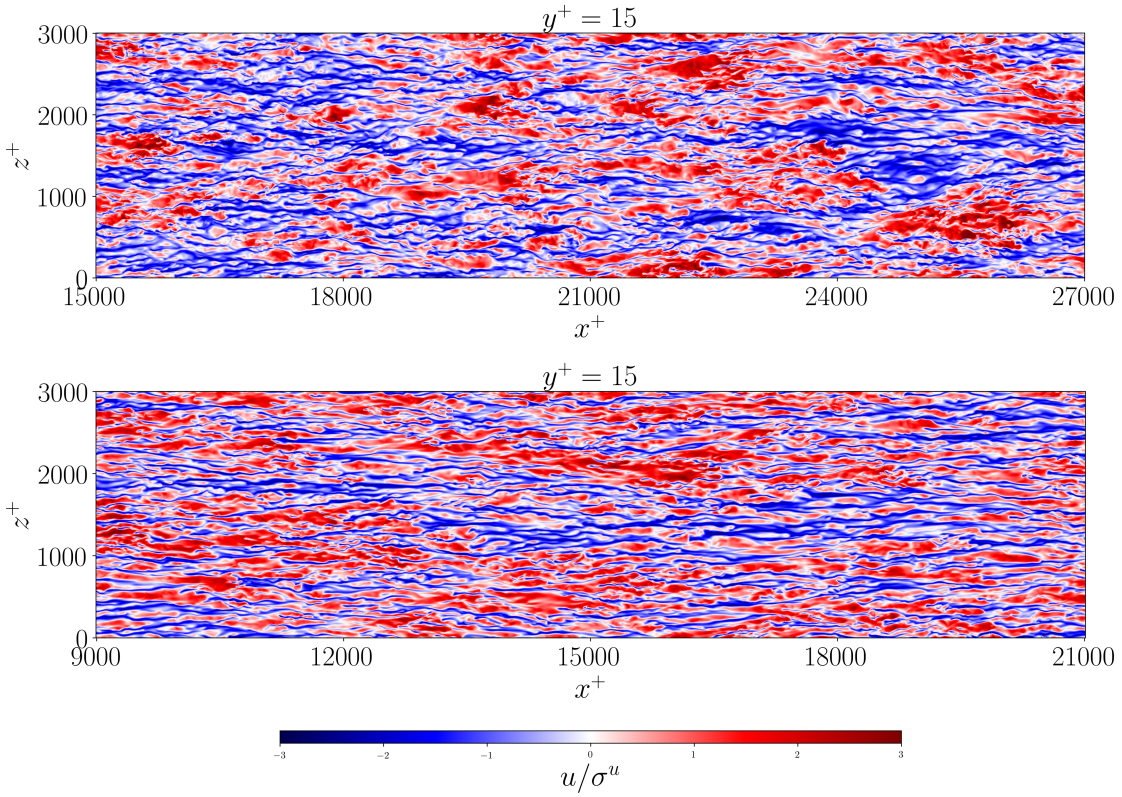

Fig. 5.1. Near-wall streaks represented using streamwise-spanwise planes at $y^+ = 15$ from the current APG TBL (top) and the DNS of channel flow of Del Álamo et al. [32] (bottom). The streamwise velocity flucuation is normalised by its standard deviation. The red color corresponds to the high-speed streaks and the blue one to low-speed streaks.

One can notice that in both cases, the low-speed streaks are thinner and more elongated than high-speed ones. It is not easy to conclude the effect of the pressure gradient using a single snapshot but one can notice that the low-speed streaks and high-speed streaks seem less regular (less elongated) in presence of APG. This is probably the footprint of more intense large-scale structures responsible for the outer peak in the Reynolds stress profiles.

5.2 Spatial two-point correlation

The two-point correlation is commonly used to investigate the average statistics of large-scale structures. The two-point correlation function of the streamwise fluctuating velocity was calculated as following and averaged over the homogeneous spanwise direction and time.

$$R_{uu}(x, y; x_0, y_0) = \frac{\langle u(x - x_0, y - y_0)u(x, y)\rangle}{\langle u(x_0, y_0)\rangle^2} \tag{5.1}$$

where (x_0, y_0) are the coordinate of the fix point.

The results for the present APG TBL are compared to the same statistics for the DNS of ZPG TBL over a flat plate at $Re_\theta \simeq 2000$ which was used to generate the inlet conditions [140]. In all figures of two-point correlation, solid lines are devoted for the current APG contours and the dash-doted ones for the ZPG case. In Fig. 5.2, the two-point correlation in the streamwise wall-normal plane normalized by the outer length scale δ is shown at four wall-normal reference positions (corresponding to $y_0/\delta = 0.08, 0.1, 0.13$ and 0.17). The streamwise position of the reference point (x_0) of the APG case is located at the reference streamwise position ($Re_\theta = 7240$) and corresponding to $Re_\theta = 2068$ for the case of ZPG TBL. Unfortunately, it was not possible to compare the two cases with the equivalent Reynolds number as these statistics require a large database of raw 3D velocity fields that was not available at a larger Reynolds number for ZPG. Even in presence of this difference in terms of Reynolds numbers, the investigation of the APG effects on the large-scale motions is still possible as the effect of pressure gradient on LSM is more important than those of Reynolds number and the latter has a large effect on the extent of structures. Contours levels correspond to iso-values from 0.1 to 0.9 of the correlation function normalized by the corresponding streamwise Reynolds stress at the reference point $u(x_0, y_0)$. The calculation of the two-point correlation function was performed in a domain extending up to the boundary layer thickness in the normal direction and around six local boundary layer thicknesses centered at the reference position in the streamwise direction.

From the comparison between the APG and ZPG correlation functions, one can notice that large-scale motions in the APG case are more inclined upstream than those in the ZPG case. The angle of inclination relative to the wall was found to be around 8° for the ZPG case and 15° for the TBL subjected to an APG. Kitsios et al. [67] have compared the two-point correlations from DNS of ZPG and APG TBLs. They found that the inclination of the major axis of the elliptical shape of these streamwise structures has an approximate angle of 7° for the ZPG case, 14° for the mild APG, and 27° for the strong APG TBL. The inclination angle seems to be constant for the four wall-normal reference positions shown in Fig. 5.2. The exact determination of this angle is however difficult as the two-point correlation functions are not extremely well converged.

The extend of the low isovalues of the two-point correlation function is associated with the large-scale motions. According to the comparison of Fig. 5.2, the largest scale structures scaled with δ extend more downstream for the APG case than for the ZPG one. By comparing the results at different wall-normal positions, we notice that the forward part of the elliptical shape clearly reduces as moving away from the wall in APG TBL contrary to the ZPG case for which the forward part remains

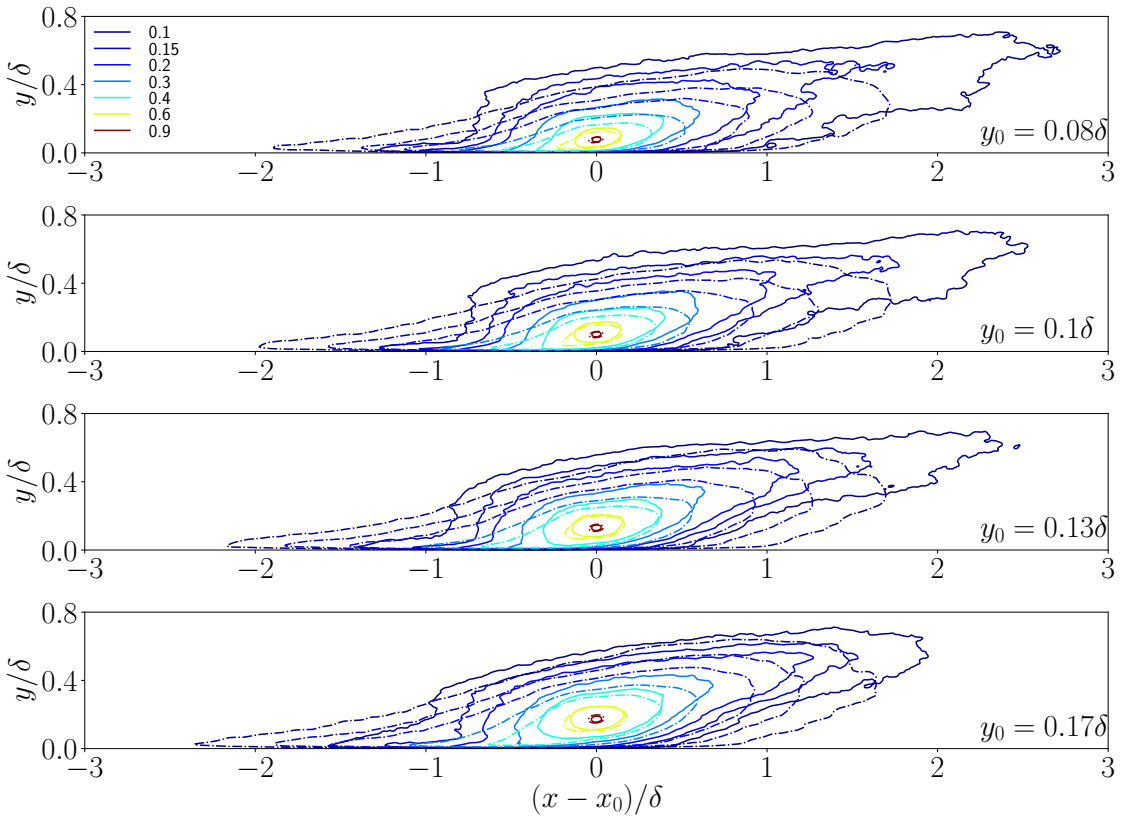

Fig. 5.2. Comparison of the iso-contours of the two-point correlation function plotted as function of boundary layer thickness δ between the APG case at $Re_\theta = 7240$ ($x_0 = 0.79L_x$) and the ZPG case at $Re_\theta = 2068$. The correlation is average over 211 (respectively 700) times and 1280 (respectively 448) points in the spanwise direction for the APG (respectively ZPG) cases. $y_0/\delta = 0.08$, 0.1, 0.13, 0.17 from top to bottom respectively.

at almost the same extent for all positions. This indicates that the upstream part of the large-scale motions seems to be modified under the effect of APG. The tail observed in the near-wall region backward of the fixed point (x_0, y_0) is associated with the near-wall low- and high-speed streaks. In ZPG case, the extent of the tail increases from -1.8δ to -2.4δ as moving upstream. However, in the APG case, the extent slowly increases from -1.3δ to -1.6δ.

On the other hand, an important difference between both cases is observed near the end of the tail, where a steep junction is visible between the inner and outer regions only in the APG case. This junction is probably responsible for the reduction of the tail extent in APG TBL. It is however important to point out again that the results of ZPG and APG are reported at different Reynolds numbers and this could explain part of the differences between the two correlation functions.

In order to focus on the steep junction in the inner region, the two-point correlation contours were plotted using the wall-unit scaling in Fig. 5.4, as it is not relevant

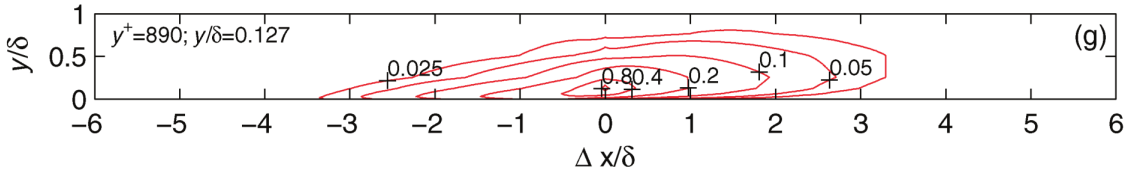

Fig. 5.3. Iso-contours of the two-point correlation (XY-plane). The reference point is located at $Re_\theta = 19100$ and its wall distance $y = 0.127\delta$ corresponding to $y^+ = 890$. (Reproduced from Tutkun et al. [153]).

to analyze the near-wall region using outer units. The present results show almost the same behavior of the steep departure from the near-wall region observed when the contours are scaled by δ.

In order to address this point, our results can be compared with the two-point correlations computed by Tutkun et al. [153] from HW rake measurements in the boundary layer wind tunnel of Lille at Reynolds number $Re_\theta = 19100$. When comparing the iso-value 0.1 in the contours of the two-point correlation reproduced in Fig. 5.3 at $y_0 = 0.127\delta$ (which is close to our results at 0.13δ) the iso-contour extend up to less then 2δ downstream. This is slightly more than for our reference ZPG case at a lower Reynolds number but much less than the corresponding APG case. This means that the effect of the Reynolds number is not enough to explain the difference between our ZPG and APG cases.

The near-wall region ($y^+ < 100$) of the two-point correlations is directly associated with the property of the near-wall streaks. One can see from Fig. 5.4 that the scaling of the streaks differ from the ZPG case. The upstream part is slightly longer in the APG case for the fix point at 50^+ and slightly shorter for $y_0 = 150^+$. The downstream part is harder to analyze as there is no sharp transition between the near-wall streaks and the outer large-scale structures.

As mentioned before the two-point correlations reflect the average statistics of the length and height of large-scale structures. Moreover, 3D representation of the correlations function can represent the width of structures, like in Sillero et al. [132]. In order to focus on the width of large-scale structures, the two-point correlation was calculated in the wall-normal spanwise plane. In Fig. 5.5, the two-point correlations scaled by δ are presented at two wall-normal distances ($y_0 = 0.08\delta$ and 0.17δ) for the same streamwise reference positions than the one used for the streamwise normal plane analysis. The structures in the APG case appear to be slightly larger than the ZPG ones at a reference position located in the upper part of the inner layer ($y_0 = 0.08\delta$), however, in the outer layer ($y_0 = 0.17\delta$) the contours in both cases present a similar extent in spanwise and wall-normal directions. The average spanwise width of the structures is around 0.4δ with small changes with the wall-

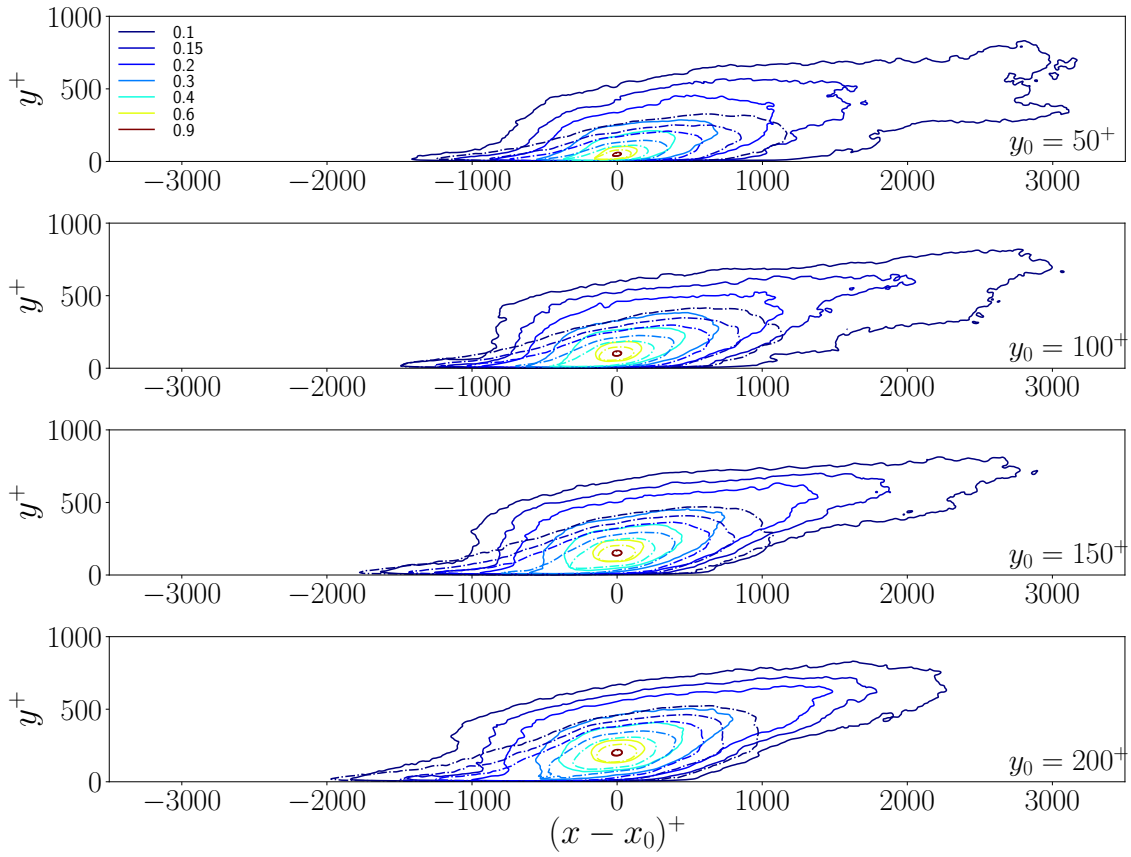

Fig. 5.4. Comparison of the iso-contours of the two-point correlation function plotted in wall-units between the APG case at $Re_\theta = 7240$ ($x_0 = 0.79L_x$) and the ZPG case at $Re_\theta = 2068$. The correlation is average over 211 (respectively 700) times and 1280 (respectively 448) points in the spanwise direction for the APG (respectively ZPG) cases. $y_0^+ = 50$, 100, 150, 200 from top to bottom respectively.

normal distances and the height of APG structures extended from 0.5δ to 0.6δ and from 0.4δ to 0.5δ in the ZPG case. Despite these small differences, the structures can be considered to have almost the same extent in the spanwise and wall-normal directions when an outer scaling is used. On the other hand, the structures in ZPG present an elliptical shape at all wall distances but, in APG case, a square shape near the wall is observed especially at $y_0 = 0.17\delta$.

In Fig. 5.6, the same correlation contours are presented using the wall-unit scaling. As expected, a significant difference in the structures dimensions is observed when using the wall-unit scaling as the corresponding Reynolds numbers are not comparable. The width of APG structures extended up to 400^+ but it still limited to 250^+ in the ZPG case.

To conclude, the streamwise large-scale structures scaled by outer units are slightly longer in the APG case as compare to ZPG and this can not be only explained by the difference of Reynolds number. Moreover, the structure is more

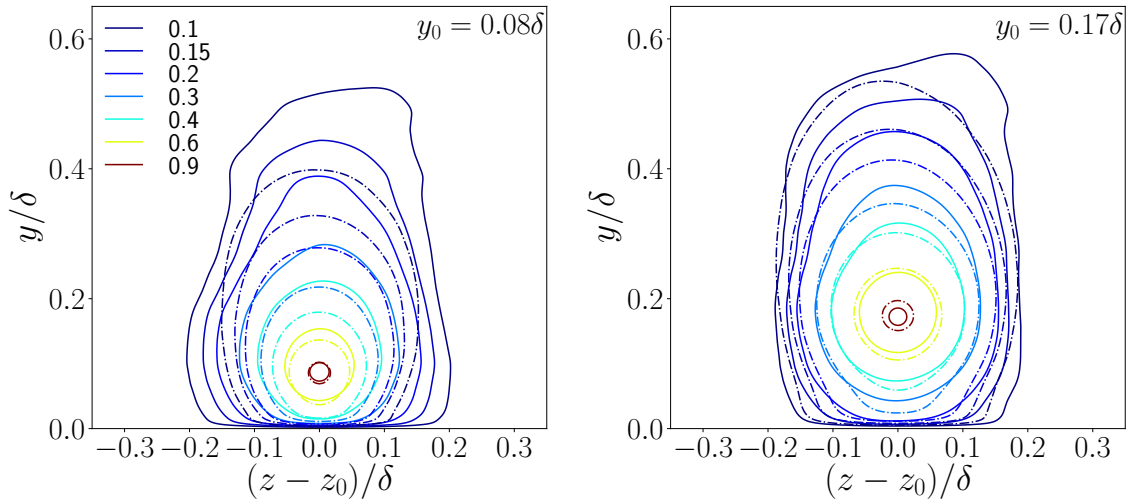

Fig. 5.5. Outer scaling two-points correlation in wall-normal-spanwise plane. APG case: $x_0 = 0.79L_x$; it is averaged over 1315 fields and 240 points in streamwise direction ($\sim \delta$). ZPG case: $x_0 = 0.75L_x$; it is averaged over 700 fields and 60 points in streamwise direction ($\sim 0.7\delta$).

inclined downstream in the APG case. However, the main difference is noticed in the upstream part of the structure just above the buffer region where the shape of the correlation function is quite different which seems to indicate a stronger impact of the large structures on the wall.

5.3 Detection methods

In order to further investigate the large-scale motion, the coherent structures of streamwise fluctuating velocity have been detected separately in space. The detection of structures individually allows the analysis of their characteristics and the contribution of small and large scales on turbulence statistics.

As the shape of the large-scale streamwise structures is complex, it is required to use a precise method to identify and detect individually these structures. Different methods have been proposed for such detection. Solak and Laval [140] used a simple thresholding technique to detect the structures of the streamwise velocity fluctuation where the threshold was chosen as the standard deviation of streamwise velocity fluctuation at $y^+ = 100$ to retain a large fraction of the kinetic energy. Yoon et al. [169] detected the same type of coherent structures from a DNS of APG TBL ($\beta = 1.43$) using a threshold variable with the wall-normal distance. Other methods have been used in the literature to detect different types of coherent structures [4, 12]. In the current study, we chose the same method as in Solak and Laval [140] in order to compare the results and to try to extract the effect of an adverse pressure

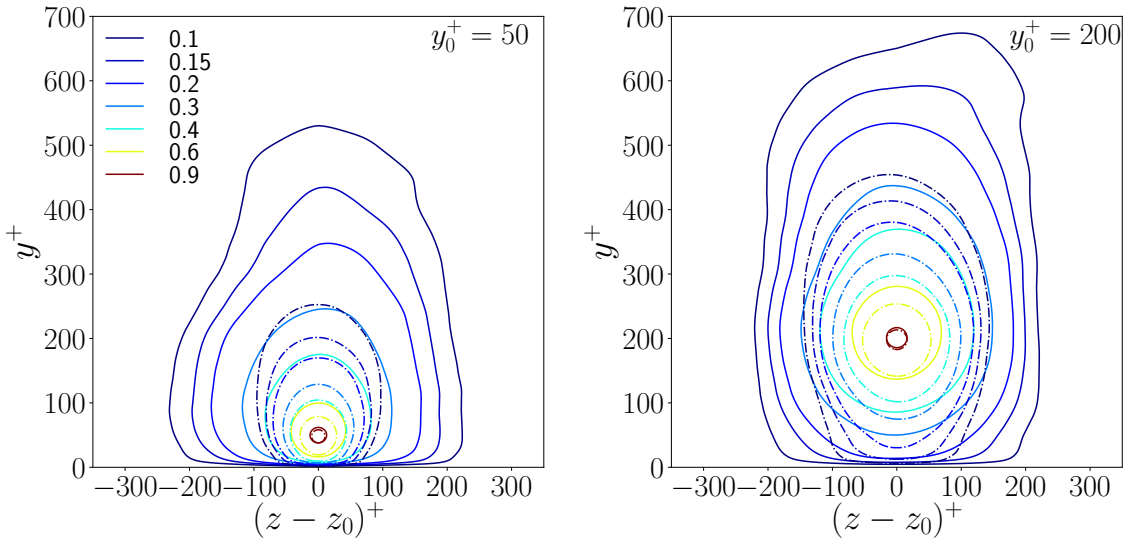

Fig. 5.6. Wall unit scaling two-points correlation in wall-normal-spanwise plane. APG case: $x_0 = 0.79L_x$; it is averaged over 1315 fields and 240 points in streamwise direction ($\sim \delta$). ZPG case: $x_0 = 0.75L_x$; it is averaged over 700 fields and 60 points in streamwise direction ($\sim 0.7\delta$).

gradient.

As a first step, 3D binary images of negative and positive streamwise fluctuations are obtained by applying a threshold on each field of streamwise velocity fluctuation. The formulation can be summarized as

$$B^{\ominus} = \begin{cases} 1 \text{ if } u < -C_{thr}\sigma_u^{100^+} \\ 0 \text{ otherwise} \end{cases} \tag{5.2}$$

$$B^{\oplus} = \begin{cases} 1 \text{ if } u > C_{thr}\sigma_u^{100^+} \\ 0 \text{ otherwise} \end{cases} \tag{5.3}$$

where $\sigma_u^{100^+}$ is the standard deviation of the streamwise velocity fluctuations at wall-normal position $y^+ = 100$, and C_{thr} is a constant threshold parameter.

The same reference velocity $\sigma_u^{100^+}$ have been used as in the ZPG case of Solak and Laval [140]. In the ZPG case, $y^+ = 100$ corresponds approximately to the beginning of the plateau or the smooth peak which is observed in the outer region of the boundary layer at high Reynolds numbers. As this outer peak is associated with the large-scale structures under investigation, taking the standard deviation of the streamwise velocity fluctuation at this position seems logical to take into account the effect of the Reynolds number.

When looking at the effect of the threshold, the results seem much closer to the ZPG case for the lower threshold when a large fraction of the volume is retained

as part of the structures. However, the results differ when detecting the structures with a higher threshold (close to 30% more volume, momentum and kinetic energy). These results seem to indicate that the streamwise velocity structures in the APG case contain larger values of streamwise velocity fluctuations. However, the results show that the percentage is quite sensible to the threshold value. It is therefore risky to draw quantitative conclusions about the proportion of momentum and energy carried by these structures.

In our APG case, by referring to Fig. 4.2a it is clearly noticed that the $\sigma_u^{100^+}$ do not has a significant change in the corresponding domain ($6818 < Re_\theta < 7582$). Moreover, the corresponding threshold is located at the crest between the inner and outer peaks of the streamwise velocity fluctuation and it is always smaller than the intensity of the outer peak which is widely related to the large-scale motion. However, the location of the standard deviation used in the binary images ($B^\ominus$ and $B^\oplus$) does not have a large effect on the statistics as using of $\sigma_u^{150^+}$ or $\sigma_u^{200^+}$ instead of $\sigma_u^{100^+}$ in (5.2) and (5.3) can change the percentages of the retained fractions of energy, momentum and volume for a maximum of 4%.

In order to see the sensitivity of the results as a function of the threshold value, the investigation was performed with three constant C_{thr} (0.5, 1 and 1.5). The percentages of the retained energy, momentum and volume fractions with different thresholds are given in Table 5.1 and compared with the same quantities in the ZPG TBL of Solak and Laval [140]. By comparing the statistics of ZPG and APG of the three quantities in the detected structures, it is noticed that the percentages in APG are always larger than those of ZPG as expected from the large outer peak of the Reynolds stress profiles.

Table 5.1. Streamwise energy, momentum and volume fraction inside the detected structures $B^\ominus$ and $B^\oplus$ from eq. (5.2) and (5.3) in APG and ZPG cases. Three threshold parameters C_{thr} are compared using the same reference standard deviation $\sigma_u^{100^+}$.

C_{thr}	Case	Energy			Momentum			Volume		
		$\oplus$	$\ominus$	$\oplus \cup \ominus$	$\oplus$	$\ominus$	$\oplus \cup \ominus$	$\oplus$	$\ominus$	$\oplus \cup \ominus$
0.5	ZPG	44%	52%	96%	41%	44%	85%	28%	27%	55%
	APG	47%	50%	97%	44%	45%	89%	30%	30%	60%
1.0	ZPG	34%	43%	77%	26%	31%	57%	13%	14%	27%
	APG	43%	41%	84%	33%	31%	64%	13%	12%	25%
1.5	ZPG	20%	30%	50%	12%	17%	29%	5%	6%	11%
	APG	28%	29%	57%	18%	19%	37%	8%	8%	16%

To go further away from the percentages of the full domain, a similar investigation using the same detection algorithm was performed to obtain the contribution

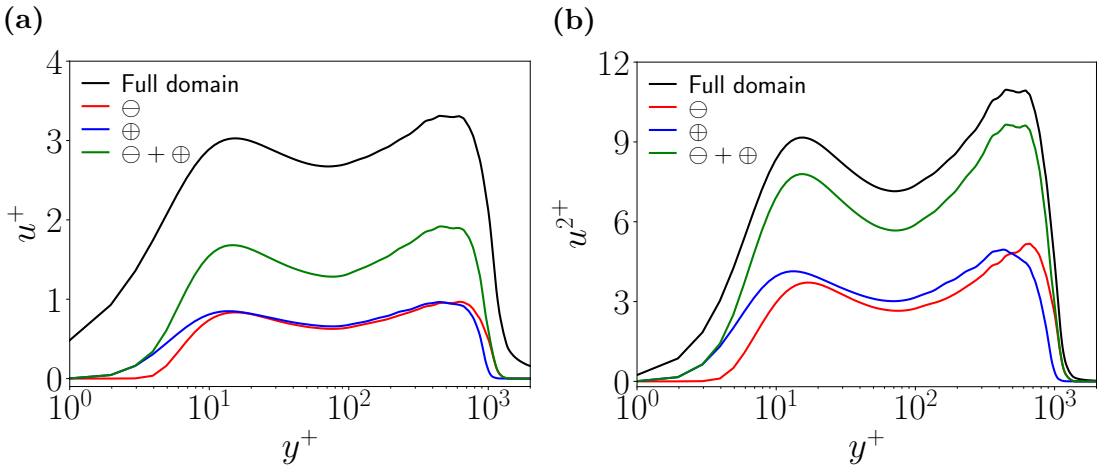

Fig. 5.7. Retained fraction of streamwise (a) momentum and (b) energy in wall-units after the thresholding process (5.2) and (5.3) as a function of wall distance. $\ominus$ corresponding to the fraction retained of $B^{\ominus}$ and $\oplus$ for $B^{\oplus}$. Black line represents the corresponding quantity for the whole domain.

of structures as a function of wall distance. In Fig. 5.7, we show the retained momentum and energy corresponding to $B^{\ominus}$ and $B^{\oplus}$ along the boundary layer in comparison with the corresponding profiles of the total streamwise turbulent intensity. Both figures show that the thresholding procedure retains a fraction of the momentum and the energy which is almost constant in y. Moreover, both negative and positive streamwise velocity profiles present similar values with a small change in shape. However, in Fig. 5.7b, a small shift toward larger y^+ appeared between the energy profiles of positive and negative fluctuations. This is due to the main effects of sweeps and ejections events as the sweeps (corresponding to $B^{\oplus}$) affect the momentum closer to the wall and the ejection linked to low-speed structures transfer momentum toward the top of the boundary layer. This observation is in agreement with the results of Ganapathisubramani et al. [39] where an analysis of the small-scale streamwise velocity fluctuations conditioned on high- and low-momentum shows that low-speed quantities dominate the high-speed ones far from the wall.

In order to have a qualitative view on the coherent structures, instantaneous three-dimensional iso-surface of the streamwise velocity fluctuations are shown in Fig. 5.8 at six different times. The time spacing between these consecutive observations is $\Delta t^+ = 180$ which corresponds to $\Delta t \frac{U_e}{\delta} = 5.6$ using outer quantities evaluated in the middle of the displayed domain. As the streamwise velocity fluctuation has an important change along the boundary layer, it is not efficient to use a constant threshold to observe the coherent structures. For that purpose, a variable threshold

has been used to retain fluctuations such as $|u| > u_{thr}(y^+)$ with u_{thr} defined as

$$u_{thr}(y^+) = \begin{cases} 2\sigma_u^{5^+} & \text{for } y^+ < 5 \\ 2\sigma_u^{y^+} & \text{for } 5 < y^+ < 500 \\ 2\sigma_u^{500^+} & \text{for } y^+ > 500 \end{cases} \tag{5.4}$$

This threshold is chosen to be suitable for illustrating coherent structures throughout the whole boundary layer. Negative fluctuations are represented by the orange color and the blue color has been used for positive ones. One can see that there are many very small structures, which indicates the importance of discarding them during the investigation of large-scale structures as they may have a not negligible contribution to the statistics. Large-scale structures that extend to the outer region are prominent. In agreement with the previous observation in Fig. 5.7b, one can easily see that the near-wall region is more populated by positive fluctuations and that the negative ones are mostly located in the upper part of the outer region. On the other hand, continuous observation of these structures using all database fields shows that the current database is sufficiently resolved to study and track the temporal coherent structures' motion since the time spacing between two consecutive velocity fields is of the order of a wall-unit time.

The previous statistics have been computed with all points of $B^{\ominus}$ and $B^{\oplus}$ obtained after the thresholding procedure. Therefore, the binary images also include small structures. In order to extract detailed statistics of individual structures, a new detection method is applied.

The inner peak that appears in the streamwise velocity fluctuation can affect the statistics of the structures because its intensity is larger than the threshold used in the detection and then the near-wall streaks will be detected. For this purpose, the detection of the structures was performed in a region starting from 20^+ which allows to focus on the highly energetic structures located in the logarithmic and outer regions.

After removing the near-wall region ($y^+ < 20$) a labeling procedure was applied on the binary images ($B^{\ominus}$ and $B^{\oplus}$) where the neighbor grid points connected by a simple connection in the orthogonal direction are regrouped in a single structure. Then, the geometrical information (location and dimensions of the bounding box) which contains the structures and Reynolds stress statistics are calculated for each structure. Since we are interested in the large-scale structures, the very small structures of a streamwise length $\lambda_x < 0.1\delta$ are discarded. This procedure is useful to reduce the number of detected structures and then to avoid the influence of the small-scale structures on the statistics of larger ones. Moreover, our interest is dedicated to the structures attached to the wall, however, as the fluctuations go to zero

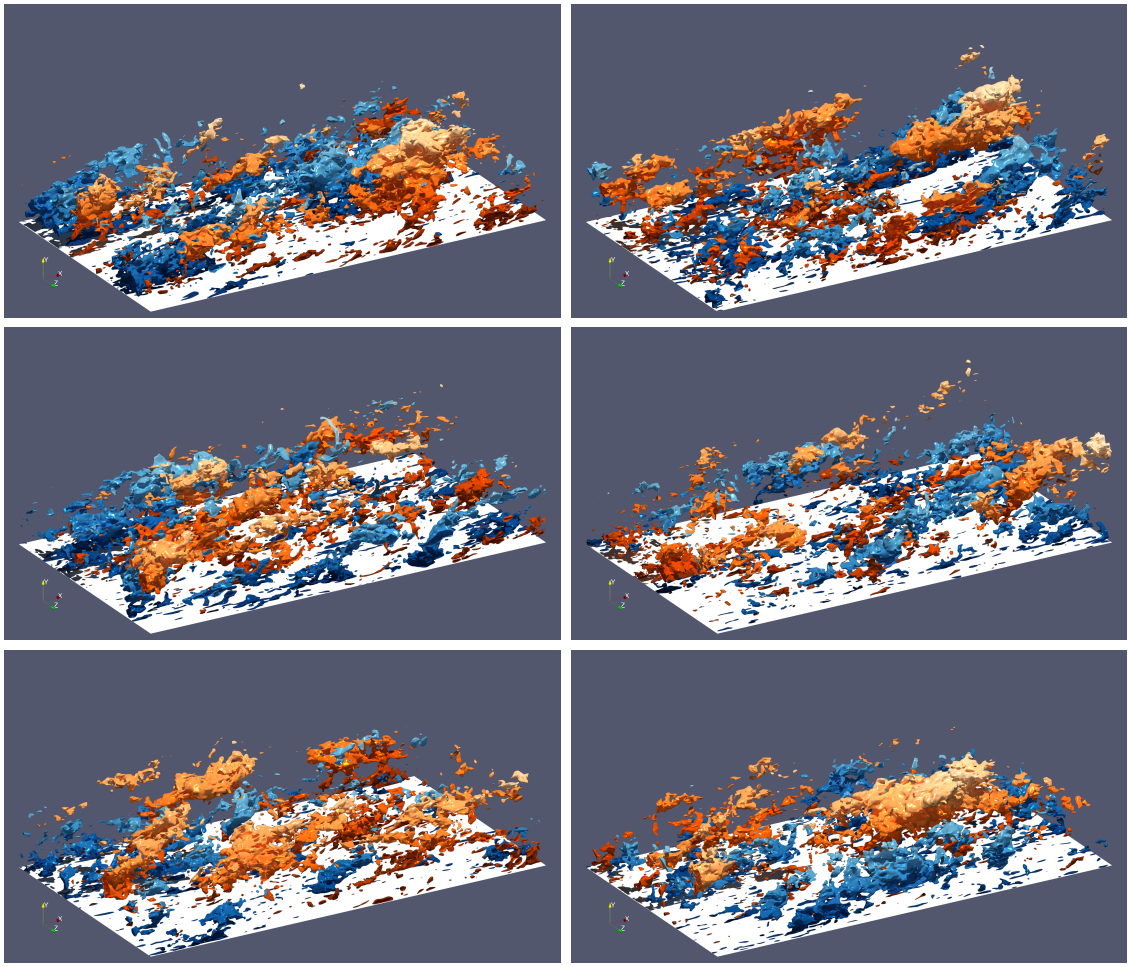

Fig. 5.8. Instantaneous iso-surface of the streamwise velocity fluctuations evaluated at 6 different times almost decorrelated (separated by $\Delta t^+ = 180$) on a small domain $6818 < Re_\theta < 7582$. Orange iso-surfaces correspond to low-speed motions and blue ones to high speed ones.

at the wall, it will be impossible to detect such structures close to the wall with the applied threshold. Furthermore, in order to keep only the attached structures, all structures with minimum wall distance $y_{min} > 50^+$ are discarded. After all these steps, the retained structures are saved in a hierarchic file (HDF5 type) with the corresponding information. This file will be used to obtain different statistics on the location and extent of the structures and the relation between the dimensions of structures. Moreover, during the detection process, the binary volume corresponding to a specific velocity field was saved where the structures are indexed based on their streamwise extent. In order to distinguish between the low and high momentum structures, negative indexes were used for the low speed and positives for the high ones. These binary volumes allow us to investigate the contribution of structures on various quantities, e.g., the Reynolds stresses, the production rate of turbulent kinetic energy, etc. taking into account the length scale of the considered structures.

5.4 Analysis of coherent structures

As a first statistic for the detection of coherent structures, we present a 2D probability density function of the streamwise and wall-normal dimensions of the detected structures, normalized by the boundary layer thickness δ evaluated at the middle of the detection domain (corresponding to $Re_\theta = 7240$). 2D PDF allows us to investigate the aspect ratio of the detected structures. The results of the low- and high-momentum structures of the current APG TBL were compared with those of the ZPG case already mentioned. In Fig. 5.9 the average height of the detected structures was presented as function of the streamwise extent. One can easily notice that many high-momentum structures (top figures) extended up to the top of the boundary layer in both cases but the low-momentum structures are limited to $0.3 - 0.4\delta$. It should be noted that the present analysis has been conducted on a domain which is 20δ long for the ZPG and only 5δ long for the APG. This explains why very long structures can not be observed in the APG case.

The aspect ratios of the high-speed attached structures show an important difference in presence of APG, where the average height of the structures represents 30% of the streamwise length instead of 15% in ZPG structures. This is in agreement with the previous results obtained with a two-point correlation which shows that the structures are more inclined. However, it seems to be similar for the low-momentum structures, where the height is around 10% of streamwise extent in both cases. Note that the structures appeared with a different aspect ratio with a height near δ and large streamwise length are corresponding to the very large-scale motions that are clearly shown in the ZPG case due to the large domain of detection. On the other hand, in addition to the restriction of the detection domain in the APG case, the 2D PDF are not extremely well converged, which leads to distorted contours, especially for the large-scale structures. However, the present results seem to show that there is no strong impact of the moderate APG on the low-momentum structures and the high-momentum ones become wider in presence of APG.

The two-dimensional PDF of the streamwise and spanwise dimensions of the coherent structures are shown in Fig. 5.10, normalized by δ. The average spanwise width seems to be 20% of the streamwise length for low-momentum structures in ZPG and APG cases like the ZPG high-momentum ones. However, the contours of the high-momentum structures of the APG case (even if they are not well converged) show that the spanwise width is closer to 30% of the streamwise length.

The present results show some similarities with those obtained in the Quadrant investigation of Lozano-Durán et al. [86]. Using data from the DNSs of turbulent channel flows of Del Álamo et al. [32] at $h^+ = 934$ and Hoyas and Jiménez [50] at $h^+ = 2003$, the shear stress structures were investigated and the streamwise extent

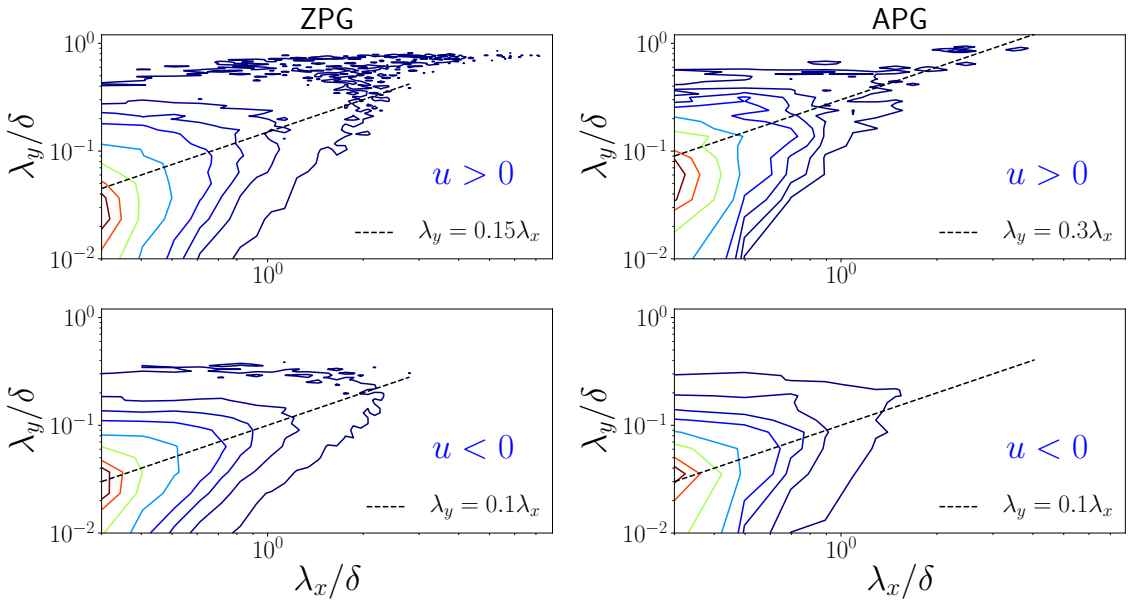

Fig. 5.9. Joint PDFs of streamwise wall-normal sizes $P(\lambda_x/\delta, \lambda_y/\delta)$ of the detected structures. Contour lines correspond to 90%, 75%, 50%, 25%, 10%, 5%, 2%, and 0.2% of the detected structures. An indicative ratio between the two sizes of the joint PDFs are given with dashed lines. Top figures correspond to high momentum structures and the lower for the low momentum. Left figures for the ZPG case and the APG case on the right.

of the ejection and sweep events λ_x seems to be approximately 3 times the height of the structures λ_y.

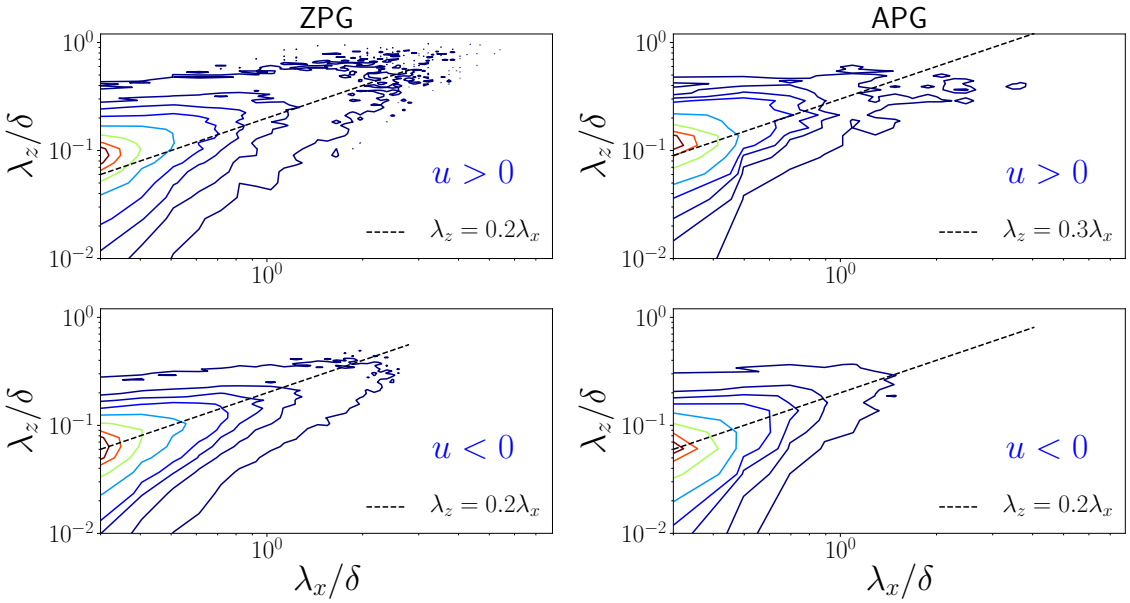

Fig. 5.10. Joint PDFs of streamwise spanwise size $P(\lambda_x/\delta, \lambda_z/\delta)$ of the detected structures. The percentages of the contours were used like as the previous figure with the same organization of sub-figures.

Chapter 6

Conclusions and perspectives

Wall-bounded turbulent flows have great theoretical, technological and environmental importance. Hence, they have received increasing attention in the last decades. Through the development and improvement of experimental and numerical techniques, turbulent flows at a wide range of Reynolds numbers have been investigated. These investigations have failed to solve many unsolved problems of wall turbulence, however, they provide new challenges and raise several new questions. This highlights the complexity of this topic and the importance of further numerical and experimental research. Furthermore, the majority of the research works have been conducted on canonical flows such as turbulent boundary layers with zero pressure gradient, where it was inevitable to start with these simple flows. On the other hand, it will be necessary to move towards more realistic flows since the canonical flow behavior does not reflect reality.

In that context, the present thesis aims to contribute to our understanding of the organization of non-canonical turbulent boundary layer flows and the effects of the adverse pressure gradient. Turbulent boundary layer flow subjected to a moderate APG was studied under external flow conditions similar to those found in the flows around a curved shape such as an airplane wing. The emphasis was on the outer region of the boundary layer in which the turbulent activity reaches its maximum.

Summary of findings

In the present work, a large database was collected from a DNS of turbulent boundary layer flows with a moderate adverse pressure gradient. The current database is well-resolved in time and space. 2D time-resolved database allows various temporal analyses on a single streamwise location and the 3D one leads to investigate the coherent structures in addition to many other statistics. A relatively high Reynolds number is achieved in this simulation in comparison with other DNSs subjected

to a moderate APG. Furthermore, the present turbulent boundary layer is out of equilibrium which makes this case interesting to test the universality of turbulence models proposed for equilibrium wall-bounded flows.

A detailed analysis of the logarithmic layer shows that the log-law proposed for this region in canonical flows does not match with the current mean streamwise velocity profiles. Even for the highest Reynolds number, the diagnostic plot for the log law does not develop a plateau but rather a peak moving from 50^+ to 80^+ as the Reynolds number increase. This peak is clearly more pronounced than for ZPG TBL at a similar Reynolds number indicating a stronger departure from a log law.

Several scalings have been tested but none of them seems to correctly scale the outer region of the mean velocity profiles on the full range of pressure gradient and Reynolds number. As already observed, the Zagarola and Smits scaling seems satisfactory in the limited range where the pressure gradient does not vary too much and far from the inlet with a sudden change of pressure gradient. The other scaling based on the position of an inflection point could not be fully conclusive as the data are not converged enough to predict with good accuracy the position of the most remote inflection point from the wall. Moreover, this inflection point would be very weak and may not be meaningful.

The Reynolds stress profiles exhibit an outer peak which is stronger than the inner peak. The position of these peaks evolves with the evolution of pressure gradient and Reynolds number. It has been shown that these outer peaks move away from the wall when scaled in boundary layer thickness or displacement thickness to start to stabilize near $1.3\delta_1$ and 0.45δ after a downstream evolution of at least 20 boundary layer thicknesses. These results seem in agreement with experimental results with a slightly different pressure gradient evolution and a much higher Reynolds number.

It is presumed that the outer peak of the Reynolds stresses is linked to an excess of turbulence kinetic energy production with respect to dissipation in the same region. This energy source, which is negligible for ZPG TBL at similar Reynolds numbers, seems to scale with the external velocity. This energy source is positive on a wide outer range from 0.2δ to 0.8δ centered on the position where the outer peak of Reynolds stresses is observed.

It has been shown that all Reynolds stress profiles can be scaled with the square root of the shear Reynolds stress u^* corresponding to the mean momentum flux. This finding extends the validity of these scaling proposed by Lozano-Duran in other categories of wall-bounded flows and seems to indicate that the outer peak of Reynolds stress involves coherent structures (large or small scales) with the same magnitude of velocity fluctuations.

Concerning the energy spectra, it was confirmed that the Townsend-Perry k^{-1}

range can be observed only for a single position from the wall near $y^+ = 35$. However, the limited Reynolds number and the difficulty to extract streamwise spectra as well as the limited convergence of the time spectra make a deeper analysis of the slope very difficult. However, it was possible to study the spanwise spectra which are less documented and which also exhibit a k^{-1} slope on a limited range. This consolidates the hypothesis of the presence of self-similar large-scale structures.

The investigation of the two-point correlation of streamwise fluctuating velocity indicated that the effect of the pressure gradient is to increase the size and lift up of these coherent structures as already observed in the literature. These correlations also revealed a different footprint and connection of these structures with the near-wall streaks. This difference with ZPG could not be fully understood and would require a deeper analysis.

Perspectives

Further studies can be proposed as future work focusing on the coherent structures using the current database. The contribution of coherent structures (low- and high-momentum) on the Reynolds stress terms in the presence of adverse pressure gradient could be investigated more deeply and be compared with the zero pressure gradient case. A comparison between the effects of small- and large-scale streamwise structures could also be examined.

In the present work, we focused on the streamwise structures but the scaling of the outer peak of all Reynolds stresses shows that the outer structures like the quadrants may also be as interesting.

Although the detection domain is not long enough to investigate the very long coherent structures, the good temporal resolution of the database allows us to study the development of the structures in time and to focus on how they are created and evolve. Moreover, the simulation and the created database have been designed to be able to extend the simulation in the streamwise direction if needed. Several time-resolved planes have been recorded at 3 streamwise positions and could be used as inlet conditions for new simulation with increasing the Reynolds numbers with the possibility to modify the pressure gradient. The present simulation has shown that the strategy is possible and adapted to simulate turbulent boundary layers at a fairly large Reynolds number.

A comparison with experimental results for a comparable adverse pressure gradient at a higher Reynolds number does not allow to distinguish clearly between the effect of Reynolds number and that of the adverse pressure gradient, because the history and evolution of both adverse pressure gradients are not similar. There-

fore, additional studies which cover a wider range in terms of Reynolds number, are needed to be able to distinguish between both effects.

The high spatial resolution of the generated databases allows one to design very different analyses of the turbulence. The present work has been focused on the statistics but it would be interesting to investigate more the energy transfer using for instance the Kármán-Howarth equations for the velocity increments which requires a large database of very well resolved DNS data. The LMFL team already has a strong experience with using this type of analysis on non-homogeneous turbulence of channel flows [170].

References

[1] L. I. Abreu, A. V. G. Cavalieri, P. Schlatter, R. Vinuesa, and D. S. Henningson. "Spectral proper orthogonal decomposition and resolvent analysis of near-wall coherent structures in turbulent pipe flows". In: *Journal of Fluid Mechanics* 900 (2020), A11.

[2] R. J. Adrian, C. D. Meinhart, and C. D. Tomkins. "Vortex organization in the outer region of the turbulent boundary layer". In: *Journal of fluid Mechanics* 422 (2000), pp. 1–54.

[3] A. S. Almgren, J. B. Bell, and W. G. Szymczak. "A numerical method for the incompressible Navier-Stokes equations based on an approximate projection". In: *SIAM Journal on Scientific Computing* 17.2 (1996), pp. 358–369.

[4] M. Atzori, R. Vinuesa, A. Lozano-Durán, and P. Schlatter. "Coherent structures in turbulent boundary layers over an airfoil". In: *Journal of Physics: Conference Series*. Vol. 1522. 1. IOP Publishing. 2020, p. 012020.

[5] W. J. Baars, N. Hutchins, and I. Marušić. "Self-similarity of wall-attached turbulence in boundary layers". In: *Journal of Fluid Mechanics* 823 (2017).

[6] W. J. Baars and I. Marušić. "Data-driven decomposition of the streamwise turbulence kinetic energy in boundary layers. Part 1. Energy spectra". In: *Journal of Fluid Mechanics* 882 (2020).

[7] B. J. Balakumar and R. J. Adrian. "Large- and very-large-scale motions in channel and boundary-layer flows". In: *Philosophical Transactions of the Royal Society A: Mathematical, Physical and Engineering Sciences* 365.1852 (2007), pp. 665–681.

[8] B. Baldwin and T. Barth. "A one-equation turbulence transport model for high Reynolds number wall-bounded flows". In: *29th aerospace sciences meeting*. 1991, p. 610.

[9] L. H. Benedict and R. D. Gould. “Concerning time and length scale estimates made from burst-mode LDA autocorrelation measurements”. In: *Experiments in fluids* 24.3 (1998), pp. 246–253.

[10] R. F. Blackwelder and H. Eckelmann. “Streamwise vortices associated with the bursting phenomenon”. In: *Journal of Fluid Mechanics* 94 (1979), pp. 577–594.

[11] P. Bradshaw. “The turbulence structure of equilibrium boundary layers”. In: *Journal of Fluid Mechanics* 29.4 (1967), pp. 625–645.

[12] M. Bross, T. Fuchs, and C. J. Kähler. “Interaction of coherent flow structures in adverse pressure gradient turbulent boundary layers”. In: *Journal of Fluid Mechanics* 873 (2019), pp. 287–321.

[13] G. L. Brown and A. S. W. Thomas. “Large structure in a turbulent boundary layer”. In: *The Physics of fluids* 20.10 (1977), S243–S252.

[14] K. C. Brown and P. N. Joubert. “The measurement of skin friction in turbulent boundary layers with adverse pressure gradients”. In: *Journal of Fluid Mechanics* 35.4 (1969), pp. 737–757.

[15] J. Carlier and M. Stanislas. “Experimental study of eddy structures in a turbulent boundary layer using particle image velocimetry”. In: *Journal of Fluid Mechanics* 535 (2005), p. 143.

[16] L. Castillo and W. K. George. “Similarity analysis for turbulent boundary layer with pressure gradient: outer flow”. In: *AIAA journal* 39.1 (2001), pp. 41–47.

[17] L. Castillo and D. J. Walker. “Effect of Upstream Conditions on the Outer Flow of Turbulent Boundary Layers”. In: *AIAA Journal* 40.7 (2002), pp. 1292–1299.

[18] S. Catris and B. Aupoix. “Towards a calibration of the length-scale equation”. In: *International Journal of Heat and Fluid Flow* 21.5 (2000), pp. 606–613.

[19] M. S. Chong, A. E. Perry, and B. J. Cantwell. “A general classification of three-dimensional flow fields”. In: *Physics of Fluids A: Fluid Dynamics* 2.5 (1990), pp. 765–777.

[20] K. T. Christensen and R. J. Adrian. “Statistical evidence of hairpin vortex packets in wall turbulence”. In: *Journal of Fluid Mechanics* 431 (2001), pp. 433–443.

[21] A. Cimarelli, E. De Angelis, J. Jiménez, and C. M. Casciola. “Cascades and wall-normal fluxes in turbulent channel flows”. In: *Journal of Fluid Mechanics* 796 (2016), pp. 417–436.

[22] F. H. Clauser. “The turbulent boundary layer”. In: *Advances in applied mechanics*. Vol. 4. Elsevier, 1956, pp. 1–51.

[23] F. H. Clauser. “Turbulent boundary layers in adverse pressure gradients”. In: *Journal of Aeronautical Sciences* 21.2 (1954), pp. 91–108.

[24] D. Coles. “The law of the wake in the turbulent boundary layer”. In: *Journal of Fluid Mechanics* 1.2 (1956), pp. 191–226.

[25] G. Comte-Bellot. “Hot-wire anemometry”. In: *Annual review of fluid mechanics* 8.1 (1976), pp. 209–231.

[26] E. R. Corino and R. S. Brodkey. “A visual investigation of the wall region in turbulent flow”. In: *Journal of Fluid Mechanics* 37.1 (1969), pp. 1–30.

[27] S. Corrsin. *Local isotropy in turbulent shear flow*. Vol. 34. 58. National Advisory Committee for Aeronautics, 1958.

[28] T. Dairay, V. Fortuné, E. Lamballais, and L. E. Brizzi. “LES of a turbulent jet impinging on a heated wall using high-order numerical schemes”. In: *International Journal of Heat and Fluid Flow* 50 (2014), pp. 177–187.

[29] V. Dallas, J. C. Vassilicos, and G. F. Hewitt. “Stagnation point von Kármán coefficient”. In: *Physical Review E* 80.4 (2009), p. 046306.

[30] P. Debue, V. Valori, C. Cuvier, F. Daviaud, J.-M. Foucaut, J.-P. Laval, C. Wiertel, V. Padilla, and B. Dubrulle. “Three-dimensional analysis of precursors to non-viscous dissipation in an experimental turbulent flow”. In: *Journal of Fluid Mechanics* 914 (2021).

[31] J. C. Del Álamo and J. Jiménez. “Spectra of the very large anisotropic scales in turbulent channels”. In: *Physics of Fluids* 15.6 (2003), pp. L41–L44.

[32] J. C. Del Álamo, J. Jiménez, P. Zandonade, and R. D. Moser. “Scaling of the energy spectra of turbulent channels”. In: *Journal of Fluid Mechanics* 500 (2004), p. 135.

[33] D. J. C. Dennis and T. B. Nickels. “Experimental measurement of large-scale three-dimensional structures in a turbulent boundary layer. Part 1. Vortex packets”. In: *Journal of Fluid Mechanics* 673 (2011), pp. 180–217.

[34] C. Diaz-Daniel, S. Laizet, and J. C. Vassilicos. “Wall shear stress fluctuations: Mixed scaling and their effects on velocity fluctuations in a turbulent boundary layer”. In: *Physics of Fluids* 29.5 (2017), p. 055102.

[35] P. A. Durbin and S. E. Belcher. “Scaling of adverse-pressure-gradient turbulent boundary layers”. In: *Journal of Fluid Mechanics* 238 (1992), pp. 699–722.

[36] F. Eich, M. Bross, D. Schanz, M. Novara, A. Schröder, and C. J. Kähler. "Large field of view volumetric measurement of a turbulent boundary layer". In: *APS Division of Fluid Dynamics Meeting Abstracts*. APS Meeting Abstracts. 2019, P15.007.

[37] R. E. Falco. "Coherent motions in the outer region of turbulent boundary layers". In: *The Physics of Fluids* 20.10 (1977), S124–S132.

[38] M. Fortin, R. Peyret, and R. Temam. "Résolution numérique des équations de Navier-Stokes pour un fluide incompressible". In: *Journal de Mécanique* 10.3 (1971), pp. 357–390.

[39] B. Ganapathisubramani, N. Hutchins, J. P. Monty, H. Ng, and I. Marušić. "Near-wall influence of large-scale motions in high Reynolds number turbulent boundary layers". In: *Sixth International Symposium on Turbulence and Shear Flow Phenomena*. Begel House Inc. 2009.

[40] B. Ganapathisubramani, E. K. Longmire, and I. Marušić. "Characteristics of vortex packets in turbulent boundary layers". In: *Journal of Fluid Mechanics* 478 (2003), pp. 35–46.

[41] W. K. George. "Is there a universal log law for turbulent wall-bounded flows?" In: *Philosophical Transactions of the Royal Society A: Mathematical, Physical and Engineering Sciences* 365.1852 (2007), pp. 789–806.

[42] W. K. George and L. Castillo. "Zero-Pressure-Gradient Turbulent Boundary Layer". In: *Applied Mechanics Reviews* 50.12 (1997), pp. 689–729.

[43] W. K. George, M. Stanislas, and J.-P. Laval. "New insights into adverse pressure gradient boundary layers". In: *Progress in Turbulence and Wind Energy IV*. Springer, 2012, pp. 201–204.

[44] H. L. Grant. "The large eddies of turbulent motion". In: *Journal of Fluid Mechanics* 4.2 (1958), pp. 149–190.

[45] M. Guala, S. E. Hommema, and R. J. Adrian. "Large-scale and very-large-scale motions in turbulent pipe flow". In: *Journal of Fluid Mechanics* 554 (2006), pp. 521–542.

[46] A. G. Gungor, Y. Maciel, M. P. Simens, and J. Soria. "Analysis of a Turbulent Boundary Layer Subjected to a Strong Adverse Pressure Gradient". In: *1st Multiflow Summer Workshop*. Vol. 506. 012007. 2014, pp. 1–14.

[47] A. G. Gungor, Y. Maciel, M. P. Simens, and J. Soria. "Scaling and statistics of large-defect adverse pressure gradient turbulent boundary layers". In: *International Journal of Heat and Fluid Flow* 59 (2016), pp. 109–124.

[48] X. Han, T. Wray, and R. K. Agarwal. “Application of a new DES model based on wray-agarwal turbulence model for simulation of wall-bounded flows with separation”. In: *47th AIAA Fluid Dynamics Conference*. 2017, p. 3966.

[49] M. R. Head and P. Bandyopadhyay. “New aspects of turbulent boundary-layer structure”. In: *Journal of fluid mechanics* 107 (1981), pp. 297–338.

[50] S. Hoyas and J. Jiménez. “Scaling of the velocity fluctuations in turbulent channels up to $Re_\tau = 2003$”. In: *Physics of fluids* 18.1 (2006), p. 011702.

[51] P. G. Huang and P. Bradshaw. “Law of the wall for turbulent flows in pressure gradients”. In: *AIAA journal* 33.4 (1995), pp. 624–632.

[52] M. Hultmark, M. Vallikivi, S. C. C. Bailey, and A. J. Smits. “Turbulent pipe flow at extreme Reynolds numbers”. In: *Physical review letters* 108.9 (2012), p. 094501.

[53] J. C. R. Hunt, A. A. Wray, and P. Moin. “Eddies, streams, and convergence zones in turbulent flows”. In: *Summer Program of the Center for Turbulence Research* (1988), pp. 193–207.

[54] N. Hutchins, K. Chauhan, I. Marušić, J. Monty, and J. Klewicki. “Towards reconciling the large-scale structure of turbulent boundary layers in the atmosphere and laboratory”. In: *Boundary-layer meteorology* 145.2 (2012), pp. 273–306.

[55] N. Hutchins and I. Marušić. “Evidence of very long meandering features in the logarithmic region of turbulent boundary layers”. In: *Journal of Fluid Mechanics* 579 (2007), pp. 1–28.

[56] J. Hwang, J. Lee, H. J. Sung, and T. A. Zaki. “Inner-outer interactions of large-scale structures in turbulent channel flow”. In: *Journal of Fluid Mechanics* 790 (2016), pp. 128–157.

[57] J. Jiménez. “Near-wall turbulence”. In: *Physics of Fluids* 25.10 (2013), p. 101302.

[58] J. Jiménez, J. C. Del Álamo, and O. Flores. “The large-scale dynamics of near-wall turbulence”. In: *Journal of Fluid Mechanics* 505 (2004), pp. 179–199.

[59] J. Jiménez and S. Hoyas. “Turbulent fluctuations above the buffer layer of wall-bounded flows”. In: *Journal of Fluid Mechanics* 611 (2008), pp. 215–236.

[60] J. Jiménez, S. Hoyas, M. P. Simens, and Y. Mizuno. “Turbulent boundary layers and channels at moderate Reynolds numbers”. In: *Journal of Fluid Mechanics* 567 (2010), pp. 335–360.

[61] J. Jiménez and P. Moin. “The minimal flow unit in near-wall turbulence”. In: *Journal of Fluid Mechanics* 225 (1991), pp. 213–240.

[62] C. J. Kähler. “Investigation of the spatio-temporal flow structure in the buffer region of a turbulent boundary layer by means of multiplane stereo PIV”. In: *Experiments in Fluids* 36.1 (2004), pp. 114–130.

[63] H. Kim, S. J. Kline, and W. C. Reynolds. “The production of turbulence near a smooth wall in a turbulent boundary layer”. In: *Journal of Fluid Mechanics* 50.1 (1971), pp. 133–160.

[64] J. Kim and P. Moin. “Application of a fractional-step method to incompressible Navier-Stokes equations”. In: *Journal of Computational Physics* 59.2 (1985), pp. 308–323.

[65] K. C. Kim and R. J. Adrian. “Very large-scale motion in the outer layer”. In: *Physics of Fluids* 11.2 (1999), pp. 417–422.

[66] V. Kitsios, C. Atkinson, J. A. Sillero, G. Borrell, A. G. Gungor, J. Jiménez, and J. Soria. “Direct numerical simulation of a self-similar adverse pressure gradient turbulent boundary layer”. In: *International Journal of Heat and Fluid Flow* 61 (2016), pp. 129–136.

[67] V. Kitsios, A. Sekimoto, C. Atkinson, J. A. Sillero, G. Borrell, A. G. Gungor, J. Jiménez, and J. Soria. “Direct numerical simulation of a self-similar adverse pressure gradient turbulent boundary layer at the verge of separation”. In: *Journal of Fluid Mechanics* 829 (2017), pp. 392–419.

[68] S. J. Kline, W. C. Reynolds, F. A. Schraub, and P. W. Runstadl. “The structures of turbulent boundary layers”. In: *Journal of Fluid Mechanics* 30.4 (1967), pp. 741–773.

[69] P.-Å. Krogstad and P. E. Skåre. “Influence of a strong adverse pressure gradient on the turbulent structure in a boundary layer”. In: *Physics of Fluids* 7.8 (1995), pp. 2014–2024.

[70] D. Küchemann. “Report on the IUTAM symposium on concentrated vortex motions in fluids”. In: *Journal of Fluid Mechanics* 21.1 (1965), pp. 1–20.

[71] S. Laizet and E. Lamballais. “High-order compact schemes for incompressible flows: a simple and efficient method with the quasi-spectral accuracy”. In: *Journal of computational physics* 228.15 (2009), pp. 5989–6015.

[72] S. Laizet and N. Li. “Incompact3d: A powerful tool to tackle turbulence problems with up to $O(10^5)$ computational cores”. In: *Internartional Journal for Numerical Methods in Fluids* 67.11 (2011), pp. 1735–1757.

[73] J. V. Larssen and W. J. Devenport. “On the generation of large-scale homogeneous turbulence”. In: *Experiments in fluids* 50.5 (2011), pp. 1207–1223.

[74] J.-P. Laval, M. Marquillie, and U. Ehrenstein. “On the relation between kinetic energy production in adverse-pressure gradient wall turbulence and streak instability”. In: *Journal of Turbulence* 13.21 (2012), pp. 1–19.

[75] J.-P. Laval, J. C. Vassilicos, J.-M. Foucaut, and M. Stanislas. “Comparison of turbulence profiles in high-Reynolds-number turbulent boundary layers and validation of a predictive model”. In: *Journal of Fluid Mechanics* 814 (2017).

[76] J. H. Lee. “Large-scale motions in turbulent boundary layers subjected to adverse pressure gradients”. In: *Journal of Fluid Mechanics* 810 (2017), pp. 323–361.

[77] J. H. Lee and H. J. Sung. “Comparison of very-large-scale motions of turbulent pipe and boundary layer simulations”. In: *Physics of Fluids* 25.4 (2013), p. 045103.

[78] J.-H. Lee and H. J. Sung. “Effects of an adverse pressure gradient on a turbulent boundary layer”. In: *International Journal of Heat and Fluid Flow* 29 (2008), pp. 568–578.

[79] J.-H. Lee and H. J. Sung. “Large scale structure of turbulent boundary layer subjected to an adverse pressure gradient”. In: *TSFP DIGITAL LIBRARY ONLINE*. Begel House Inc. 2009.

[80] Jin Lee, Jae Hwa Lee, Jung-Il Choi, and Hyung Jin Sung. “Spatial organization of large-and very-large-scale motions in a turbulent channel flow”. In: *Journal of fluid mechanics* 749 (2014), pp. 818–840.

[81] M. Lee and R. D. Moser. “Direct numerical simulation of turbulent channel flow up to $Re_\tau \approx 5200$”. In: *Journal of fluid mechanics* 774 (2015), pp. 395–415.

[82] Q. X. Lian. “A visual study of the coherent structure of the turbulent boundary layer in flow with adverse pressure gradient”. In: *Journal of Fluid Mechanics* 215 (1990), pp. 101–124.

[83] M. J. Lighthill. “Boundary layer theory”. In: *Laminar boundary layers* 46 (1963), p. 113.

[84] J. Lin, J.-P. Laval, J.-M. Foucaut, and M. Stanislas. “Quantitative characterization of coherent structures in the buffer layer of near-wall turbulence. Part 1: streaks”. In: *Experiments in Fluids* 45.6 (2008), pp. 999–1013.

[85] A. Lozano-Durán and H. J. Bae. “Characteristic scales of Townsend’s wall-attached eddies”. In: *Journal of Fluid Mechanics* 868 (2019), pp. 698–725.

[86] A. Lozano-Durán, O. Flores, and J. Jiménez. “The three-dimensional structure of momentum transfer in turbulent channels”. In: *Journal of Fluid Mechanics* 694 (2012), pp. 100–130.

[87] H. Ludwieg. “Instrument for measuring the wall shearing stress of turbulent boundary layers”. In: (1950).

[88] Y. Maciel, M. P. Simens, and A. G. Gungor. “Coherent structures in a non-equilibrium large-velocity-defect turbulent boundary layer”. In: *Flow, Turbulence and Combustion* 98.1 (2017), pp. 1–20.

[89] Y. Maciel, T. Wei, A. G. Gungor, and M. P. Simens. “Outer scales and parameters of adverse-pressure-gradient turbulent boundary layers”. In: *Journal of Fluid Mechanics* 844 (2018), pp. 5–35.

[90] M. Marquillie, U. Ehrenstein, J.-P. Laval, et al. “Instability of streaks in wall turbulence with adverse pressure gradient”. In: *Journal of Fluid Mechanics* 681.205-240 (2011), p. 30.

[91] I. Marušić, R. Mathis, and N. Hutchins. “Predictive model for wall-bounded turbulent flow”. In: *Science* 329.5988 (2010), pp. 193–196.

[92] R. Mathis, N. Hutchins, and I. Marušić. “Large-scale amplitude modulation of the small-scale structures in turbulent boundary layers”. In: *Journal of Fluid Mechanics* 628 (2009), pp. 311–337.

[93] B. J. McKeon and J. F. Morrison. “Asymptotic scaling in turbulent pipe flow”. In: *Philosophical Transactions of the Royal Society A: Mathematical, Physical and Engineering Sciences* 365.1852 (2007), pp. 771–787.

[94] G. L. Mellor. “The effects of pressure gradients on turbulent flow near a smooth wall”. In: *Journal of Fluid Mechanics* 24.2 (1966), pp. 255–274.

[95] G. L. Mellor and D. M. Gibson. “Equilibrium turbulent boundary layers”. In: *Journal of Fluid Mechanics* 24.2 (1966), pp. 225–253.

[96] J. P. Monty, Z. Harun, and I. Marušić. “A parametric study of adverse pressure gradient turbulent boundary layers”. In: *International Journal of Heat and Fluid Flow* 32.3 (2011), pp. 575–585.

[97] J. F. Morrison, B. J. McKeon, W. Jiang, and A. J. Smits. “Scaling of the streamwise velocity component in turbulent pipe flow”. In: *Journal of Fluid Mechanics* 508 (2004), pp. 99–131.

[98] Y. Na and P. Moin. “Direct numerical simulation of a separated turbulent boundary layer”. In: *Journal of Fluid Mechanics* 374 (1998), pp. 379–405.

[99] Y. Nagano, M. Tagawa, and T. Tsuji. “Effects of adverse pressure gradients on mean flows and turbulence statistics in a boundary layer”. In: *Turbulent Shear Flows 8*. Springer, 1993, pp. 7–21.

[100] Y. Nagano, T. Tsuji, and T. Houra. “Structure of turbulent boundary layer subjected to adverse pressure gradient”. In: *International Journal of Heat and Fluid Flow* 19.5 (1998), pp. 563–572.

[101] H. M. Nagib, K. A. Chauhan, and P. A. Monkewitz. “Approach to an asymptotic state for zero pressure gradient turbulent boundary layers”. In: *Philosophical Transactions of the Royal Society A: Mathematical, Physical and Engineering Sciences* 365.1852 (2007), pp. 755–770.

[102] H. Nagib, C. Christophorou, K. Chauhan, and P. Monkewitz. “The Wall Shear Stress in Zero-Pressure Gradient Turbulent Boundary Layers. Do We Know Enough?” In: *Presentation at Perryfest 2004* (2004).

[103] R. Narasimha and K. R. Sreenivasan. “Relaminarization in highly accelerated turbulent boundary layers”. In: *Journal of Fluid Mechanics* 61.3 (1973), pp. 417–447.

[104] R. Narasimha and K. R. Sreenivasan. “Relaminarization of fluid flows”. In: *Advances in applied mechanics*. Vol. 19. Elsevier, 1979, pp. 221–309.

[105] B. G. Newman. *Some contributions to the study of the turbulent boundary-layer near separation*. Department of Supply, Aeronautical Research Consultative Committee, 1951.

[106] T. B. Nickels. “Inner scaling for wall-bounded flows subject to large pressure gradients”. In: *Journal of Fluid Mechanics* 521 (2004), pp. 217–239.

[107] T. B. Nickels, I. Marušić, S. Hafez, and M. S. Chong. “Evidence of the k_1^{-1} law in a high-Reynolds-number turbulent boundary layer”. In: *Physical review letters* 95.7 (2005), p. 074501.

[108] T. B. Nickels, I. Marušić, S. Hafez, N. Hutchins, and M. S. Chong. “Some predictions of the attached eddy model for a high Reynolds number boundary layer”. In: *Philosophical Transactions of the Royal Society A: Mathematical, Physical and Engineering Sciences* 365.1852 (2007), pp. 807–822.

[109] J. Nordström, N. Nordin, and D. Henningson. “The fringe region technique and the Fourier method used in the direct numerical simulation of spatially evolving viscous flows”. In: *SIAM Journal on Scientific Computing* 20.4 (1999), pp. 1365–1393.

[110] A. E. Perry and M. S. Chong. “On the mechanism of wall turbulence”. In: *Journal of Fluid Mechanics* 119 (1982), pp. 173–217.

[111] A. E. Perry, S. Henbest, and M. S. Chong. “A theoretical and experimental study of wall turbulence”. In: *Journal of Fluid Mechanics* 165 (1986), pp. 163–199.

[112] A. E. Perry and I. Marušić. “A wall-wake model for the turbulence structure of boundary layers. Part 1. Extension of the attached eddy hypothesis”. In: *Journal of Fluid Mechanics* 298 (1995), pp. 361–388.

[113] S. B. Pope. *Turbulent flows*. 2001.

[114] M. M. Rahman, R. K. Agarwal, and T. Siikonen. “A modified one-equation turbulence model based on turbulent kinetic energy equation”. In: *54th AIAA Aerospace Sciences Meeting*. 2016, p. 1598.

[115] N. Renard and S. Deck. “On the scale-dependent turbulent convection velocity in a spatially developing flat plate turbulent boundary layer at Reynolds number $Re_\theta = 13000$”. In: *Journal of Fluid Mechanics* 775 (2015), pp. 105–148.

[116] O. Reynolds. “An experimental investigation of the circumstances which determine whether the motion of water shall be direct or sinuous, and of the law of resistance in parallel channels”. In: *Philosophical Transactions of the Royal society of London* 174 (1883), pp. 935–982.

[117] O. Reynolds. “On the dynamical theory of incompressible viscous fluids andthe determination of the criterion”. In: *Proceedings of the Royal Society of London* 56.336-339 (1894), pp. 40–45.

[118] S. K. Robinson. “Coherent motions in the turbulent boundary layer”. In: *Annual Review of Fluid Mechanics* 23.1 (1991), pp. 601–639.

[119] S. K. Robinson, S. J. Kline, and P. R. Spalart. “A review of quasi-coherent structures in a numerically simulated turbulent boundary layer”. In: *NASA STI/Recon Technical Report N* 90 (1989), p. 13723.

[120] J. C. Rotta. “On the theory of the turbulent boundary layer”. In: *NACA Technical Report 1344* (1953).

[121] J. C. Rotta. “Turbulent boundary layers in incompressible flow”. In: *Progress in Aerospace Sciences* 2.1 (1962), pp. 1–95.

[122] P. Sagaut. *Large eddy simulation for incompressible flows: an introduction*. Springer Science & Business Media, 2006.

[123] A. E. Samuel and P. N. Joubert. “A boundary layer developing in an increasingly adverse pressure gradient”. In: *Journal of Fluid Mechanics* 66.3 (1974), pp. 481–505.

[124] D. M. Schatzman and F. O. Thomas. “An experimental investigation of an unsteady adverse pressure gradient turbulent boundary layer: embedded shear layer scaling”. In: *Journal of Fluid Mechanics* 815 (2017), pp. 592–642.

[125] P. Schlatter, Q. Li, G. Brethouwer, A. V. Johansson, and D. S. Henningson. “Simulations of spatially evolving turbulent boundary layers up to $Re_\theta = 4300$”. In: *International Journal of Heat and Fluid Flow* 31.3 (2010). Sixth International Symposium on Turbulence and Shear Flow Phenomena, pp. 251–261.

[126] P. Schlatter and R. Örlü. “Turbulent boundary layers at moderate Reynolds numbers: inflow length and tripping effects”. In: *Journal of Fluid Mechanics* 710 (2012), pp. 5–34.

[127] H. Schlichting and K. Gestern. *Boundary Layer Theory*. Springer Verlag, 1999.

[128] W. Schoppa and F. Hussain. “Coherent structure generation in near wall turbulence”. In: *Journal of Fluid Mechanics* 453 (2002), pp. 57–108.

[129] A. Sekimoto, V. Kitsios, C. Atkinson, and J. Soria. “Outer scaling of self-similar adverse-pressure-gradient turbulent boundary layers”. In: *arXiv preprint arXiv:1912.05143* (2019).

[130] S.-I. Shah, J.-P. Laval, and M. Stanislas. “A specific behaviour of adverse pressure gradient near wall flows”. In: *Progress in wall turbulence: understanding and modeling*. Springer, 2011, pp. 257–265.

[131] J. A. Sillero, J. Jiménez, and R. D. Moser. “One-point statistics for turbulent wall-bounded flows at Reynolds numbers up to $\delta^+ \approx 2000$”. In: *Physics of Fluids* 25.10 (2013), p. 105102.

[132] J. A. Sillero, J. Jiménez, and R. D. Moser. “Two-point statistics for turbulent boundary layers and channels at Reynolds numbers up to $\delta^+ \approx 2000$”. In: *Physics of Fluids* 26.10 (2014), p. 105109.

[133] C. M. de Silva, N. Hutchins, and I. Marusic. “Uniform momentum zones in turbulent boundary layers”. In: *Journal of Fluid Mechanics* 786 (2016), pp. 309–331.

[134] P. E. Skåre and P.-Å. Krogstad. “A turbulent equilibrium boundary layer near separation”. In: *Journal of Fluid Mechanics* 272 (1994), pp. 319–348.

[135] M. Skote and D. S. Henningson. “Direct numerical simulation of a separated turbulent boundary layer”. In: *Journal of Fluid Mechanics* 471 (2002), pp. 107–136.

[136] M. Skote, D. S. Henningson, and R. A. W. M. Henkes. "Direct Numerical Simulation of Self-Similar Turbulent Boundary Layers in Adverse Pressure Gradients". In: *Flow, Turbulence and Combustion* 60.1 (1998), pp. 47–85.

[137] C. R. Smith and S. P. Metzler. "The characteristics of low-speed streaks in the near-wall region of a turbulent boundary layer". In: *Journal of Fluid Mechanics* 129.1 (1983), pp. 27–54.

[138] C. R. Smith, J. D. A. Walker, A. H. Haidari, and U. Sobrun. "On the dynamics of near-wall turbulence". In: *Philosophical Transactions of the Royal Society of London. Series A: Physical and Engineering Sciences* 336.1641 (1991), pp. 131–175.

[139] A. J. Smits, B. J. McKeon, and I. Marušić. "High-Reynolds number wall turbulence". In: *Annual Review of Fluid Mechanics* 43 (2011), pp. 353–375.

[140] I. Solak and J.-P. Laval. "Large-scale motions from a direct numerical simulation of a turbulent boundary layer". In: *Physical Review E* 98 (2018), p. 033101.

[141] P. R. Spalart. "Detached-eddy simulation". In: *Annual review of fluid mechanics* 41 (2009), pp. 181–202.

[142] P. R. Spalart and S. Allmaras. "A one-equation turbulence model for aerodynamic flows". In: *30th aerospace sciences meeting and exhibit*. 1992, p. 439.

[143] P. R. Spalart and G. N. Coleman. "Numerical study of a separation bubble with heat transfer". In: *European Journal of Mechanics-B/Fluids* 16.2 (1997), pp. 169–189.

[144] P. R. Spalart and J. H. Watmuff. "Experimental and numerical study of a turbulent boundary layer with pressure gradients". In: *Journal of Fluid Mechanics* 249 (1993), pp. 337–371.

[145] S. Srinath, J. C. Vassilicos, C. Cuvier, J.-P. Laval, M. Stanislas, and J.-M. Foucaut. "Attached flow structure and streamwise energy spectra in a turbulent boundary layer". In: *Physical Review E* 97.5 (2018), p. 053103.

[146] P. N. Swarztrauber. "The methods of cyclic reduction, Fourier analysis and the FACR algorithm for the discrete solution of Poisson's equation on a rectangle". In: *Siam Review* 19.3 (1977), pp. 490–501.

[147] Á. Tanarro, R. Vinuesa, and P. Schlatter. "Effect of adverse pressure gradients on turbulent wing boundary layers". In: *Journal of Fluid Mechanics* 883 (2020).

[148] H. Tennekes and J. L. Lumley. *A first course in turbulence*. MIT press, 1972.

[149] T. Theodorsen. “Mechanisms of turbulence”. In: *Proceedings of the 2nd Midwestern Conference on Fluid Mechanics*. 1952.

[150] A. A. Townsend. “Equilibrium layers and wall turbulence”. In: *Journal of Fluid Mechanics* 11.01 (1961), pp. 97–120.

[151] A. A. Townsend. “The properties of equilibrium boundary layers”. In: *Journal of Fluid Mechanics* 1.6 (1956), pp. 561–573.

[152] A. A. Townsend. *The structure of turbulent shear flow*. Cambridge university press, 1976.

[153] M. Tutkun, W. K. George, J. Delville, M. Stanislas, P. B. V. Johansson, J.-M. Foucaut, and S. Coudert. “Two-point correlations in high Reynolds number flat plate turbulent boundary layers”. In: *Journal of Turbulence* 10 (2009), N21.

[154] M. Vallikivi, B. Ganapathisubramani, and A. J. Smits. “Spectral scaling in boundary layers and pipes at very high Reynolds numbers”. In: *Journal of Fluid Mechanics* 771 (2015), pp. 303–326.

[155] M. Vallikivi, M. Hultmark, and A. J. Smits. “Turbulent boundary layer statistics at very high Reynolds number”. In: *Journal of Fluid Mechanics* 779 (2015), pp. 371–389.

[156] J. C. Vassilicos, J.-P. Laval, J.-M. Foucaut, and M. Stanislas. “The streamwise turbulence intensity in the intermediate layer of turbulent pipe flow”. In: *Journal of Fluid Mechanics* 774 (2015), pp. 324–341.

[157] C. S. Vila, R. Vinuesa, S. Discetti, A. Ianiro, P. Schlatter, and R. Örlü. “Experimental realisation of near-equilibrium adverse-pressure-gradient turbulent boundary layers”. In: *Experimental Thermal and Fluid Science* 112 (2020), p. 109975.

[158] C. S. Vila, R. Vinuesa, S. Discetti, A. Ianiro, P. Schlatter, and R. Örlü. “Separating adverse-pressure-gradient and Reynolds-number effects in turbulent boundary layers”. In: *Physical Review Fluids* 5.6 (2020), p. 064609.

[159] R. Vinuesa, A. Bobke, R. Örlü, and P. Schlatter. “On determining characteristic length scales in pressure-gradient turbulent boundary layers”. In: *Physics of fluids* 28.5 (2016), p. 055101.

[160] R. Vinuesa, R. Örlü, C. S. Vila, A. Ianiro, S. Discetti, and P. Schlatter. “Revisiting history effects in adverse-pressure-gradient turbulent boundary layers”. In: *Flow, turbulence and combustion* 99.3-4 (2017), pp. 565–587.

[161] J. M. Wallace, H. Eckelmann, and R. S. Brodkey. “The wall region in turbulent shear flow”. In: *Journal of Fluid Mechanics* 54.1 (1972), pp. 39–48.

[162] H.-P. Wang, S.-Z. Wang, and G.-W. He. “The spanwise spectra in wall-bounded turbulence”. In: *Acta Mechanica Sinica* 34.3 (2018), pp. 452–461.

[163] T. Wei and Y. Maciel. “Derivation of Zagarola-Smits scaling in zero-pressure-gradient turbulent boundary layers”. In: *Physical Review Fluids* 3.1 (2018), p. 012601.

[164] D. C. Wilcox et al. *Turbulence modeling for CFD*. Vol. 2. DCW industries La Canada, CA, 1998.

[165] R. B. Wilhelmson and J. H. Ericksen. “Direct solutions for Poisson’s equation in three dimensions”. In: *Journal of Computational Physics* 25.4 (1977), pp. 319–331.

[166] C. E. Willert. “High-speed particle image velocimetry for the efficient measurement of turbulence statistics”. In: *Experiments in fluids* 56.1 (2015), pp. 1–17.

[167] C. E. Willert, C. Cuvier, J.-M. Foucaut, J. Klinner, M. Stanislas, J.-P. Laval, S. Srinath, J. Soria, O. Amili, C. Atkinson, et al. “Experimental evidence of near-wall reverse flow events in a zero pressure gradient turbulent boundary layer”. In: *Experimental Thermal and Fluid Science* 91 (2018), pp. 320–328.

[168] Y. Wu. “A study of energetic large-scale structures in turbulent boundary layer”. In: *Physics of Fluids* 26.4 (2014), p. 045113.

[169] M. Yoon, J. Hwang, J. Yang, and H. J. Sung. “Wall-attached structures of streamwise velocity fluctuations in an adverse-pressure-gradient turbulent boundary layer”. In: *Journal of Fluid Mechanics* 885 (2020), A12.

[170] R. Yuvaraj. “Analyse de la cascade d’énergie dans une couche limite turbulente”. PhD thesis. Ecole centrale de Lille, 2021.

[171] M. V. Zagarola and A. J. Smits. “Mean-flow scaling of turbulent pipe flow”. In: *Journal of Fluid Mechanics* 373 (1998), pp. 33–79.

[172] M. V. Zagarola and A. J. Smits. “Scaling of the mean velocity profile for turbulent pipe flow”. In: *Physical review letters* 78.2 (1997), p. 239.

[173] J. Zhou, R. J. Adrian, S. Balachandar, and T. M. Kendall. “Mechanism for generating coherent packets of hairpin vortices in channel flow”. In: *Journal of Fluid Mechanics* 387 (1999), pp. 353–396.

Direct Numerical Simulation of Wall Turbulence subjected to an Adverse Pressure Gradient

The main objective of this work is to analyze the effects of a moderate adverse pressure gradient on the dynamics of turbulent boundary layer flows. For that purpose, a direct numerical simulation (DNS) of the turbulent boundary layer (TBL) subjected to a moderate adverse pressure gradient (APG) out of equilibrium has been performed using the open-source code Incompact3d up to a Reynolds number of 8000 based on momentum thickness. A large database resolved in time and space was collected and used to analyze the turbulence statistics. Special attention has been paid to the existence and evolution of the outer peak of Reynolds stresses observed in APG wall-bounded flows. Different velocity scalings have been investigated and tested against the numerical results. The velocity scale based on the shear stress is shown to scale all the Reynolds stresses profiles for different Reynolds numbers, indicating that all Reynolds stresses are associated with a single dynamics of turbulent structures.

The large-scale coherent structures of the streamwise velocity fluctuations have been investigated using two-point spatial correlation. A comparison with a zero pressure gradient case at an equivalent Reynolds number allows us to further investigate the effect of the pressure gradient on the size and inclination of attached coherent structures. A deeper investigation of the coherent structures was also performed, where each structure was detected separately based on a thresholding method to distinguish between the effects of large and small scales and to better understand the mechanisms controlling the dynamics of these structures. The contribution of large-scale motions (LSM) on the Reynolds stresses comparing with ZPG case was also analyzed.

Keywords: turbulence, direct numerical simulation, turbulent boundary layers

---

Simulation numérique directe de la turbulence de paroi soumise à un gradient de pression défavorable

L'objectif principal de ce travail est d'analyser les effets d'un gradient de pression défavorable modéré sur la dynamique d'écoulement d'une couche limite turbulente. Dans ce contexte, une simulation numérique directe (DNS) de la couche limite turbulente (TBL) soumise à un gradient de pression défavorable modéré (APG) hors équilibre a été réalisée jusqu'à un Reynolds de 8000 en utilisant le code open-source Incompact3d. Une large base de données résolues en temps et en espace a été collectée et utilisée pour analyser les statistiques de la turbulence. Une attention particulière a été consacrée à l'existence et à l'évolution du pic de contraintes de Reynolds observé dans la zone externe de la couche limite. Différentes échelles de vitesse ont été étudiées, testées et confrontées aux résultats numériques. L'échelle de vitesse basée sur la contrainte de cisaillement permet de mettre à l'échelle tous les profils de contraintes de Reynolds pour plusieurs nombres de Reynolds, ce qui indique que toutes les contraintes de Reynolds sont associées à une dynamique unique des structures turbulentes.

Les structures cohérentes à grande échelle des fluctuations de vitesse longitudinales ont été étudiées en utilisant la corrélation spatiale en deux points. Une comparaison avec un cas sans gradient de pression à un nombre de Reynolds équivalent nous permet d'étudier l'effet du gradient de pression sur la taille et l'inclinaison des structures cohérentes attachées. Une étude approfondie sur les structures cohérentes a également été réalisée, où chaque structure a été détectée séparément en utilisant une méthode de seuillage afin de distinguer les effets des grandes et petites échelles et de mieux comprendre les mécanismes qui contrôlent la dynamique de ces structures. La contribution des mouvements de grande échelle (LSM) sur les contraintes de Reynolds en comparaison avec le cas ZPG a également été analysée.

Mots clés : turbulence, simulation numérique directe, couches limites turbulentes